IN-PLACE HOT MIX ASPHALT DENSITY ESTIMATION USING GROUND PENETRATING RADAR

By

Imad l. Al-Qadi
Zhen Leng
Al Larkin

Technical Report of Research
Supported by the

FEDERAL AVIATION ADMINISTRATION

Under Cooperative Agreement
DOT 05-C-AT-UIUC

UNIVERSITY OF ILLINOIS AT URBANA-CHAMPAIGN
ADVANCED TRANSPORTATION RESEARCH AND ENGINEERING LABORATORY (ATREL)

ICT Report No. 11-096

December 2011

FINAL REPORT

IN-PLACE HOT MIX ASPHALT DENSITY ESTIMATION USING GROUND PENETRATING RADAR

BY
IMAD L. AL-QADI
ZHEN LENG
AL LARKIN

DEPARTMENT OF CIVIL
AND ENVIRONMENTAL ENGINEERING

UNIVERSITY OF ILLINOIS AT URBANA-CHAMPAIGN
URBANA, ILLINOIS

ICT REPORT NO. 11-096

DECEMBER 2011

ACKNOWLEDGMENT/DISCLAIMER

This report is based on the results of an FAA project, Nondestructive Testing and Evaluation (NDTE) Technologies for Airport Pavement Acceptance and Quality Assurance Activities. The FAA project was conducted in cooperation with the Center of Excellence for Airport Technology (CEAT) and the University of Illinois at Urbana-Champaign.

The contents of this study reflect the views of the authors, who are responsible for the facts and the accuracy of the data presented herein. The contents do not necessarily reflect the official views or policies of the CEAT or FAA. The research was conducted at the Advanced Transportation Research and Engineering Laboratory (ATREL) at the University of Illinois at Urbana-Champaign. This paper does not constitute a standard, specification, or regulation.

EXCUTIVE SUMMARY

In-situ asphalt mixture density is critically important to the performance of flexible airport pavements: density that is too high, or too low, may cause early pavement distresses. Traditionally, two methods have been commonly used for in-situ asphalt mixture density measurement: laboratory testing on field-extracted cores and in-situ nuclear gauge testing. However, both these methods have limitations. The coring method damages pavement, causes traffic interruption, and provides only limited data at discrete locations. The nuclear gauge method also provides limited data measurement. Moreover, it requires a license for the operators because it uses radioactive material. To overcome the limitations of these traditional methods, this study proposes to develop a nondestructive method of using ground penetrating radar (GPR) to measure in-situ asphalt mixture density accurately, continuously, and rapidly.

The prediction of asphalt mixture density using GPR is based on the fact that the dielectric constant of an asphalt mixture, which can be measured by GPR, is dependent on the dielectric and volumetric properties of its components. According to electromagnetic (EM) mixing theory, two candidate specific gravity models, namely the modified complex refractive index model (CRIM) and the modified Bottcher model, were developed to predict the bulk specific gravity of asphalt mixture from its dielectric constant.

To evaluate the performance of these two models, a full-scale six-lane test site with four sections in each lane was carefully designed and constructed. Forty cores were extracted from the test site, and their densities were measured in the laboratory and compared to the GPR-predicted values using the two models. Both models were found effective in predicting asphalt mixture density, although the modified Bottcher model performed better. To account for the effect of the non-spherical inclusions in asphalt mixture and further improve the density prediction accuracy, a shape factor was introduced into the modified Bottcher model. Nonlinear least square curve fitting of the field core data indicated that a shape factor of -0.3 provided the best-performance model, which is referred to as the Al-Qadi Lahouar Leng (ALL) model.

The performance of the ALL model was validated using data collected from an active pavement construction site in Chicago area. It was found that when the ALL model was employed, the prediction accuracy of the GPR was comparable to, or better than, that of the traditional nuclear gauge. For the asphalt mixtures without slags, the average density prediction errors of GPR were between 0.5% and 1.1% with two calibration cores, while those of the nuclear gauge were between 1.2% and 3.1%.

Due to the importance of accurate input of the dielectric constant of asphalt mixture to the prediction accuracy of the specific gravity model, this study also looked into alternative methods for asphalt mixture dielectric constant estimation. The extended common mid-point (XCMP) method using two air-coupled antenna systems was developed, and its implementation feasibility was explored. The XCMP method was found to provide better performance than the traditional surface-reflection method for thick pavement structures with multi-lifts. However, for thin pavement layers (less than 63 mm thick), the accuracy of this method could be improved. Factors accounting for the accuracy reduction for a thin surface layer include the sampling rate limitation of the GPR systems, as well as the possible overlap of the GPR signal reflections at the surface and bottom of the thin asphalt layer.

TABLE OF CONTENTS

LIST OF FIGURES

LIST OF TABLES

CHAPTER 1 INTRODUCTION

1.1 Introduction

The quantification of in-situ airport pavement system characteristics is needed for both quality assurance (QA) of new pavements and condition assessment of existing pavements. For flexible airport pavements, the properties of the asphalt concrete (AC) layer can be grouped into three categories: volumetric, structural, and functional. The volumetric properties of an AC layer mainly include density, air void content, asphalt content, aggregate gradation, and voids in mineral aggregate; the structural properties of an AC layer mainly include the thickness and modulus of the layer and its bond with the underlying lift or layer; and the functional properties of an AC layer mainly include the transverse and longitudinal surface profiles, friction and noise (Von Quintus 2009).

Among the various criteria used to assess flexible airport pavement potential performance, the in-situ asphalt mixture density is critically important: density that is either too high, or too low, can lead to premature pavement failures, which in turn result in considerable extra cost in maintenance and rehabilitation. In pavement engineering, the terms *density* and *air void content* are often used interchangeably. Air void content (V_a) is defined as the percentage of air voids within asphalt mixture by volume. It is typically quantified by comparing a test specimen's bulk density with its theoretical maximum density (TMD), the density when the air void content is equal to zero. In the laboratory, the air void content is typically calculated using AASHTO T269 (2007), ASTM D3203 (2003), or an equivalent procedure. These procedures all use lab-measured bulk specific gravity (G_{mb}) and theoretical maximum specific gravity (G_{mm}) in the following equation:

$$V_a = 100\left(\frac{G_{mm} - G_{mb}}{G_{mm}}\right). \tag{1.1}$$

Here, the specific gravity of asphalt mixture is equal to the density of asphalt mixture divided by the density of water at 4 ^{o}C, which has a known value of 1 g/cm^3. Therefore, G_{mb} and G_{mm} are numerically the same as the bulk density and TMD, respectively, of asphalt mixture in g/cm^3. In the practice of construction, percent of TMD, which is equal to 100-V_a, is also commonly used to describe the compaction level of asphalt pavement.

To achieve optimum long-term pavement performance, the density of dense-graded mixtures should be controlled within a range of air void content from 3% to 8% during their service life (Roberts et al. 1996). Over-compacted asphalt mixture (V_a below 3%) can cause rutting, shoving and bleeding, while AC surfaces whose densities are too low (V_a above 8%) allow water and air to penetrate into a pavement, increasing the danger for water damage, oxidation, raveling, and cracking (Killingsworth 2004). As a result, in-situ asphalt mixture density or air void content is commonly measured in practice not only as a QA index for new pavements but as a condition index for evaluating the structural capacity of existing pavements to estimate their remaining service life as well. Note that the discussion here applies to dense-graded asphalt mixture and not open-graded asphalt mixture or stone mastic asphalt (SMA).

1.2 Problem Statement

Traditionally, two techniques are commonly used to estimate in-situ asphalt mixture density: laboratory tests on pavement cores and in-situ nuclear gauge measurements (Figure 1.1 (a) and (b)). The first technique adopts a destructive procedure, in which cores are extracted from pavement to directly measure the thicknesses and the volumetric properties of different pavement layers. Although this procedure provides the most accurate density measurements, it is time consuming and provides only limited information, as cores are typically taken every 300 m (1000 ft). And while the nuclear gauge is a nondestructive technique that provides reasonably accurate estimates of the AC layer density, this technique, too, has some drawbacks. First, the nuclear gauge, like the lab tests on cores, also provides limited information about the layer density since nuclear measurements are usually taken with high spatial spacing. Second, nuclear gauge operation requires special licensing since it uses radioactive material, and thus can be applied only by authorized personnel.

(a) Coring (b) Nuclear gauge (c) Nonnuclear EM gauge

Figure 1.1 Available methods for in-situ asphalt mixture density measurement.

Recently, electromagnetic (EM) density gauges have entered the market as an alternative to the coring process and the nuclear density gauges (Figure 1.1 (c)). These nonnuclear devices, which use EM waves to measure in-place density, have the advantage of completely bypassing the licenses, training, specialized storage, and safety risks associated with devices that use a radioactive source (Romero 2002). However, just like the traditional methods, the nonnuclear density gauges are unable to provide high-coverage measurements either. Moreover, the reliability and accuracy of this method are currently still in debate.

Considering the limitations of the current methods for in-situ asphalt mixture density measurement, a new method with improved coverage area and efficiency is keenly desired. Ideally, this new method should be able to provide density measurements nondestructively, continuously, and rapidly.

1.3 Research Objective

Among various nondestructive evaluation (NDE) techniques for airport pavement quality assessment, ground penetrating radar (GPR), an EM-wave-based method, is distinguished by its high coverage area and rapid survey speed. Additionally, the dielectric properties of a mixture, which can be measured by GPR, are physically related to its volumetric properties, according to the EM mixing theory. Therefore, if validated models that connect an asphalt mixture's measured dielectric properties and its density are

developed, the continuous and rapid measurement of in-place asphalt mixture density using GPR will become feasible. Consequently, this research effort proposes to develop the theoretical models and implementation algorithm for using GPR as an NDE tool for in-situ asphalt mixture density measurement.

1.4 Report Scope

This report is divided into five chapters. Chapter 1 provides an introduction about the research, describes the existing problems, and presents the research objective. Chapter 2 outlines the current state of knowledge, which includes available NDE tools for evaluating flexible airport pavement properties, GPR systems and their pertinent EM theories, and GPR applications to pavements. Chapter 3 details the approach that this study has implemented to achieve the research objective, which includes the development of specific gravity models, model evaluation and fine-tuning using test site data, model validation using in-service pavement data, dielectric constant estimation using extended common midpoint method (XCMP) method, and implementation plan for predicting in-situ asphalt mixture density using GPR. Chapter 4 summarizes the findings and conclusions of this study. Finally, Chapter 5 presents the recommendations for further study.

CHAPTER 2 CURRENT STATE OF KNOWLEDGE

Ground penetrating radar (GPR) is one of the NDE tools that have been successfully applied in airport pavement engineering. Each of these NDE tools serves a particular testing purpose and has both advantages and limitations. The foundations of GPR applications lie in the electromagnetic (EM) theory. By testing the response of a pavement material under excited EM fields, GPR systems can be used to quantify those pavement characteristics that are related to its EM properties.

This chapter begins with a review of various NDE methods commonly used for the quality evaluation of airport pavements, especially the evaluation of flexible pavements, explaining why GPR is the most potential NDE tool for predicting asphalt pavement density. The chapter then introduces the EM principles, which GPR is based on. The chapter concludes with a description of the current status of the GPR applications to pavements, including the in-situ asphalt mixture density measurement.

2.1 NDE Methods for Airport Pavement Quality Assessment

The choice of method to assess airport pavement quality is a function of testing purpose. In general, these methods can be grouped into two categories: destructive and non-destructive. The destructive methods usually involve extracting cores or cutting samples from the pavement and then testing these cores or samples in the laboratory. Although destructive methods can provide accurate results, their drawbacks are obvious and many; some include the damage inflicted on the pavement structure, the inability to provide real-time measurement, and, often, the disruption suffered by pavement users. Given this, nondestructive methods are preferred for the condition assessment of in-situ pavements. The value of applying nondestructive techniques here proceeds from the noninvasive nature of the techniques, the anticipated rapidity of the measurements, nondisturbance to the service during data collection, and the quantitative assessment of the condition.

In this section, the most commonly used NDE techniques for the quality assessment of pavements, especially flexible pavements, are reviewed. These techniques are divided according to their working principles into four categories: deflection-based methods, seismic methods, electromagnetic methods, and other methods.

2.1.1 Deflection-Based Methods

Deflection-based methods for pavement evaluation mainly refers to those methods that determine the pavement layer stiffness based on the measured deflections at pavement surface under controlled static, vibratory, or impulse loading.

2.1.1.1 Static load deflection equipment

Static load deflection equipment, such as the well-known Benkelman Beam, is among the earliest applications of NDE methods in pavement evaluation. As Figure 2.1 shows, the Benkelman Beam measures the maximum deflection response of a pavement to static or slowly applied loads, typically 80 kN (18 kip) on a single axle with dual tires inflated to 480 to 550 kPa (70 to 80 psi). This method is easy to use, with a low equipment cost, but it is also slow and labor-intensive and does not provide a deflection basin. Furthermore, the static or quasi-static loading employed does not accurately represent the effects of a moving wheel load.

Figure 2.1 Benkelman Beam for pavement deflection measurement.

2.1.1.2 Steady-state dynamic load deflection equipment

Steady-state dynamic load deflection devices apply a static preload and a sinusoidal vibration to the pavement with a dynamic force generator, as Figure 2.2 illustrates. The main advantage that steady-state deflection equipment offers over static deflection equipment is that it can measure deflections at different locations using

geophones to construct a deflection basin. However, one technical problem of this method is that the static preload in most cases is relatively large in comparison with the maximum peak-to-peak loading, and the stress states and stiffness of some stress-sensitive paving materials may be affected by the static preload. In addition, the frequency of loading affects the deflection results, and it is difficult to establish a load frequency that matches that of moving vehicles.

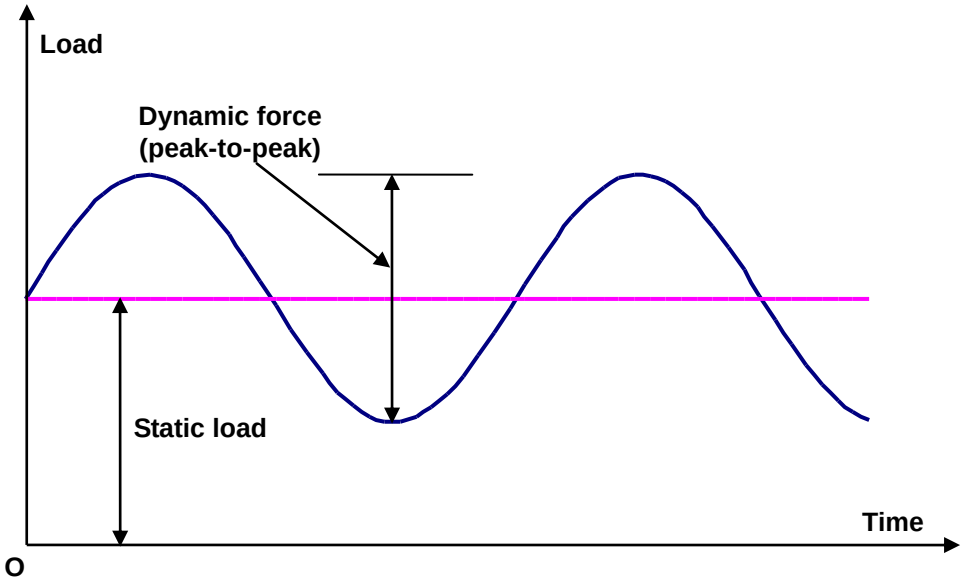

Figure 2.2 Typical output of vibrating steady-state force generator.

2.1.1.3 Impulse load deflection equipment

The most common type of deflection-based device for pavement evaluation is the falling weight deflectometer (FWD). The FWD can be mounted either in a vehicle or on a trailer and is equipped with a weight and several velocity transducer sensors. As Figure 2.3 shows, the FWD is a device capable of applying impulse loads to the pavement surface, similar in magnitude and duration to that of a single heavy moving wheel load. The response of the pavement system is measured in terms of vertical deformation, or deflection, over a given area using geophones or seismometers. An FWD enables its users to determine a deflection basin caused by a controlled load. FWD-generated data, combined with information about layer thickness, can be used to obtain the in-situ resilient elastic moduli of pavement structure layers. This finding can then be used in a structural

analysis to determine the bearing capacity, estimate expected life, and calculate overlay requirements over a desired design life. The advantages of an impulse-load response-measuring device over steady-state deflection equipment are its rapidity, its variability of impact load, and its more accurate simulation of the transient loading of traffic.

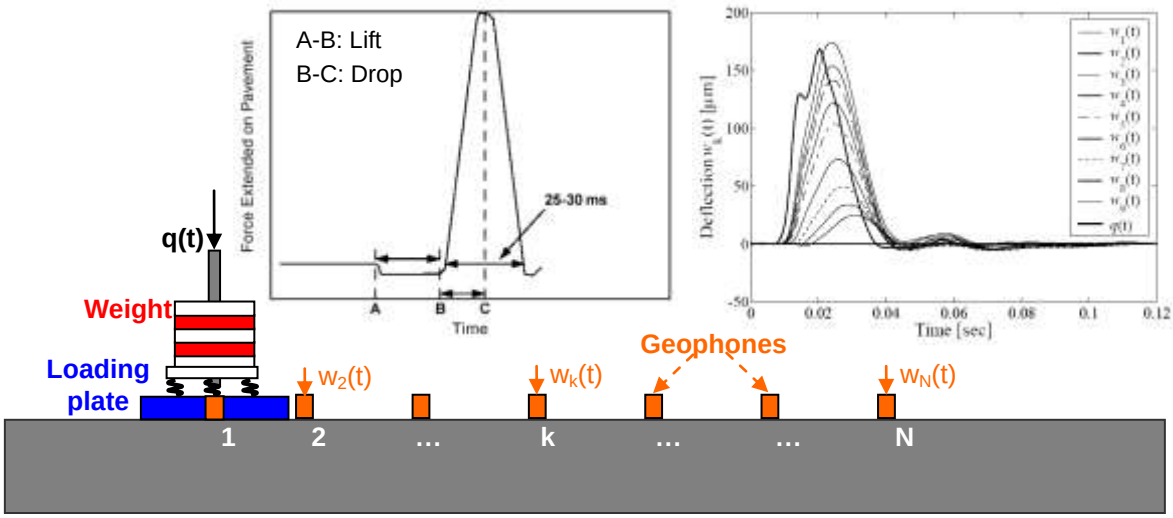

Figure 2.3 FWD test setup and time histories of loading and deflections (Guzina and Osburn 2002).

For airport pavement evaluation, the heavy weight deflectometer (HWD) is used to simulate heavy loading from aircrafts such as the Boeing 747. The HWD follows the same testing and data analysis procedure as the FWD but is capable of applying a higher impact-loading capacity. The loading range of the HWD is 30 to 240 kN (6.7 to 54.0 kip) compared with the FWD's range of 7 to 150 kN (1.6 to 33.7 kip). The light weight deflectometer (LWD), shown in Figure 2.4, is a portable and lightweight version of the FWD and is mainly used for testing unbounded pavement materials. Relative to the FWD, the LWD has a shallow depth of influence due to the lighter weight (less than 20 kg or 44 lbs) being dropped by hand. It is, therefore, ideal for single-layer structural evaluation.

Figure 2.4 Light weight deflectometer.

2.1.1.4 Continuous load deflection equipment

One of the common limitations of the aforementioned deflection devices is that they can collect data only at discrete locations. To expedite the data collection and increase the data coverage, research efforts have been made to develop deflectometers able to perform continuous data collection. For example, the rolling wheel deflectometer (RWD) is a device that measures the pavement deflection beneath an actual moving semi-trailer wheel load. Applied Research Associates, Inc. designed and built the RWD trailer, which loads the pavement with a 177-N (18-kip) single axle. A continuous deflection profile is measured by a series of lasers mounted beneath the RWD trailer (Figure 2.5). Highway agencies are able to measure pavement deflections at normal highway speeds, without the need, expense, or safety risk entailed by lane closures. The RWD can be used in conjunction with existing deflection technology such as the falling weight deflectometer (FWD). The RWD is a good tool for identifying problem pavement sections that a highway agency could then revisit with the FWD for more detailed analysis (Van 2008). Another example of the continuous deflection measuring device is the rolling dynamic deflectometer (RDD) developed in Texas (James and Stokoe, 1998). The RDD applies large sinusoidal dynamic forces to the pavement through specially designed loading rollers. The resulting deflections are simultaneously measured by rolling sensors designed to minimize the influence of noise caused by rough pavement surfaces. Distance measuring and data acquisition systems were designed to record the forces applied to the pavement

and the resulting dynamic displacements; these systems also track the position of the RDD. However, the RDD survey can only be performed at a speed of up to 2.4 km/h (1.5 mph).

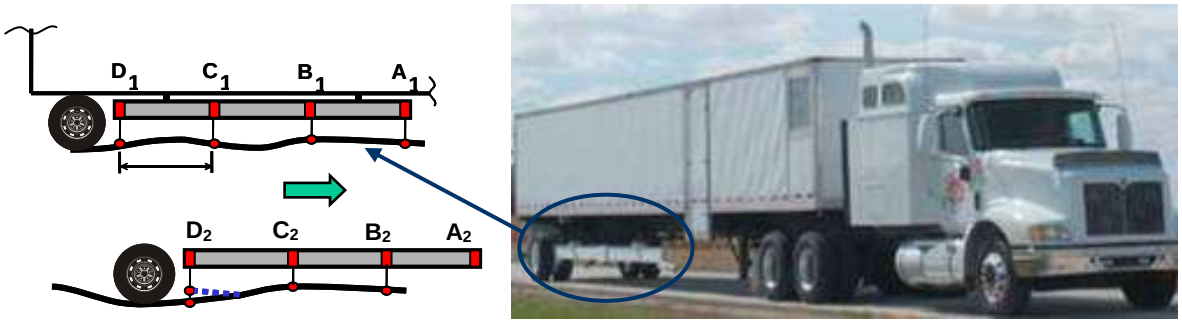

Figure 2.5 Rolling wheel deflectometer.

2.1.2 Stress Wave Methods

Stress wave methods are another type of NDE methods commonly used to evaluate pavement structural condition. A stress wave refers to the mechanical wave that propagates in elastic or viscoelastic materials due to a stress-based disturbance. The properties of a pavement, such as the layer thickness, stiffness, interface bonding, and internal distresses, can potentially be characterized by the pavement's response to a stress disturbance, which is generated by different devices such as a drop weight, a strike hammer, and a transducer.

There are two main types of stress waves: body waves and surface waves. Body waves can be further divided into longitudinal or primary waves (P wave), transverse or secondary waves (S wave), and Lamb waves according to the direction of the particle motion. In a P wave, particle motion is parallel to the propagation direction; in an S wave, particle motion is perpendicular to the propagation direction; and a Lamb wave is a complex wave whose particle motion lies in the plane defined by the plane normal and the direction of wave propagation (Achenbach1984). Rayleigh waves, whose particle motions follow elliptical orbits, are a type of surface waves.

In this section, three types of stress wave methods, which are commonly used for pavement structure evaluation, are introduced. These methods include the impact echo (IE)/pulse echo method, the ultrasonic pulse velocity (UPV) method, and the spectral

analysis of surface wave (SASW) method.

2.1.2.1 Impact echo/pulse echo method

As illustrated in Figure 2.6, in the IE/ pulse echo test, an impact or an ultrasonic pulse is made at the pavement surface to generate stress waves; the reflections of these waves from any inhomogeneities in the pavement structure, such as layer interfaces, voids, and cracks, are recorded to extract information at the tested location. From the time-domain data of the reflected body waves, the frequency spectrum is obtained. The frequency peaks identified in the frequency domain can be used to calculate the distance to a receiver. For a single layer structure, the thickness of the layer *d* can be calculated as follows (Hill et al. 2000):

$$d = \beta \frac{v_p}{f}, \tag{2.1}$$

where v_p is the P-wave velocity, f is the resonant frequency and β is a correction factor. The theoretical basis of the factor β is explained in a study by Gibson and Popovics (2005).

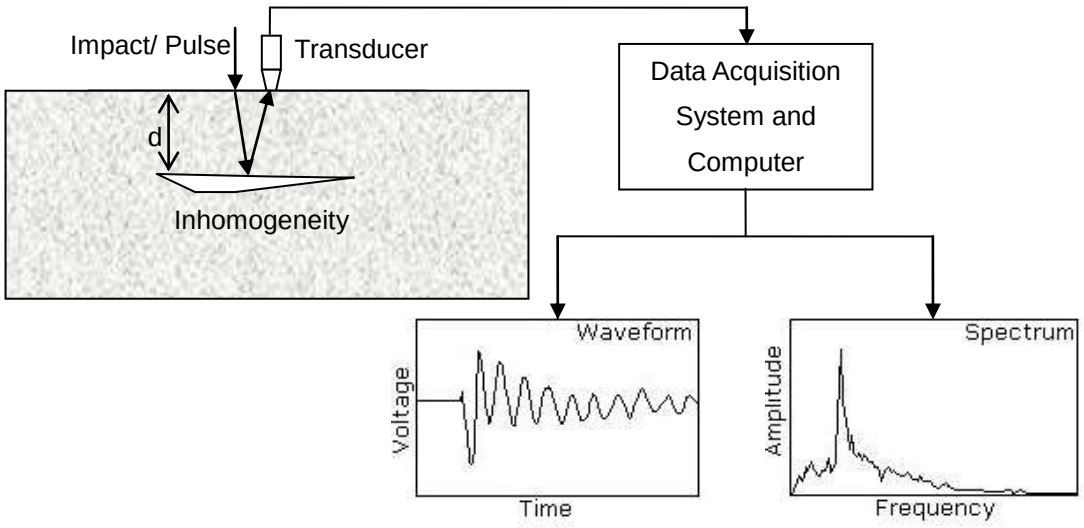

Figure 2.6 Conceptual description of IE test.

2.1.2.2 Ultrasonic pulse velocity method

For more than 60 years, the ultrasonic pulse velocity (UPV) method has been successfully used to evaluate the quality of concrete (Malhotra and Carino 2004). Recent studies also suggest that the UPV method can estimate the dynamic modulus of asphalt mixture with reasonable accuracy (Pellinen and Witczak 2002; Jiang et al. 2006). As depicted in Figure 2.7(a), the UPV test setup consists of a transmitter and receiver at a known distance apart, L. The transient time of the pulse, Δt, is recorded by a timer and the P wave velocity, v_p, is calculated as

$$v_p = \frac{L}{\Delta t}. \tag{2.2}$$

If the density of the material medium, ρ, and the Poisson's ratio, μ, are known the modulus of elasticity, E, can be estimated using the following equation:

$$v_p = \sqrt{\frac{E(1-\mu)}{\rho(1+\mu)(1-2\mu)}}. \tag{2.3}$$

Nevertheless, the estimation of the modulus of elasticity in concrete and asphalt mixture is not normally recommended for two reasons: (1) the errors of the estimation of Poisson's ratio are not negligible; (2) Equation 2.3 is appropriate for homogeneous material only, leaving its validity for inhomogeneous material, such as concrete and asphalt mixture, questionable (Malhotra and Carino 2004). Other applications of the UPV test include characterizing the homogeneity of concrete, estimating the strength of concrete, and monitoring the top-down cracking (Khazanovich et al. 2005), fatigue damage, and crack healing in asphalt pavements (Abo-Qudais and Suleiman 2005; Al-Qadi and Riad 1996). It should be noted that for field testing of in-service pavements, indirect configuration of sensors as shown in Figure 2.7(b) needs to be used, as only the top surface is accessible. The drawbacks of this configuration are that the received signals are weaker relative to the direct transmission method and the collected data are more prone to error, possibly requiring a special procedure to determine the pulse velocity (Luo and Bungey 1996).

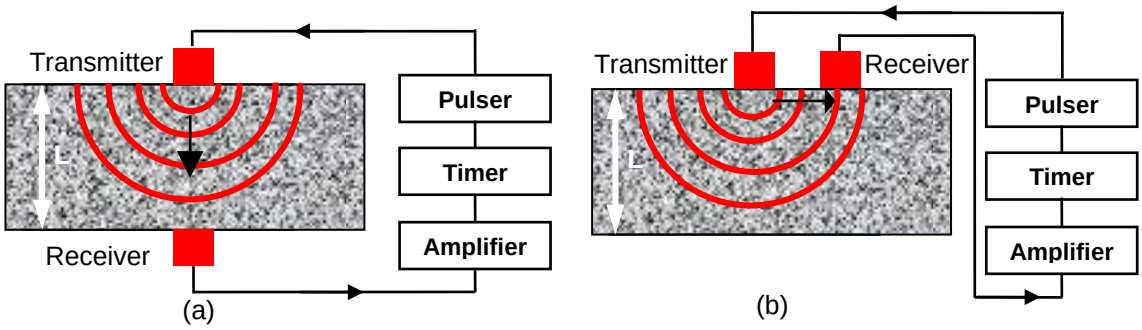

Figure 2.7 UPV test: (a) direct sensor configuration; (b) indirect sensor configuration.

2.1.2.3 Spectral analysis of surface waves method

The SASW method is based on the phenomenon of dispersion of surface waves in layered systems (Tayabji and Lukanen 2000), and, from this phenomenon, defines the elastic moduli profile of a pavement utilizing the inversion process. Presented alongside the basic equations used in the evaluation of the phase velocity in Figure 2.8, the typical SASW test setup demands a seismic source and at least two receivers. The surface of the medium is impacted and the transmitted waves are monitored with the receivers. As the surface waves carry about two-thirds of the seismic energy, they are easier than the P waves and S waves to measure. The wave data analysis can be performed in either the time domain or frequency domain. However, the accuracy of the time-domain analysis is based on the following two assumptions: that the layer does not have surface imperfection and that the impact is "sharp" enough to generate only waves that contain energy for wavelengths shorter than the thickness of the top layer, a condition that is usually difficult to satisfy (Nazarian et al. 1999). Therefore, the frequency-domain analysis, i.e. the SASW, is by far more robust than the time-domain analysis.

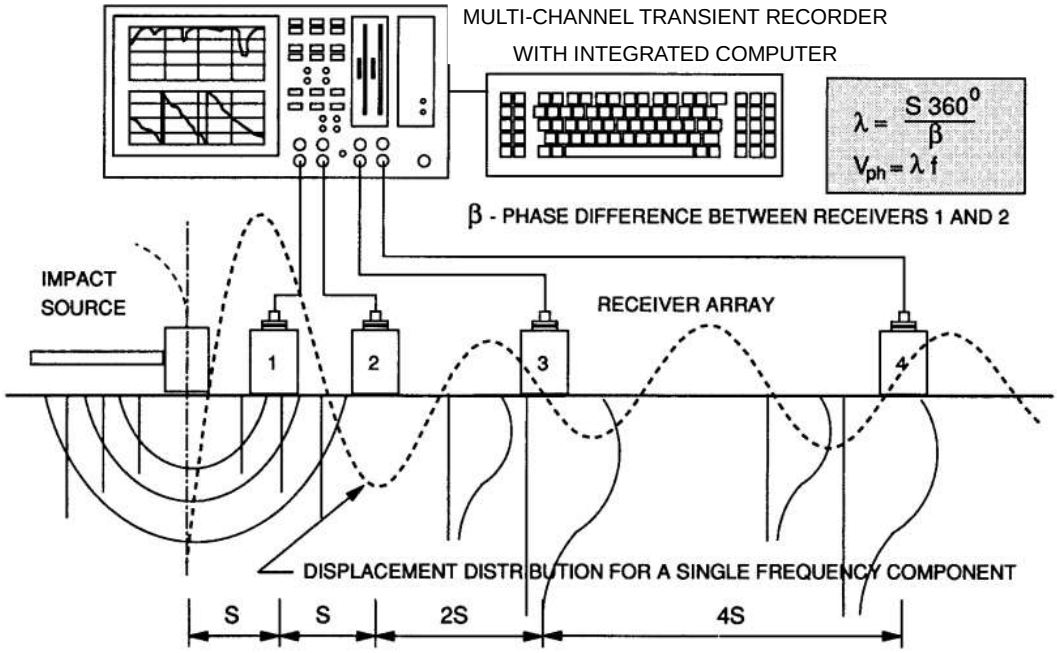

.

Figure 2.8 Schematic of experimental arrangement for SASW test (Gucunski and Krstic 1996).

In the SASW method, the Fourier Transform is performed on the time-domain data collected by the two receivers to obtain a phase spectrum (i.e., variation in phase with frequency). For each frequency, the travel time between receivers can be calculated by

$$t(f) = \frac{\varphi(f)}{360f}, \tag{2.4}$$

where *f* is the frequency, *t(f)* is the travel time of the given frequency, and *Φ(f)* is the phase difference between the two receivers in degrees of the given frequency, which is determined through the Fourier transform.

As the distance between the receivers is identified, the Rayleigh wave velocity at a given frequency is calculated by

$$v_R = \frac{x}{t(f)}, \tag{2.5}$$

and the corresponding wavelength of the Rayleigh wave can be calculated by

$$\lambda_R = \frac{v_r(f)}{f}. \tag{2.6}$$

By repeating the procedure outlined by Equations (2.4) through (2.6) for each frequency, the dispersion curve, a plot of the Rayleigh wave velocity versus wavelength, can be computed.

The Rayleigh wave velocity and S-wave velocity, v_S, are related by Poisson's ratio, μ, by the following approximation (Nazarian et al. 1999):

$$v_s = v_R(1.13 - 0.16\mu). \tag{2.7}$$

Shear modulus, G, can be determined from shear wave velocity by using

$$G = \frac{\gamma}{g} v_s^2, \tag{2.8}$$

where γ and g are the unit weight and acceleration of gravity, respectively.

Finally, Young's modulus, E, can be determined from shear modulus through Poisson's ratio, by using

$$E = 2(1+\mu)G. \tag{2.9}$$

As Figure 2.9 shows, two devices based on the SASW method that are commonly used to determine the pavement layer modulus have been developed: seismic pavement analyzer (SPA) and portable seismic pavement analyzer (PSPA).

(a)

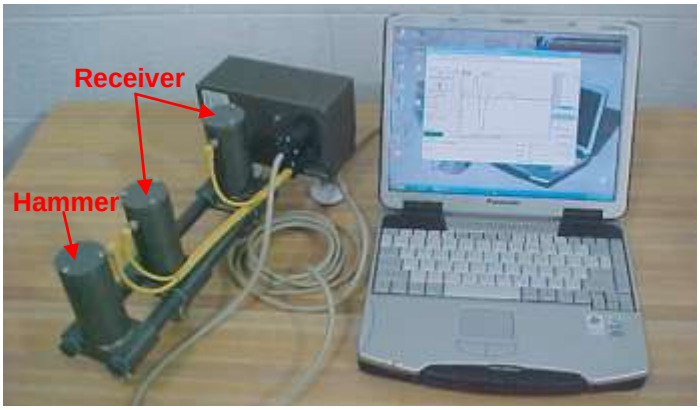

(b)

Figure 2.9 SASW-based equipment: (a) SPA; (b) PSPA (Celaya and Nazarian 2008).

2.1.3 Electromagnetic Methods

Electromagnetic methods are those that rely on technologies such as electrical impedance, electromagnetic wave, magnetic resonance, and infrared thermograph to determine pavement quality. The GPR method belongs to this category.

2.1.3.1 Nuclear and non-nuclear density gauges

Both the nuclear and nonnuclear density gauges (Figure 1.1) introduced in Chapter 1 are essentially electromagnetic devices. The application of the nuclear gauge is based on the transmission and reception of gamma rays, which is a type of EM wave with extremely high frequency (Figure 2.10). Nuclear gauges usually contain a small gamma source such as the Cesium-138 on the end of the retractable rod (as shown in Figure 2.11). Gamma rays emitted from the source interact with electrons in the pavement and those

rays reach the detector are counted. Pavement density is then correlated to the number of gamma rays received by the detector. The nuclear gauges are typically operated in two modes: direct transmission and backscatter. In direct transmission mode, the retractable rod is lowered into the tested pavement through a predrilled hole. In backscatter mode, the retractable rod is lowered so that it is even with the detector but still contained within the instrument. Different calibration factors are used to relate gamma count to actual pavement density in the two testing modes (http://training.ce.washington.edu/WSDOT/, Nov 22, 2010).

The nonnuclear density gauge, or the electrical density gauge, is a recent device created to measure the density of compacted soils or asphalt mixture. This device determines the density of an AC mat by measuring its electrical impedance, defined as the resistance to flow of an alternating current, at a chosen frequency of alternating current. After the impedance is measured, the AC mat's dielectric constant, defined as the ability of a material to store electrostatic energy per unit of volume, can then be determined. The overall dielectric constant of a material (such as asphalt mixture) is a function of the volume and dielectric constant of each component. Therefore, the relative density of a material that is composed of several components can be determined. However, the nonnuclear gauge requires a special procedure for calibrating the particular type of asphalt mixture to be tested. The accuracy and reliability of this method currently remain under debate.

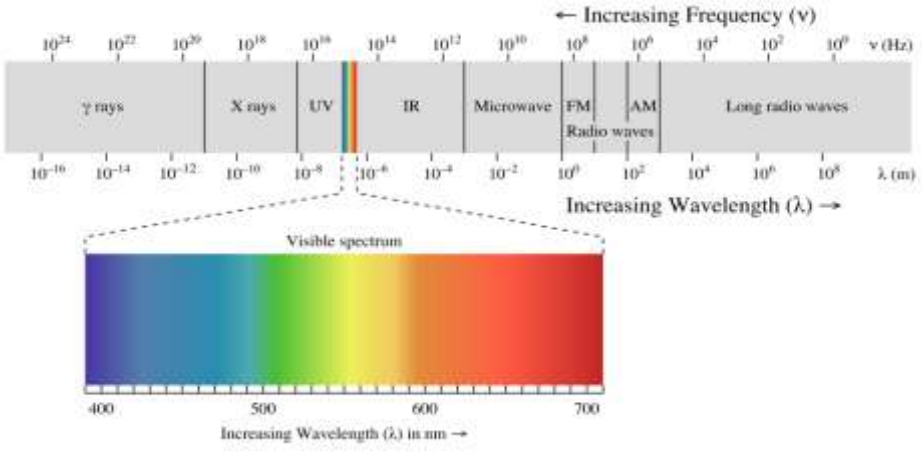

Figure 2.10 Electromagnetic spectrum (http://en.wikipedia.org/wiki/File:EM_spectrum.svg, Oct. 30, 2010).

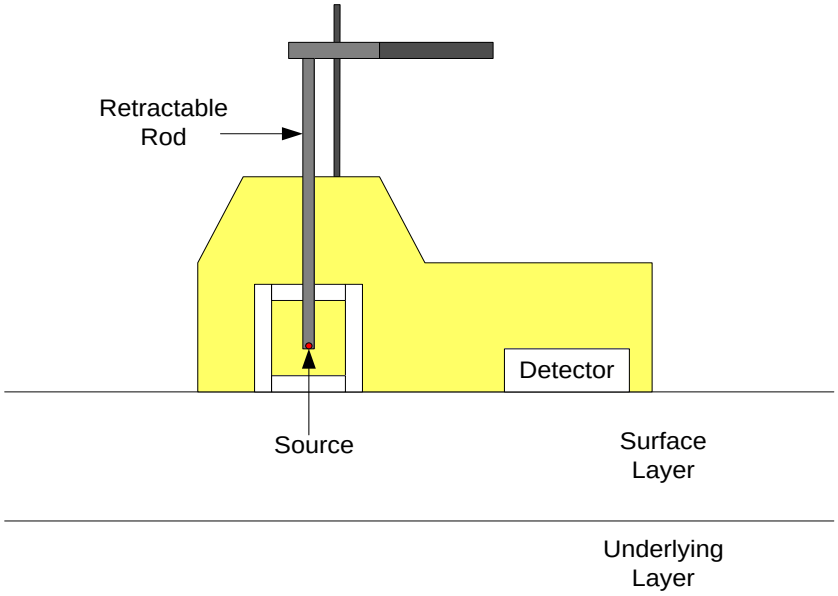

Figure 2.11 Nuclear density gauge schematic.

2.1.3.2 Ground penetrating radar

The majority of the GPR systems used for airport pavement applications are impulse systems, which emit short EM pulses to penetrate the pavement from a moving antenna and record the reflected echoes created at pavement surface and internal inhomogeneities. The two-way travel time to the target and the amplitudes of the reflected pulses can then be measured in the time domain. The great advantages offered by GPR technology include the high speed of data collection and the availability of a continuous profile of the dielectric constants.

A GPR system is typically composed of an antenna, a data acquisition system, a distance measuring instrument (DMI), a survey vehicle or cart, and an optional GPS (Figure 2.12). The core component of a GPR system is the antenna, which is used as either the signal transmitter or receiver or as both. When the same antenna is used as both the transmitter and receiver, the GPR system is called a monostatic system; when one antenna is used for transmission and the other is used for reception, the system is bistatic; and when a single antenna or multiple antennas are used as transmitters and

multiple antennas are used as receivers, the system is multistatic.

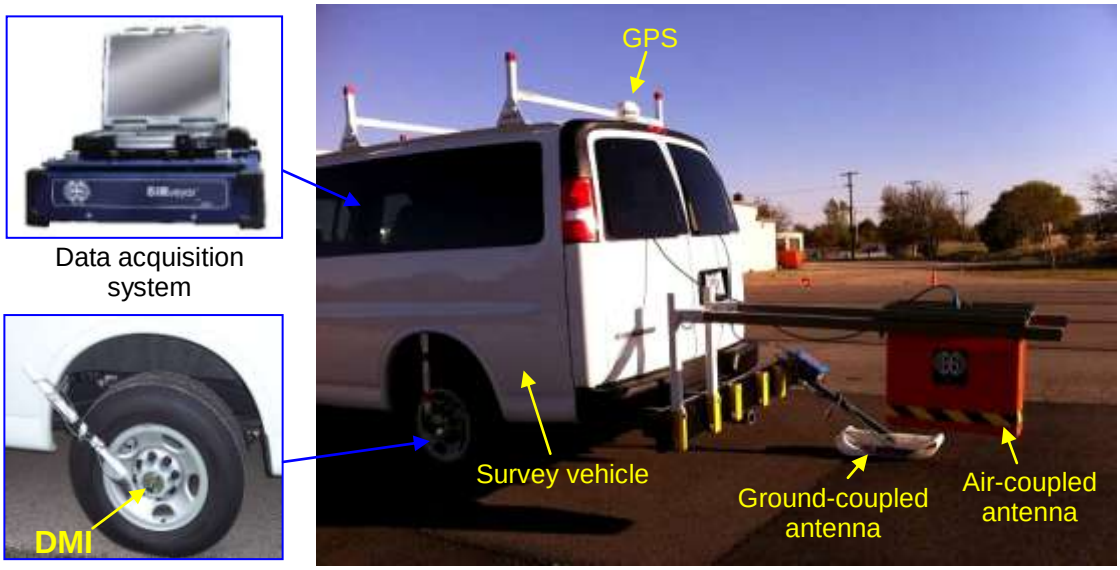

Figure 2.12 Typical components of a van-mounted GPR system.

GPR systems are classified as either air-coupled systems or ground-coupled systems, depending on how the antennas are mounted. As Figure 2.12 displays, air-coupled “horn” antenna systems are typically mounted 150 to 500 mm (6 to 20 in) above the pavement surface. For production use in pavement applications, it is preferable to utilize the air-coupled antennae mounted on a holding bracket attached to the front or rear bumper of a survey vehicle where GPR data can be collected at highway speeds. The elevated antenna also reduces antenna-ground and antenna-target interactions, thereby achieving less antenna clutter and a clear surface reflection (Figure 2.13 (a)). Note that the incident pulse of the GPR antenna is usually in a Mexican-hat shape. However, this setup also poses a pair of problems. First, radar penetration is reduced, as a large percentage of the incident energy is reflected at the pavement surface instead of penetrating into the pavement. Second, undesirable antenna movement can be caused by the surface roughness during data collection at high speed.

On the other hand, a ground-coupled antenna is in full contact with a pavement surface (Figure 2.12); because less energy is reflected by the pavement surface, EM

waves emitted by a ground-coupled system can penetrate deeper than those emitted by an air-coupled system with the same antenna frequency. However, the GPR survey has to be performed at a much lower speed, usually less than 8 km/h (5 mph). Another disadvantage of the ground-coupled systems is the incidence of surface coupling, which is caused by the overlap of the emitted and reflected signals at the surface (Figure 2.13(b)). The surface coupling makes it difficult to determine, without signal processing, the exact time at which the GPR signal hits the pavement surface. Therefore, ground-coupled systems are not recommended for accurate pavement thickness measurements (Leng et al. 2009).

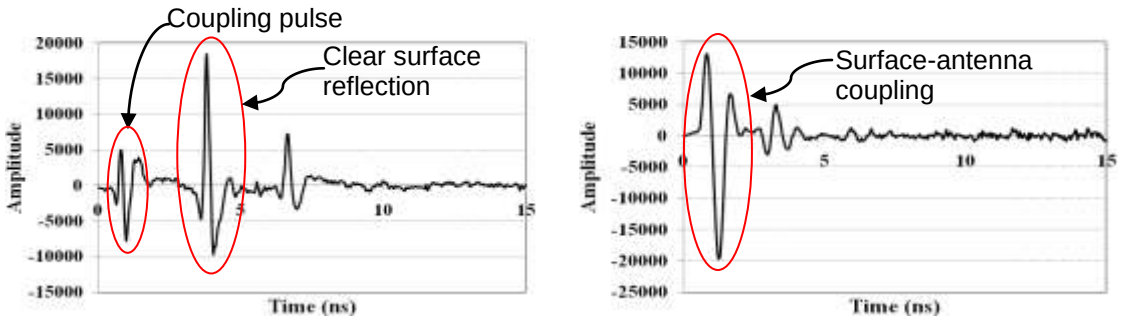

(a) Air-coupled antenna (b) Ground-coupled antenna

Figure 2.13 Typical single-scan GPR signals.

More details about the GPR principles and applications to pavement will be provided in Sections 2.2 and 2.3, respectively.

2.1.3.3 Infrared tomography

Infrared tomography consists of mapping thermal contour on the surface of a material. This technology is based on the recognition that defects and inhomogeneties (e.g., low- or high-density areas in an AC mat) would manifest themselves as local hot or cold regions in the thermal color-map. Therefore, for an anomaly to be detected by thermography, the anomaly must create an atypical temperature or a temperature differential at the surface of the test object. Figure 2.14 shows the thermography images of a good road section and a deteriorated road section. In these images, the brighter color indicates the warmer object and the darker color indicates the colder object.

(a)

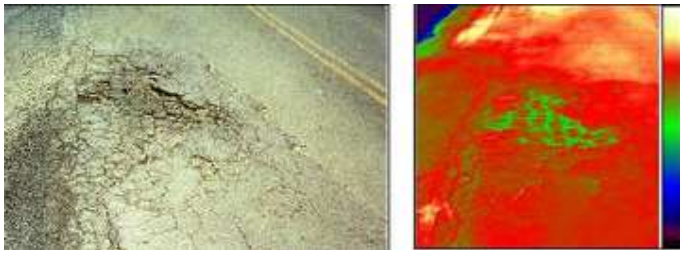

(b)

Figure 2.14 Optical (left) and infrared (right) images of a (a) good road section; (b) deteriorated road section (Loulizi 2001).

2.1.3.4 Laser profiler

Profilers are used to evaluate airport pavement roughness, a measure of riding comfort, and rutting of asphalt pavements. Two types of profilers have commonly been used: contact and noncontact. With their relatively higher survey speed, noncontact profilers, which typically rely on laser sensors, have a distinct advantage over contact profilers. For longitudinal profile measurement, high-speed laser devices are usually mounted over each wheel path to sample at 50-mm intervals. Figure 2.15 shows an example of the laser device mounted in the back of a van. For rutting measurement, it is recommended that a minimum of 11 lasers be used to cover a 3-m (9-ft) transverse profile (Austroads Test Method AG: AM/T009 2007). The preferred configuration is shown in Figure 2.16.

Figure 2.15 Laser device mounted in the back of a van.

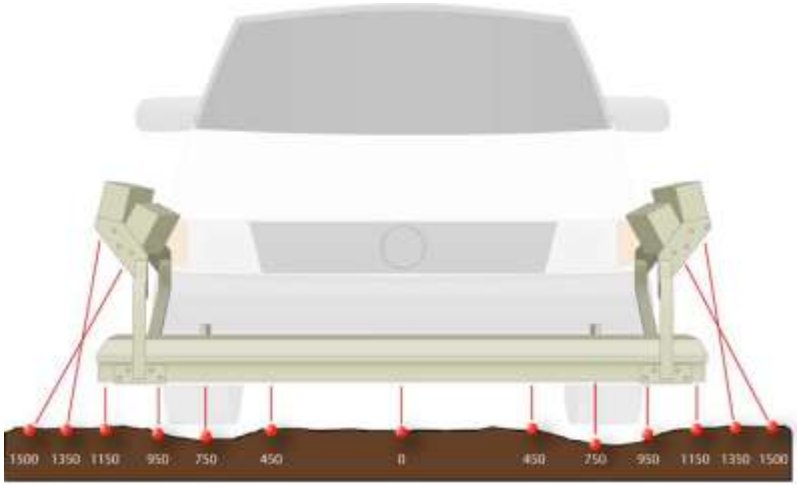

Figure 2.16 Preferred laser configuration for rutting measurement (distance in mm) (Austroads Test Method AG: AM/T009 2007).

2.1.3.5 Magnetic imaging technology

Magnetic imaging technology is used mainly to detect the location of metal within the pavement structure. As Figure 2.17(a) shows, the coil mounted in the device generates a pulse of magnetic field, which induces an eddy current in a pre-placed metal reflector on the surface of the base. EM sensors in the device then measure the intensity of the magnetic field caused by the eddy current in the reflector. Since most concrete materials

have no effect on magnetic fields, the eddy current approach eliminates thickness measurement biases caused by variations in the properties of concrete materials. This technique is medium-independent and can be used to measure concrete thickness of up to 508 mm (20 in).

Two main applications of this technique have been found in pavement: to measure pavement thickness by locating the steel plate pre-buried in the pavement and to measure the dowel bar locations (Figures 2.17(b) and 2.17(c)).

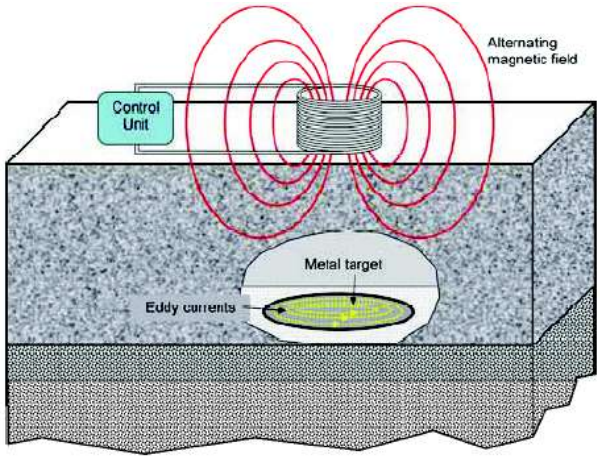

(a)

(b)

(c)

Figure 2.17 Magnetic topography (a) working principle; (b) thickness measurement; (c) dowel bar measurement (http://www.mit-dresden.de/, Oct. 30 2010).

2.1.4 Other Nondestructive Evaluation Techniques

There are also some other NDE tools used for airport pavement evaluation belonging to none of the above categories. In this section, the applications of two of these other tools, intelligent compactor and surface friction measurement equipment, will be

discussed.

2.1.4.1 Intelligent compaction

Intelligent compaction (IC) rollers were designed to offer real-time pavement quality measurement with no negative impact to the contractor's progress. As illustrated in Figure 2.18, these rollers are equipped with instrumentation fed to a documentation and feedback control system that processes the data in real time for the roller operator. Compaction meters or accelerometers are mounted in or about the drum to monitor applied compaction effort, frequency, and response from the material being compacted. The readings from this instrumentation determine the effectiveness of the compaction process. But, the methodology to calculate material response to compaction is often proprietary. For asphalt IC rollers, additional temperature instrumentation is used to monitor the surface temperature of the asphalt pavement material. This is critical, as vibratory compaction in certain temperature ranges can have adverse effects. Although these roller-mounted systems are demonstrably beneficial to a contractor from a control standpoint, they have not been used for acceptance and confirmation of the design-modulus values. Compacting asphalt pavement materials involves the added complexity of a modulus that is affected by temperature, loading rate, and stiffness of base layers. Therefore, it remains unknown if any measured increases in stiffness are the result of an increase in density or a reduction in temperature (Chang et al. 2010).

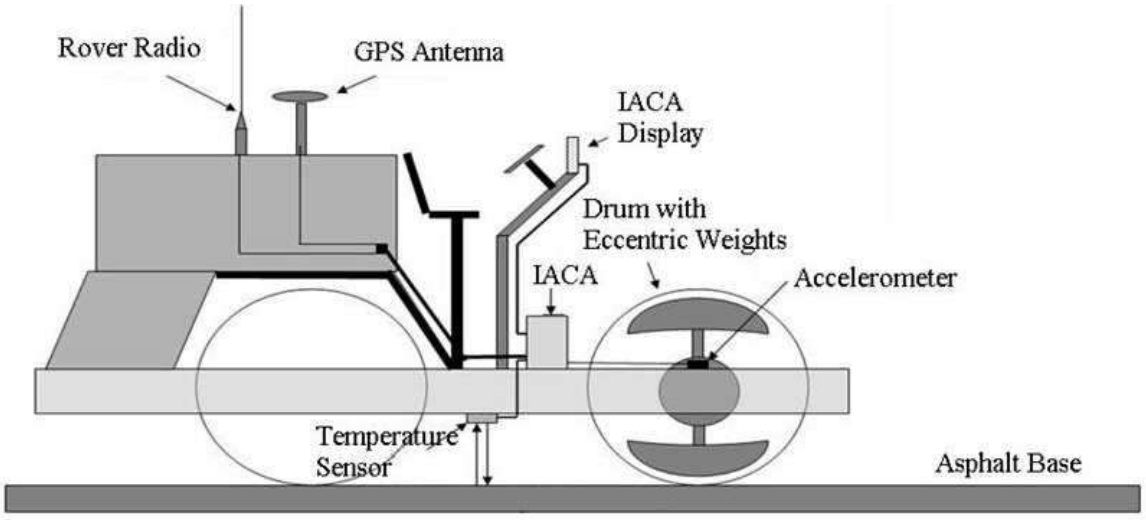

Figure 2.18 Functional schematic of the intelligent compactor (Commuri and Lemon 2007).

**IACA in this figure represents Intelligent Asphalt Compaction Analyzer*

2.1.4.2 Surface friction measuring equipment

Critically important to driving safety, surface friction is a functional property of pavement. Various NDE devices have been used to measure road surface friction. The principle of measurement differs among these devices, but they all fall within one of five different types: deceleration devices, locked-wheel devices, side-force devices, fixed-slip devices, and variable-slip devices (Loulizi 2001). Deceleration devices measure the deceleration of the vehicle under full braking. One of the known devices that use this principle is the Coralba meter, which is simply installed in a vehicle preferably equipped with antilock brakes. The Coralba meter measures the deceleration of the vehicle after a sudden and severe brake is performed. Another method somewhat similar to that applied by the deceleration device is the stopping-distance method (ASTM E445). Locked-wheel trailers, as shown in Figure 2.19, are used by most U.S. States to measure the skid number, defined as 100 times the friction coefficient (ASTM E274). The test tire is installed in a trailer, which is towed behind the measuring vehicle at a speed of 64 km/h (40 mph). Water is applied in front of the test tire, a braking system is forced to lock the tire, and the resistive force is measured. Side-force devices maintain the test wheel in a plane at an angle to the direction of motion to measure the side force perpendicular to the plane of rotation. The British SCRIM, with a wheel yaw angle of 20º, is the most used device of this type. Another system used by several U.S. States is the Mu-Meter, which measures the side force developed by two yawed wheels. The Mu-Meter procedure is denoted as ASTM E670. Fixed-slip devices usually operate between 10% and 20% slip. Some devices known to operate with this principle are the FAA friction tester, the Saab Friction Tester, and the Grip Tester. Variable-slip devices measure friction as a function of slip between the wheel and the road surface. These devices give maximum information about the frictional characteristics of the tire and road surface. Two of the known variable-slip devices are the French IMAG and the Norwegian Norsemeter RUNAR and ROAR systems.

Figure 2.19 Locked-wheel trailer.

2.1.5 Summary

A summary of the NDE methods discussed above is presented in Table 2.1. These NDE methods are compared against one another according to the type of measured pavement properties as well as the ability to provide high-coverage volumetric, structural, and functional measurements. Note that here the coverage is in terms of the surface area or length of the pavement. As the table makes clear, GPR, infrared tomography, and intelligent compactor, in addition to the nuclear and nonnuclear density gauges, are the potential NDE tools for monitoring the volumetric properties of asphalt mixture. All three of these methods are capable of providing high-coverage measurement.

Table 2.1 Summary of NDE Methods for Airport Pavement Condition Assessment

Method Category	Method Name	Type of Measured Property			High-Coverage Measurement?
		Volumetric	Structural	Functional	
Deflection-Based Method	Static load deflection equipment		√		Not feasible
	Steady-state dynamic load deflection equipment		√		Not feasible
	Impulse load deflection equipment		√		Not feasible
	Continuous load deflection equipment		√		Yes
Stress Wave Method	Impact echo		√		Not feasible
	Ultrasonic pulse velocity		√		Not feasible
	Spectral analysis of surface waves		√		Not feasible
EM Method	Nuclear and non-nuclear density gauges	√			Not feasible
	Ground penetrating radar	√	√		Yes
	Infrared tomography	√			Yes
	Laser profiler			√	Yes
Others	Intelligent compactor	√	√		Yes
	Surface friction measurement equipment			√	Not feasible

The application of the infrared tomography method to monitor the asphalt mixture density is based on the assumption that the thermal energy emitted by the asphalt mixture is completely determined by its density. However, because the thermal energy received by the infrared camera is affected by many other factors, such as the ambient temperature, wind speed, and sky condition, this method is not appropriate for providing quantified density information. The principle of intelligent compaction involves adjusting the vibration amplitude and frequency of the roller drums based on the measured material stiffness

through certain auto-feedback systems. However, as the stiffness measured by the intelligent compactor depends not only on the density of the asphalt mixture but also on many other factors, such as the mixture temperature and loading rate and the stiffness of the underlying layer, this method cannot provide quantitative density measurement either.

On the other hand, the underlying principle of mixture density measurement using GPR is that the dielectric constant of the asphalt mixture is physically related to the volumetric properties and dielectric properties of its components. For a given mixture, the change to the air volume will cause the change to its bulk dielectric constant. Hence, if the necessary volumetric and dielectric properties of the mixture's components are known and the appropriate mathematical models are developed, GPR is able to provide the quantitative density of the asphalt mixture by measuring its dielectric constant. Therefore, among all available NDE methods, GPR is the only method capable of offering both continuous and quantitative measurement of the in-situ asphalt mixture density. Furthermore, GPR can accurately measure one of the structural properties of pavement (layer thickness) and simultaneously detect the distresses within pavement structure (such as water accumulation and large air void).

2.2 Principles of GPR Systems

The application of GPR is based on transmitting EM signals and analyzing the reflected signals from interfaces where there is dielectric contrast. Therefore, the foundations of GPR lie in the EM theory. This section reviews the basic EM principles needed to work quantitatively with GPR.

2.2.1 Electromagnetic Propagation

When EM waves propagate through a homogeneous medium, they are governed by Maxwell's equations and constitutive relations, which relate the electric and magnetic fields of the sources to the electrical properties of the medium. Maxwell's equations are a set of four partial differential equations that relate the electric and magnetic fields to their sources, charge density, and current density and their development with time. Individually, the equations, which are expressed below, are known as Faraday's law of induction, Ampère's law with Maxwell's correction, Gauss's law, and Gauss's law for magnetism:

$$\nabla \times \bar{E} = -\frac{\partial \bar{B}}{\partial t}, \tag{2.10}$$

$$\nabla \times \bar{H} = \bar{J} + \frac{\partial \bar{D}}{\partial t}, \tag{2.11}$$

$$\nabla \cdot \bar{D} = q, \tag{2.12}$$

$$\nabla \cdot \bar{B} = 0, \tag{2.13}$$

where $\bar{E}$ is the electric field strength vector (V/m); $\bar{B}$ is the magnetic flux density vector (T); t is the time (s); $\bar{H}$ is the magnetic field intensity (A/m); $\bar{J}$ is the electric current density vector (A/m^2); $\bar{D}$ is the electric displacement vector (C/m^2); and q is the electric charge density (C/m^3).

A material's response to EM fields is determined by its permittivity ε conductivity σ and permeability μ through the following constitutive equations:

$$\bar{J} = \sigma \bar{E}, \tag{2.14}$$

$$\bar{D} = \varepsilon \bar{E}, \tag{2.15}$$

$$\bar{B} = \mu \bar{H}. \tag{2.16}$$

The above constitutive equations are analogous to the stress-strain constitutive equations in structural analysis, familiar to civil engineers. The functions of a material's EM properties ε, σ, and μ are similar to that of the elastic modulus for elastic material, which connects an elastic material's mechanical response to the applied stress/load.

Conductivity, σ, is the inverse of resistivity, which measures a material's ability to conduct electric current. Permittivity, ε, on the other hand, shows a material's ability to be polarized and therefore its ability to store a charge in response to an applied EM field.

Magnetic permeability, μ, measures a material's susceptibility to magnetization (Loulizi 2001). Free space, which is considered a reference material, has a permittivity of ε_0 = 8.854×10^{-9} F/m and a permeability of $\mu_0 = 4\pi \times 10^{-7}$ H/m. Permittivity and permeability of other materials are usually expressed as a ratio to ε_0 and μ_0, which are called relative permittivity or dielectric constant, ε_r, and relative permeability, μ_r, respectively.

For a source-free medium and time-harmonic EM fields with angular frequency ω (assuming time variations in the form $e^{j\omega t}$), the following wave propagation properties can be obtained from Maxwell's equations (Lahouar 2003):

$$\alpha = \frac{\sigma}{2}\frac{\eta_0}{\sqrt{\varepsilon_r}}, \tag{2.17}$$

$$\beta = \frac{\omega}{c}\sqrt{\varepsilon_r}, \tag{2.18}$$

$$v = \frac{c}{\sqrt{\varepsilon_r}}, \tag{2.19}$$

where α is the propagation attenuation constant (Np/m), β is the phase constant (rad/m), v is the wave propagation speed, η_0 is the wave impedance of free space ($\eta_0 = \sqrt{\frac{\mu_0}{\varepsilon_0}} \approx 120\pi\ \Omega$), and c is the speed of light in free space ($c = \frac{1}{\sqrt{\varepsilon_0 \mu_0}} \approx 3 \times 10^8\ m/s$).

It should be noted that the dielectric constant is usually expressed as a complex number in which the real part denotes the energy storage in the media and the imaginary part denotes the loss due to dielectric effect (Lahouar 2003). However, because conduction loss is usually much higher than dielectric effect loss, the dielectric constant can be considered a real number, provided that conduction loss is accounted for using Equation 2.17. Moreover, the dielectric constants of most materials are dependent on the frequency of the EM waves. However, within the frequency range above 0.5 GHz, which is the case for most GPR systems used for pavement surveys, the dielectric constant of pavement materials does not vary significantly. Therefore, ε_r can be considered frequency-independent to facilitate the interpretation of pavement GPR data.

2.2.2 Electromagnetic Scattering

Similar to mechanical waves, EM waves will also scatter when they encounter a discontinuity in a medium. In the case of GPR surveys on a layered medium, the discontinuity can be either the interface between two homogeneous layers in the layered system or an irregularly shaped defect within a layer. Due to the discontinuity, the wave is reflected, refracted, or diffracted depending on the geometry of the discontinuity, the properties of the materials, the polarization of the fields, and the wavelength of the incident signal.

For a planar-layered medium, such as the pavement system, reflection from a planar surface can be only considered. The scattering will yield a reflected signal and a transmitted signal. The reflection and transmission coefficients can be determined using the boundary conditions at the interface. For an oblique incident wave, two solutions can be found for the reflection and transmission coefficients depending on the polarization of the incident fields.

Polarization of the incident fields is defined with respect to the plane of incidence, or the plane formed by the normal to the interface and the direction of propagation of the incident wave. As depicted in Figure 2.20, a transverse electric TE (or perpendicular) wave refers to a wave with the electric field perpendicular to the plane of incidence. A transverse magnetic TM (or parallel) wave refers to a wave with the electric field parallel to the plane of incidence (the magnetic field is therefore perpendicular to this plane). The reflection and transmission coefficients can be calculated using Equations 2.20 to 2.23 (Lahouar 2003).

For TE polarization:

$$\gamma_{\perp} = \frac{-\eta_1 \cos\theta_t + \eta_2 \cos\theta_i}{\eta_1 \cos\theta_t + \eta_2 \cos\theta_i}, \tag{2.20}$$

$$\tau_{\perp} = \frac{2\eta_2 \cos\theta_i}{\eta_1 \cos\theta_t + \eta_2 \cos\theta_i}. \tag{2.21}$$

For TM polarization:

$$\gamma_{//} = \frac{-\eta_1 \cos\theta_i + \eta_2 \cos\theta_t}{\eta_1 \cos\theta_i + \eta_2 \cos\theta_t}, \tag{2.22}$$

$$\tau_{//} = \frac{2\eta_2 \cos\theta_i}{\eta_1 \cos\theta_i + \eta_2 \cos\theta_t}, \tag{2.23}$$

where γ and τ are the reflection and transmission coefficients, respectively; η_1 and η_2 are the impedances of media 1 and 2, and the impedance is given by $\eta_{1,2} = \sqrt{\frac{\mu_{1,2}}{\varepsilon_{1,2}}}$; and θ_i and θ_t are the angles of incidence and transmission, which are related by Snell's law of refraction as the following equation:

$$\sqrt{\varepsilon_1}\, sin\theta_i = \sqrt{\varepsilon_2}\, sin\theta_t . \tag{2.24}$$

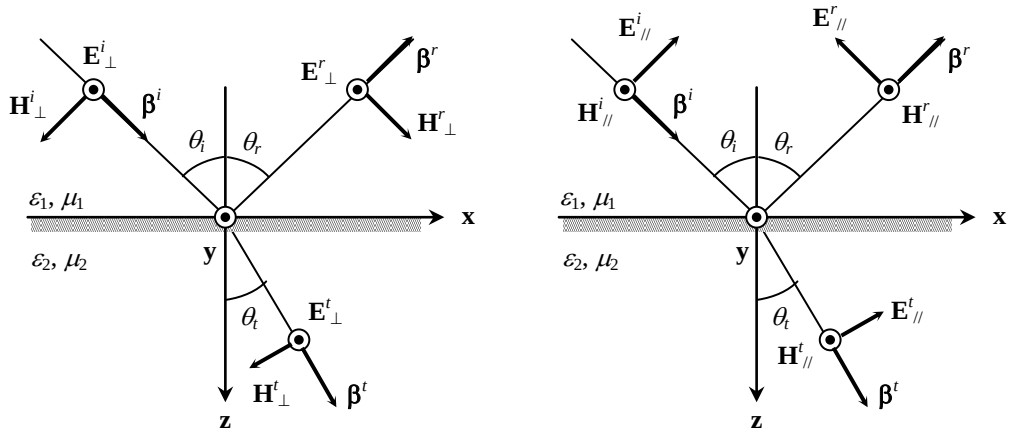

(a) (b)

Figure 2.20 Oblique reflection and transmission from a flat surface: (a) TE; (b) TM (Lahouar 2003).

Applying a normal incidence with θ_i and θ_t equal to zero, the reflection and transmission coefficients can be expressed as

$$\gamma = \frac{\sqrt{\varepsilon_{r,1}} - \sqrt{\varepsilon_{r,2}}}{\sqrt{\varepsilon_{r,1}} + \sqrt{\varepsilon_{r,2}}}, \tag{2.25}$$

$$\tau = \frac{2\sqrt{\varepsilon_{r,1}}}{\sqrt{\varepsilon_{r,1}} + \sqrt{\varepsilon_{r,2}}}, \tag{2.26}$$

where $\varepsilon_{r,1}$ and $\varepsilon_{r,2}$ are the dielectric constants of media 1 and 2.

2.2.3 Dielectric Constant Estimation

The application of GPR is based on the dielectric characteristics of transmission materials. The dielectric constant provides the basic information for obtaining the layer thickness and material condition in a GPR survey.

Currently, the most common method for estimating in-place pavement materials' dielectric constant is based on the amplitude of the reflection at the pavement surface. Figure 2.21 depicts a typical EM reflection from a layered system made of homogeneous and lossless materials. According to the surface-reflection method, the dielectric constant of the first layer, $\varepsilon_{r,1}$, can be estimated nondestructively from the GPR-collected signal, based on the following equation (Lahouar et al 2003):

$$\varepsilon_{r,1} = \left(\frac{1 + \frac{A_0}{A_p}}{1 - \frac{A_0}{A_p}} \right)^2, \tag{2.27}$$

where $\varepsilon_{r,1}$ is the dielectric constant of the first layer, A_0 is the amplitude of the surface reflection, and A_P is the amplitude of the incident GPR wave, which is obtained by collecting data over a copper plate place on the pavement surface. The amplitudes can be obtained directly from GPR data, as Figure 2.21 shows.

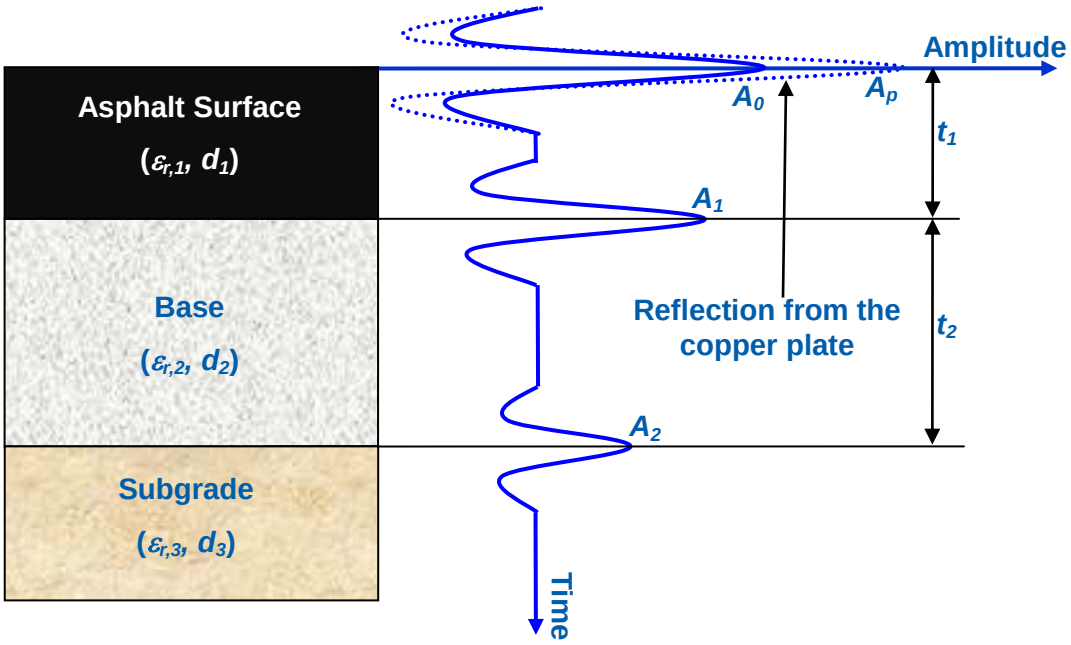

Figure 2.21 Typical reflections from the interfaces in pavements.

Once the dielectric constant of surface layer is known, the EM wave travel speed within this layer can be calculated using Equation 2.19. Thus, the thickness of the surface layer can be calculated by using the following equations:

$$d_1 = \frac{ct_1}{2\sqrt{\varepsilon_{r,1}}}, \tag{2.28}$$

where t_1 is the two-way travel time of the GPR signal within the surface layer, which can be obtained from GPR data.

2.2.4 Electromagnetic Mixing Theory

Ground penetrating radar measurements are seldom carried out on pure elements. Instead, almost all GPR work is conducted on materials that are composites or mixtures of many other materials or elements. For example, for a flexible pavement structure as shown in Figure 2.21, the surface layer is composed of asphalt binder, aggregate, air, and possibly water, and the materials in the base and subgrade consist of aggregate, air and possibly water.

Generally, if the dimensions of the mixtures' constituents are considerably smaller than the wavelength of the subjected EM wave, the scattering effect of the inclusions can be ignored and the bulk dielectric constant of the mixture can be considered to represent the whole mixture (Sihvola and Lindell 1989). As the free-space wavelength of the 2-GHz GPR signal is 150 mm (6 in) and the maximum aggregate size of the asphalt mixture is usually less than 25 mm (1 in), it is reasonable to treat the asphalt mixture as a homogeneous material for the EM waves of GPR with central frequencies equal to or less than 2 GHz.

Since the early work of Rayleigh, many mixing formulas designed to investigate the relationship between the bulk dielectric constant of a mixture and the dielectric constant of its components have been published. The equation derivation of a general mixing formula was provided by Sihvola (1989) for mixtures that contain spherical scatterers and is shown as the following.

Consider a mixture with background material of permittivity ε_0 containing *n* scatterers in unit volume, each of polarizability α. Note that the background need not be the free space. The effective permittivity or the bulk permittivity ε_{eff} of a random medium is defined as the ratio between the average displacement $\overline{D}$ and the average field $\overline{E}$ as follows:

$$\overline{D} = \varepsilon_{eff}\overline{E} . \tag{2.29}$$

The displacement depends on the polarization $\overline{P}$ in the material:

$$\overline{D} = \varepsilon_0\overline{E} + \overline{P} . \tag{2.30}$$

The polarization can be calculated from the dipole moment $\overline{p}$ of the scatterers; it is the dipole moment density in this polarizable material:

$$\overline{P} = n\overline{p} , \tag{2.31}$$

where *n* is the number of scatters. This treatment assumes that the dipole moments are the same for all scatters. If there are different polarizabilities, they have to be summed by

weighing each dipole moment with its number density; the polarization consists of a sum or integral.

The dipole moment depends on the polarizability and the exciting field $\bar{E}^e$:

$$\bar{p} = \alpha \bar{E}^e . \tag{2.32}$$

For spherical scatters, the exciting field is

$$\bar{E}^e = \bar{E} + \frac{\bar{P}}{3\varepsilon_0} . \tag{2.33}$$

Therefore, the effective permittivity is

$$\varepsilon_{eff} = \varepsilon_0 + 3\varepsilon_0 \frac{n\alpha}{3\varepsilon_0 - n\alpha} . \tag{2.34}$$

This equation can also be written in the form of

$$\frac{\varepsilon_{eff} - \varepsilon_0}{\varepsilon_{eff} + 2\varepsilon_0} = \frac{n\alpha}{3\varepsilon_0} . \tag{2.35}$$

It is worth noting that the scatterers in the mixture need not be of the same size. As long as each of the scatters satisfied the quasi-static requirement, their relative polarizabilities are the same and must be multiplied with the volume fraction to sum to the average polarization. On the other hand, if the mixture contains scatterers with different polarizabilities such as, in the simplest case, spheres of *N* different permittivities, they must be multiplied by their individual volume fractions, and Equation 2.35 is modified into

$$\frac{\varepsilon_{eff} - \varepsilon_0}{\varepsilon_{eff} + 2\varepsilon_0} = \sum_{i=1}^{N} \frac{n_i \alpha_i}{3\varepsilon_0} . \tag{2.36}$$

The use of this formula requires that the different types of scatterers be distributed homogeneously in the mixture when regarding scales of the order of wavelength.

The simplest mixture consists of a background medium and spherical scatterers.

The polarizability of this kind of scatterer depends on the field ratio between inside and outside fields when the scatterer is in a static field. The polarizability of a scatter with radius a_i is

$$\alpha_i = 4\pi a_i^3 \varepsilon_0 \frac{\varepsilon_i - \varepsilon_0}{\varepsilon_i + 2\varepsilon_0}. \tag{2.37}$$

Hence, according to Equation 2.36, the effective permittivity of the mixture is

$$\frac{\varepsilon_{eff} - \varepsilon_0}{\varepsilon_{eff} + 2\varepsilon_0} = \sum_{i=1}^{N} \frac{4\pi a_i^3 n_i}{3} \frac{\varepsilon_i - \varepsilon_0}{\varepsilon_i + 2\varepsilon_0}. \tag{2.38}$$

Since the volume of n_i spheres of radius a_i is calculated by

$$V_i = \frac{4\pi a_i^3 n_i}{3}, \tag{2.39}$$

Equation 2.38 can be rewritten as

$$\frac{\varepsilon_{eff} - \varepsilon_0}{\varepsilon_{eff} + 2\varepsilon_0} = \sum_{i=1}^{N} V_i \frac{\varepsilon_i - \varepsilon_0}{\varepsilon_i + 2\varepsilon_0}. \tag{2.40}$$

This formula is known as the Rayleigh mixing formula. As two extreme cases: when there is no scatterers (i.e. $V_i = 0$), the effective permittivity $\varepsilon_{eff} = \varepsilon_0$; and when the mixture is full of one scatterer and no background material (i.e. $V_1 = 1$), the effective permittivity $\varepsilon_{eff} = \varepsilon_1$. These are two basic requirements for a good mixing formula.

However, it should be noted that Equations 2.33 and 2.37 apply when a scatterer is situated in an unbounded homogeneous material of permittivity ε_0. For sparse mixtures where the distance between scatterers is big, the derivation and the result are probably justified because the perturbation field of a scatterer possesses a $1/r^3$-like distance dependence, and its effect is small even at regions of the nearest neighboring scatterers. For dense mixtures, the analysis requires more consideration, and the Rayleigh mixing formula should be modified accordingly.

A quasi-heuristic consideration gives the following result for the effective permittivity:

$$\frac{\varepsilon_{eff} - \varepsilon_0}{\varepsilon_{eff} + 2\varepsilon_0 + v(\varepsilon_{eff} - \varepsilon_0)} = \sum_{i=1}^{N} V_i \frac{\varepsilon_i - \varepsilon_0}{\varepsilon_i + 2\varepsilon_0 + v(\varepsilon_{eff} - \varepsilon_0)}. \tag{2.41}$$

where, parameter v can be seen as an indicator of how the polarization of neighboring inclusions is taken into account in calculating the dipole moment of a single scatter. Here, the coefficient $v = 0$ can be seen as yielding the classical Rayleigh mixing formula. When the coefficient $v = 2$, the mixing formula becomes

$$\frac{\varepsilon_{eff} - \varepsilon_0}{3\varepsilon_{eff}} = \sum_{i=1}^{N} V_i \frac{\varepsilon_i - \varepsilon_0}{\varepsilon_i + 2\varepsilon_{eff}}. \tag{2.42}$$

This formula is widely known as the Bottcher mixing formula. Also, the case $v = 3$ leads to

$$\frac{\varepsilon_{eff} - \varepsilon_0}{4\varepsilon_{eff} - \varepsilon_0} = \sum_{i=1}^{N} V_i \frac{\varepsilon_i - \varepsilon_0}{\varepsilon_i + 3\varepsilon_{eff} - \varepsilon_0}, \tag{2.43}$$

which is known as the Coherent potential formula.

In addition to the above models, a widely used class of mixing models are formed by the “power-law” approximations:

$$\varepsilon_{eff}^{\beta} = \sum_{i=1}^{N} V_i \varepsilon_i^{\beta}, \tag{2.44}$$

where, β is an empirical power parameter. This type of model follows a simple principle: a certain power of the permittivity is averaged by volume weights. The most commonly used value of the parameter β is 1/2. When β = 1/2, the mixing formula is referred to as complex refractive index model.

There are also many other EM mixing models available (Sihvola 1999). However, most of these other models were developed for some specific mixtures and are usually more complicated. The multiplicity of mixing formulas presented in the literature reflects that an exact solution for the electromagnetic problem with random parameters and

boundaries is not yet available. This has led to the existence of several mixing theories demanding experimental confirmation.

2.3 GPR Applications to Pavements

GPR research in pavement engineering was initiated in the mid-1970s by the Federal Highway Administration to investigate the feasibility of radar in tunnel applications (Black and Kopac 1992). Since then, GPR applications for pavement structure evaluation have been extended to a wide range of areas. The applications generally considered to be established include:

- the measurement of pavement layer thicknesses;
- the detection of pavement distresses;
- the determination of depth and alignment of steel bars; and
- the estimation of density and air void.

In this section, the current state of knowledge about these applications will be presented.

2.3.1 Layer Thickness Measurement

Layer thickness measurement is by far the most common and successful application of GPR in pavement survey. The GPR thickness data has been collected for the purposes of: (a) overlay design and prediction of pavement service life, (b) support of other testing techniques, such as FWD testing, and (c) QA when new pavement systems are constructed or old pavements are overlaid.

The ability of GPR to measure asphalt and base thickness has been extensively documented, although different investigators have reported various GPR performances depending on the site surveyed and the GPR data analysis technique used. For an old pavement system (specifically, a segment of Interstate 81), Lahouar et al. (2002) reported an average error of 6.8% in estimating the thickness of asphalt pavement layers ranging from 280 to 350 mm (11 to 14 in) thick, while a mean error of 3.8% for an AC layer thickness range of 100mm to 200mm (4 to 8 in) was reported for a new pavement system at the Virginia Smart Road. In another study, Maser (1996) reported thickness accuracies of ±7.5% for asphalt layers with thicknesses ranging from 51 to 500 mm (2 to 20 in) and

±12% for granular base layers with thicknesses ranging from 150 to 330 mm (6 to 13 in). Loizos and Plati (2007) reported an average error of between 5% and 10%, depending on the dielectric constant estimation technique utilized. Al-Qadi et al. (2001) conducted GPR surveys on a test section of Route 288 in Richmond, Virginia, to evaluate the performance of the GPR when it was used as a QA-QC tool for a newly built pavement system. GPR data were collected over the granular base layer and the three different asphalt layers in the pavement test section after each layer was laid down. Measurements were taken approximately five hours after the asphalt mixture was laid down. A comparison of the GPR thicknesses to the thicknesses measured directly from field cores revealed an average error of 2.9%. It was concluded that the relatively high accuracy of the GPR tool in this case was due to the homogeneity of the layers, as they were newly constructed at the time of the survey.

It should be noted that in all the aforementioned studies, the surface reflection method with one air-coupled GPR system was used to calculate the material dielectric constant for pavement thickness measurement (Al-Qadi and Lahouar 2005a). This yields greater accuracy in computing GPR thickness for new pavement due to new pavement's relatively uniform properties. Al-Qadi et al. (2003) utilized the modified common midpoint method with an air-coupled GPR system and a ground-coupled GPR system to measure the average dielectric constant of an asphalt layer. This technique yielded a mean thickness error of 6.8% for the GPR data collected from a 27-km portion of I-81. The researchers concluded that the errors were mainly attributable to the inaccurate localization of the surface reflection from the ground-coupled antenna, which was usually overlapped with the coupling pulse. To simplify and expedite the data procession, various programs have been developed by researchers to automatically calculate the pavement layer thickness using GPR data (Lahouar and Al-Qadi 2008; Olhoeft and Smith III 2000).

Thickness measurements using GPR for concrete pavements are not as successful as those for flexible pavements because detecting the reflection from the concrete-base course interface can be difficult (Cardimonda et al. 2003). This difficulty has been attributed mainly to two factors: the similar properties of concrete pavement and base course and the higher signal attenuation in the concrete.

2.3.2 Distress Detection

In addition to pavement thickness measurement, another common application of GPR to pavements is pavement distresses detection. The distresses potentially identifiable by GPR mainly include the stripping of asphalt mixture, the voids beneath pavements, and the delamination of pavement interface.

Stripping in asphalt mixture is a moisture-induced distress that occurs when the bond between the asphalt and aggregate is broken by the penetrating water, leaving an unstable low-density layer in the asphalt. The Texas Transportation Institute has conducted several surveys to identify the presence of stripping within existing pavements (Saarenketo and Scullion 1994). These surveys indicated that the existence of severe stripping in surface layer would cause an additional peak between the surface and base reflections. However, as similar reflection can be received from an internal asphalt layer with different electrical properties, it is recommended that cores and FWD data be used to confirm the interpretation (Saarenketo and Scullion 2000). It should be noted that GPR works only if there are significant differences in electric properties between layers. Therefore, when stripping problems are in their early stages and therefore have not yet produced significant electric property change, it is impossible for GPR to detect them. In addition, when the pavement is tested under dry or wet conditions, the signatures for the stripping will be different. When the stripping layer is dry, a negative peak will be observed due to its lower density and therefore lower dielectric constant. When the stripping zone is saturated, a positive peak will be found due to the extremely high dielectric constant of the accumulated water. Hammons et al. (2006) proposed using the GPR Uniform Index—which equates to the GPR amplitude at a specific location and depth range of interest divided by the average GPR amplitude over a normalization range—as an indicator of asphalt stripping. Based on the index, the roadway was segmented into features that could be used to plan seismic testing and coring operations to further verify and confirm the stripping areas.

The nondestructive mapping of voids under concrete pavement is of interest to pavement engineers because of the loss of pavement support. Generally, voids occur beneath joints in which water enters the soil and, aided by the pumping action of traffic, carries out the fine materials. The earliest study investigating the feasibility of using GPR to locate and measure voids beneath pavements dates to 1981 (Steinway 1981). In this

study, a 1-GHz air-coupled mine detection radar was used. It was found that GPR was capable of locating voids to within 150 mm (6 in) in length and 216 mm (8.5 in) in depth with a standard deviation of error of less than 13 mm (0.5 in). Although void detection is one of the earliest applications of GPR for pavements, unsatisfactory results have often been reported (Morey 1998, Al-Qadi 2002). One problem when using GPR to detect the voids beneath concrete slabs is the moisture content of voids; when the voids are dry, semidry, or saturated, the GPR reflection pattern looks completely different. Also, the presence of reinforcement can affect the ability of GPR to successfully identify voids below it. Despite these, GPR still offers a useful tool for void detection. A recent study claims the potential of a 400-MHz ground-coupled GPR to locate voids with depths ranging from 50 to 400 mm (2 to 16 in) and to locate other voids beneath reinforcement, although drilling and coring were recommended for determining the extent and depth of the void (Chen and Scullion 2008). Given the small depth of void underneath concrete slabs, its detection is always a challenge (Al-Qadi 1996).

Spalling, a common type of distress for all types of concrete pavements affects pavement quality, such as smoothness and ride quality. Early-age delamination, which typically develops at a shallow depth below the pavement surface, is a main contributor to the occurrence of spalling. In an early study (Joyce 1985), GPR was used as a network-level tool to quickly assess the general conditions of bridge decks with respect to delaminations. The results of the evaluation were encouraging, as distressed areas with a longitudinal dimension of 0.6 m (2 ft) or more could be detected. Data interpretation, however, was subjective, being based primarily on qualitative differences in apparent wave velocity and/or attenuation of the inspection wave. Huston et al. (2000) used a custom-designed stepped frequency GPR system to detect delamination in roadways. Delamination as small as 1 mm (0.04 in) was detected in the laboratory. However, their laboratory findings were not supported by the field measurements.

A research project was undertaken by Rhazi et al. (2003) to determine GPR's real capacity for detecting delamination in concrete bridge decks. Several concrete bridge decks with asphalt coating were evaluated by four GPR systems. The study concluded that despite the progress made in the field of radar antennas, it was still impossible for the actual GPR systems to detect delamination clearly and without ambiguity. The researchers concluded that the low dimension of delamination, the proximity of the delamination to the

reinforcement, and the insufficient resolution to radar antenna were the main factors causing the difficulty.

Other studies have called into question the application of GPR in detecting debonding between pavement layers. Even at frequencies of 1 to 2 GHz, the GPR wavelengths in asphalt are too long to resolve thin debonding. Numerical modeling of the GPR signals in the case of debonded asphalt was carried out by Smith and Scullion (1993). Their results indicated that an air-filled delamination of 5.0 mm (0.2 in) or larger and water-filled debonding of 2.5 mm (0.1 in) and larger at a minimum depth of 50 mm (2 in) may be detected using a 2.5 GHz GPR antenna. The suggested maximum speed for data acquisition was 16 km/h (10 mph). Based on other field investigations, the GPR survey may provide useful information that may indicate debonding between asphalt layers. For example, the much larger amplitudes in GPR image mark the location of the debonded zones. Based on the available literature, detection of delamination between asphalt lifts, especially at its early stage of development, is highly challenging and demands further systematic investigation. More likely, successful results may be achieved indirectly by using the technology to measure the condition associated with the presence or development of delamination in pavement. For example, given the high sensitivity of GPR signals to changes in moisture, the penetration of moisture within the delaminated region may be detected and, thus, may assist in identifying delamination. A combination of GPR with other NDT technique(s) that directly detect delamination may yield the best outcome.

2.3.3 Steel-Bar Alignment and Depth Determination

Of the various types of materials that may be found within pavement structures, metal provides the largest contrast in dielectric properties compared to other pavement materials. Hence, the ability to locate steel bars in concrete pavement is well established. Recommended uses in reinforced pavements mainly include determination of rebar depths and checking of misalignments of dowel bars (UK Department of Transport 2001).

When GPR scans are collected from a reinforced pavement surveyed transversally to the rebars, the rebars will result in a signature with a parabolic shape in the B-scan GPR image (GPR signal scans stacked against survey distance). Al-Qadi and Lahouar (2005b) developed the image-processing techniques that can be used to extract the classic parabolic shape resulting from the rebar reflection. By fitting the extracted points to a

theoretical reflection model, the location of the rebar, the dielectric constant at the location, and the rebar cover depth were determined from the model parameters. GPR data collected from a continuous reinforced concrete pavement section with a known structure showed that the technique has a 2% error in estimating cover depth.

Because the visual representation in GPR image can bear little resemblance to the shape or size of the sub-surface bar, recent years have seen the development of many automatic algorithms for interpretation. Neural networks potentially offer considerable scope for automatic interpretation of radar results (Newnham and Goodier 2000, Shaw et al. 1998). However, success has so far been limited to straightforward cases such as reinforcing bar location. Bar sizing is more difficult and there is little evidence of industrial usage.

2.3.4 Density and Air Void Estimation

Asphalt mixture air void content or density, is one of the most important factors affecting the life span and deformation properties of pavements. Although there have been several attempts to estimate the air void or density of asphalt pavement using GPR, this application is still in its development stage and, consequently, the relevant literature is limited.

The first attempt to use GPR measurement to predict the volumetric property of asphalt mixture was made by Al-Qadi (1992), who developed regression models to predict the volumetric moisture content of asphalt mixture based on its dielectric constant. Although the focus of this study was to predict the moisture content of asphalt mixture, the same principle could be applied to the air void content prediction.

Lytton (1995) created a computer program to predict the density and water content of the various layers within a multilayer system using conventional GPR (U.S. Patent No. 5384715). The software, named System Identification and Analysis of Subsurface Radar Signals (SIDARS), takes advantage of the fact that each pavement layer is composed of three types of material: solids, fluids, and gases. Thus, the dielectric constant of a pavement layer is a function of the layer's solid, fluid, and gas dielectric constants. A wave propagation model of the pavement system is employed in SIDARS to generate a synthetic reflected radar signal. Initial values for a layer's solid, fluid, and gas concentrations are adjusted through iterative process to minimize the mean-squared-error

between the measured reflected and calculated synthetic radar signals (Lytton 2000). By calibrating the model embedded in the software to ground truth data obtained from cores, the volume and weight compositions of the layer can be calculated (Wells et al. 2001).

Saarenketo (1997) is one of the first researchers in Europe to use GPR to measure asphalt pavement density. His study was also based on the concept that the dielectric constant of a pavement can be assumed to be a function of the dielectric constants of its components. Therefore, changes in their proportions (e.g., in void content) can be measured by recording the overall dielectric constants of the pavement. The components of the asphalt mixture include asphalt, aggregate, air, and possible water. The dielectric constants for asphalt usually remain in the range of 2.6 to 2.8, those for crushed dry aggregate vary between 4.5 and 6.5, and those for air stand at 1. Although the dielectric constant of water is dependent on the degree to which it is bound, it was found that water does not have any appreciable effect on the dielectric constant measurements of new pavement. Laboratory tests were performed to correlate dielectric constant to density of dry asphalt mixture. Based on their research, Finnish researchers concluded that an exponential relationship exists between the surface dielectric constant and void content:

$$void(\%) = a \cdot e^{-b \cdot \varepsilon_{AC}}, \tag{2.45}$$

where ε_{AC} represents the surface dielectric constant, which can be obtained with horn antennas at highway speed, and coefficients *a* and *b* are calibration constants dependent on mixture type and can be determined from field cores. GPR data collected from various roads proved that the drop in dielectric value indicates density problems. Most significantly, the study demonstrated that GPR offers tremendous potential for assisting in monitoring the localized problem (Scullion and Saarenketo 2000).

Silvast (2001) used GPR technology to measure the runway air void content at the Helsinki-Vantaa airport in Finland. The purpose of the project was to evaluate the effectiveness of GPR application for runway-pavement quality control. GPR data were collected on a pavement area 900 m (2700 ft) long and 60 m (180 ft) wide containing 8 parallel lanes. Approximately three hours were spent on the data collection. The dielectric constant of the pavement was calculated using the surface reflection technique. Calibration samples were taken from three lanes, and void content values of these

samples were used to calibrate the void content based on dielectric values. The survey was carried out at 50 to 70 km/h (90 to 112 mph). During data processing, the void content was calculated at 5 m (15 ft) mean values. The study concluded that GPR technology presented a functioning pavement QC method for runways. More broadly, the study verified speed and large coverage as advantages offered by GPR over traditional methods and also exemplified GPR's effectiveness in monitoring changes in pavement quality and pavement structure over time.

Two nondestructive testing methods, infrared imaging and GPR, were applied in Texas to evaluate the density uniformity of asphalt overlays (Sebesta and Scullion 2002). Data were collected from TxDOT overlay projects on US-79, IH-10, and US-290 during the summer of 2001. Using the exponential equation proposed by the Finnish researchers, the relationship between the surface dielectric constants and voids were regressed using cores taken from the field, and the air void content profile for the whole pavement was then predicted. By comparing two testing methods, this research concluded that GPR is a much better tool for investigation than the infrared devices if density changes are the primary heterogeneities in the new asphalt surface. The researchers also recommended the maximum values of dielectric constant reductions, which are 0.8 for coarse-graded mixes and 0.4 for dense-graded mixes, to meet the TxDOT density profile specification.

CHAPTER 3 RESEARCH APPROACH

This chapter presents the details of the research approach implemented in this study to achieve the stated research objective, the development of the theoretical models and implementation algorithm for using GPR as an NDE tool for in-situ asphalt mixture density measurement.

As stated in Chapter 2, GPR surveys can yield the estimated dielectric constant of the asphalt mixture by using Equation 2.27. According to the EM mixing theory, the dielectric constant of an asphalt mixture is a function of the dielectric and volumetric properties of its components, i.e., air, asphalt binder, and aggregate, yielding a direct physical relation between the dielectric constant of an asphalt mixture and its density. Consequently, if validated mathematical models between the asphalt mixture dielectric constant and its density can be developed, it is feasible to predict the asphalt mixture density through a GPR survey by following the procedure illustrated in Figure 3.1. Note that in this figure, the bulk specific gravity of asphalt mixture (G_{mb}) is equal to the bulk density of asphalt mixture divided by the density of water at 4 ^{o}C (1 g/cm^3), and therefore is numerically the same as the bulk density of the asphalt mixture in g/cm^3. G_{mb} will be used in this dissertation to describe the asphalt mixture's density, because this density index is commonly used in pavement engineering.

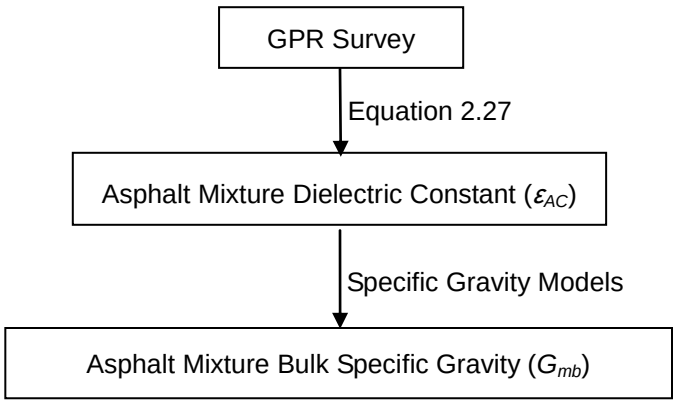

Figure 3.1 Outline of asphalt mixture density prediction through a GPR survey.

It is clear in Figure 3.1 that the two critical factors for the asphalt mixture density

prediction are the validity of the specific gravity models, and the accuracy of the estimated asphalt mixture dielectric constant. In addition, an appropriate implementation algorithm is also needed to employ this procedure in practice. Correspondingly, the research tasks as shown in Figure 3.2 were proposed for this study.

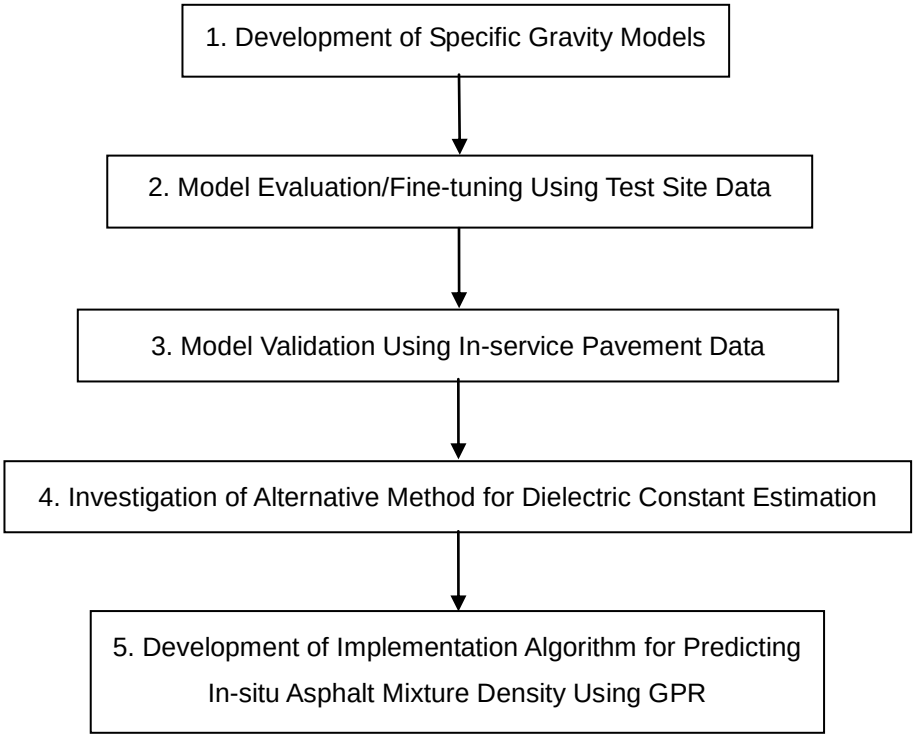

Figure 3.2 Research tasks.

In the first task, two candidate specific gravity models were developed based on the EM mixing theory described in Chapter 2. In the second task, a full-scale six-lane test site with four sections in each lane was carefully designed and constructed. GPR data collected from the test site were used in combination with the developed models to predict the in-situ asphalt mixture density of each test section. The predicted density values by the two models were compared to the ground truth data to evaluate the performance of the two models. Model fine-tuning was then followed to find the best-performance model for the test site data. In the third task, the performance of the selected best-performance model in the second task was validated using the data collected from in-service pavement

sections, which are located in Chicago area. In the fourth task, a new method, namely, the extended common mid-point method using two air-coupled antenna systems, was investigated to improve the accuracy of the asphalt mixture dielectric constant estimation. In the final task, guidelines were developed to help pavement engineers predict the asphalt pavement density using GPR in practice, which include GPR equipment selection, asphalt mixture information collection, aggregate dielectric constant determination, GPR data collection, and asphalt mixture density prediction. The following sections provide the details for each research task.

3.1 Development of Specific Gravity Models

In Section 2.4, mixing models between the dielectric constant of a homogeneous mixture and the dielectric and volumetric properties of its components have been introduced. In this study, two of these mixing models, namely the Complex Refractive Index Model (CRIM) and the Bottcher mixing formula, were selected to develop the specific gravity models, which enable the prediction of the asphalt mixture bulk specific gravity from its dielectric constant. These two models were selected, because they had been successfully used in other areas, and their parameters are relatively easy to obtain. The Rayleigh model could also be a candidate for consideration in this study. However, this model was developed for sparse mixtures, while asphalt mixture is a dense mixture with aggregate particles in contact with each other.

When developing the specific gravity models in this study, the asphalt mixture was assumed dry. Thus, the components of the mixture included air, aggregate, and asphalt binder. Figure 3.3 shows a phase diagram of the asphalt mixture describing the asphalt mixture's composition and parameters. The volumetric and mass contributions of each component to the entire mixture are represented by V and M, respectively; and the specific gravity and dielectric constant of each component are G and ε, respectively. The details of the symbols used in the specific gravity model derivation are given on the right-hand side of Figure 3.3.

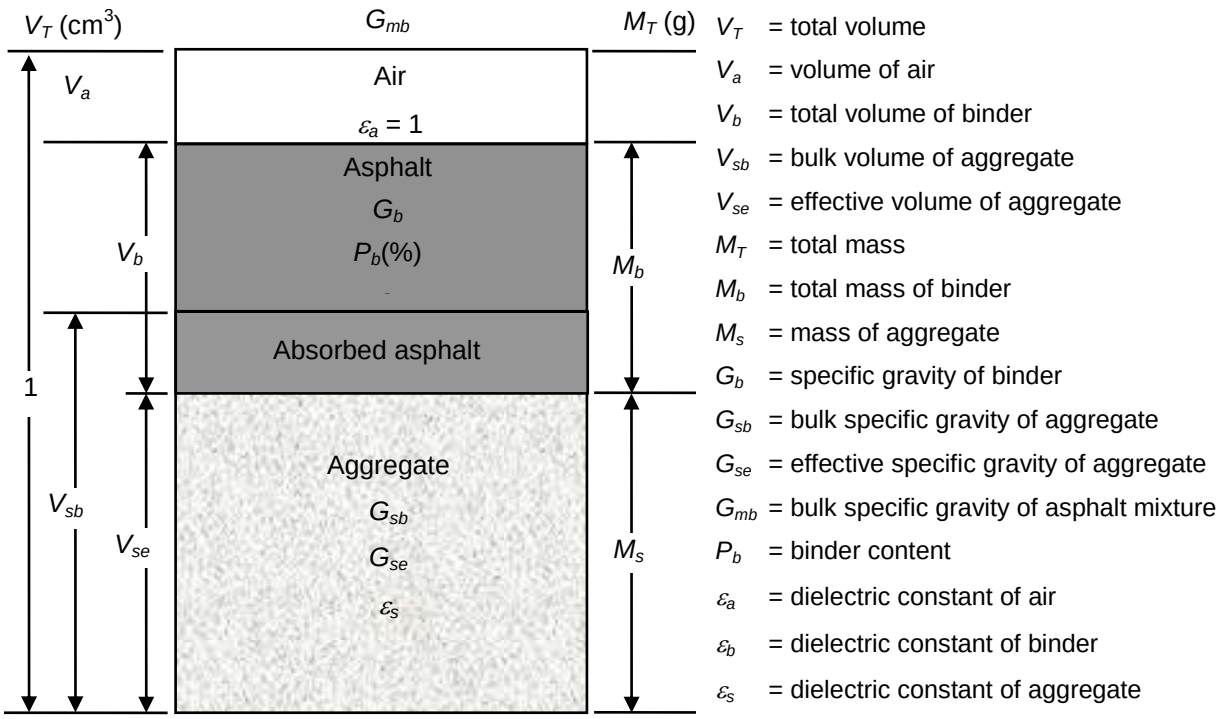

Figure 3.3 Asphalt mixture composition and parameters.

3.1.1 Modified Complex Refractive Index Model

Based on the complex refractive index model (CRIM) mixture theory (Equation 2.44), the dielectric constant of an asphalt mixture, ε_{AC}, can be estimated as follows:

$$\sqrt{\varepsilon_{AC}} = V_a\sqrt{\varepsilon_a} + V_{se}\sqrt{\varepsilon_s} + V_b\sqrt{\varepsilon_b}, \tag{3.1}$$

where all the parameters are as defined in Figure 3.3 and ε_a=1.

Assuming the total volume of the asphalt mixture, V_T = 1, the volumes of air, binder, and aggregate can be calculated using the following equations from the volumetric properties of the asphalt mixture:

$$V_a = 1 - \frac{G_{mb}}{G_{mm}}, \tag{3.2}$$

$$V_b = \frac{M_b}{G_b} = \frac{G_{mb} P_b}{G_b}, \tag{3.3}$$

$$V_{se} = \frac{M_s}{G_{se}} = \frac{G_{mb}(1 - P_b)}{G_{se}}, \tag{3.4}$$

where all parameters are as defined in Figure 3.3.

Substituting Equations 3.2, 3.3 and 3.4 in Equation 3.1 yields the following:

$$\sqrt{\varepsilon_{AC}} = (1 - \frac{G_{mb}}{G_{mm}})\sqrt{1} + \frac{G_{mb}(1 - P_b)}{G_{se}}\sqrt{\varepsilon_s} + \frac{G_{mb} P_b}{G_b}\sqrt{\varepsilon_b}. \tag{3.5}$$

And reorganizing Equation 3.5 gives the modified CRIM as follows:

$$G_{mb} = \frac{\sqrt{\varepsilon_{AC}} - 1}{\frac{P_b}{G_b}\sqrt{\varepsilon_b} + \frac{(1 - P_b)}{G_{se}}\sqrt{\varepsilon_s} - \frac{1}{G_{mm}}}. \tag{3.6}$$

3.1.2 Modified Bottcher Model

With the Bottcher mixing model, the effective dielectric constant ε_{eff} of a mixture, composed of a background material (dielectric constant ε_0) with *N* inclusions of different dielectric constants, is given by Equation 2.42.

In applying the Bottcher mixing model, this study assumed that the asphalt mixture is composed of an asphalt binder (dielectric constant ε_b) as the background material and that it includes spherical-shaped aggregates and air particles. From Equation 2.42, the asphalt mixture dielectric constant is given by the following equation:

$$\frac{\varepsilon_{AC} - \varepsilon_b}{3\varepsilon_{AC}} = V_{se}\frac{\varepsilon_s - \varepsilon_b}{\varepsilon_s + 2\varepsilon_{AC}} + V_a\frac{\varepsilon_a - \varepsilon_b}{\varepsilon_a + 2\varepsilon_{AC}}, \tag{3.7}$$

where all the parameters are as defined in Figure 3.3 and $\varepsilon_a = 1$.

Substituting Equations 3.2 and 3.4 in Equation 3.7 leads to the following:

$$\frac{\varepsilon_{AC}-\varepsilon_b}{3\varepsilon_{AC}}=\frac{G_{mb}(1-P_b)}{G_{se}}\frac{\varepsilon_s-\varepsilon_b}{\varepsilon_s+2\varepsilon_{AC}}+(1-\frac{G_{mb}}{G_{mm}})\frac{1-\varepsilon_b}{1+2\varepsilon_{AC}}. \tag{3.8}$$

Solving Equation 3.8 for G_{mb} yields the modified Bottcher model as follows:

$$G_{mb}=\frac{\frac{\varepsilon_{AC}-\varepsilon_b}{3\varepsilon_{AC}}-\frac{1-\varepsilon_b}{1+2\varepsilon_{AC}}}{\left(\frac{\varepsilon_s-\varepsilon_b}{\varepsilon_s+2\varepsilon_{AC}}\right)\left(\frac{1-P_b}{G_{se}}\right)-\left(\frac{1-\varepsilon_b}{1+2\varepsilon_{AC}}\right)\left(\frac{1}{G_{mm}}\right)}. \tag{3.9}$$

3.1.3 Sensitivity Analysis of Specific Gravity Models

Equations 3.6 and 3.9 are referred to in this study as the modified CRIM model and the modified Bottcher model, respectively. These two models can be expressed in the following simplified format:

$$G_{mb}=f_{\varepsilon_s,\varepsilon_b,P_b,G_b,G_{se},G_{mm}}(\varepsilon_{AC}), \tag{3.13}$$

where the bulk specific gravity of asphalt mixture, G_{mb}, is the model output, and the dielectric constant of asphalt mixture, ε_{AC}, is the model input. There are, in addition, six material property parameters: the dielectric constant of the aggregate (ε_s), the dielectric constant of the binder (ε_b), the asphalt binder content (P_b), the specific gravity of the binder (G_b), the effective specific gravity of the aggregate (G_{se}), and the maximum specific gravity of the asphalt mixture (G_{mm}). The values of P_b, G_{se}, and G_{mm} can be acquired from the mixture design. The values of G_b and ε_b are usually constant at around 1.015 and 3.0, respectively. The value of ε_s is dependent on the aggregate type and source. For example, the dielectric constant of limestone is usually within the range of 6 to 8, and the dielectric constant of granite is usually between 4 and 7.

To compare these two models, the variations of G_{mb} and air void content as a function of ε_{AC} for the two mixture theories are plotted in Figure 3.4 and 3.5, respectively. The typical values shown in Table 3.1 were assumed for the model parameters.

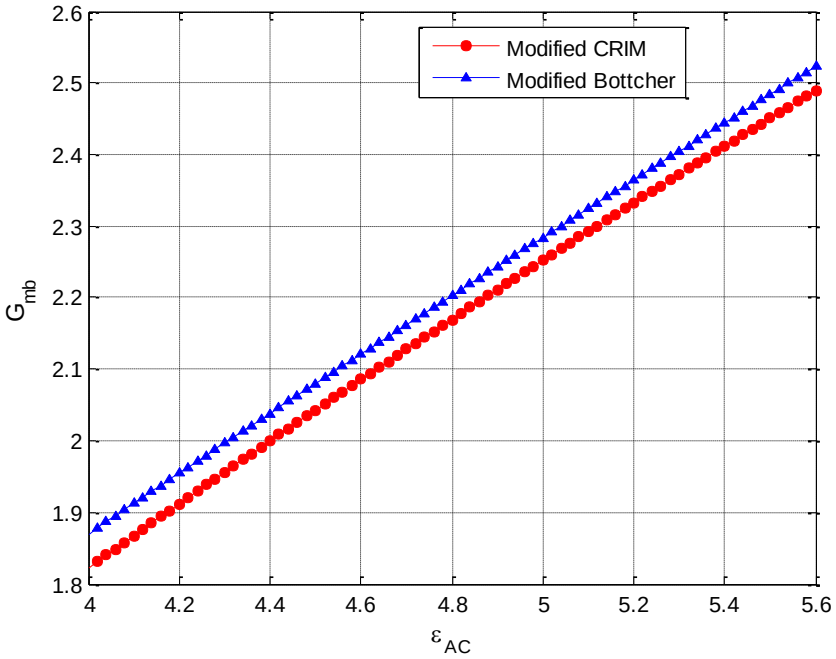

Figure 3.4 Variation of Gmb as a function of εAC.

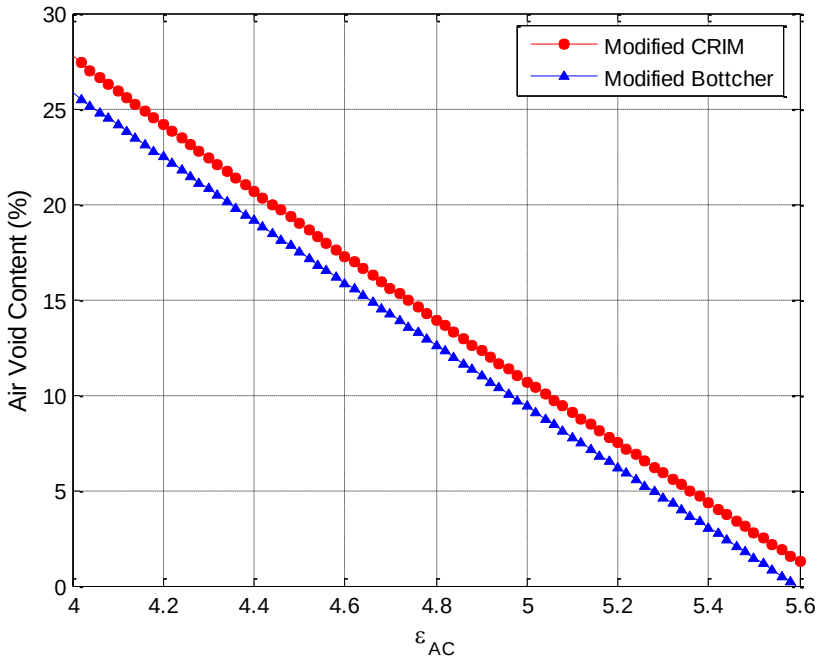

Figure 3.5 Variation of air void content as a function of εAC.

Table 3.1 Typical Values of the Parameters in Specific Gravity Models

Parameters	ε_s	ε_b	P_b	G_b	G_{se}	G_{mm}
Typical Value	6	3.0	5%	1.015	2.705	2.521

According to Figure 3.4, both models give similar results for the bulk specific gravity G_{mb} (e.g. for ε_{AC} = 5.2, G_{mb} = 2.334 from the modified CRIM model, and G_{mb} = 2.363 from the modified Bottcher model). The air void contents for the two models are also comparable as shown in Figure 3.5 (e.g. ε_{AC} = 5.2, AV = 7% from the modified CRIM model, and AV = 6% from the modified Bottcher model).

Figure 3.6 shows the G_{mb} sensitivity of the two models with respect to ε_{AC} errors, assuming ε_{AC} =5. For example, an ε_{AC} error of 10% gives a G_{mb} error of 8.8% for the modified CRIM model, and 8.7% for the modified Bottcher model. The error on the bulk specific gravity is at most equal to the error on the dielectric constant.

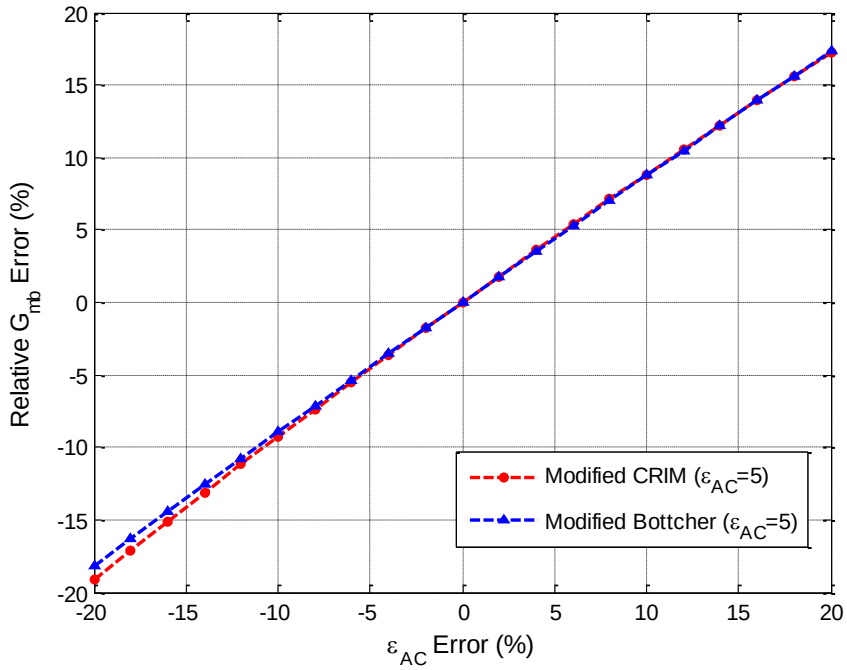

Figure 3.6 Relative Gmb error as a function of εAC error.

3.2 Model Evaluation and Fine-tuning Using Test Site Data

To evaluate the performance of the specific gravity models derived based on the EM mixing theory and find the best model(s) for asphalt mixture, this study first conducted some laboratory tests (Al-Qadi et al. 2009). As Figure 3.7 shows, GPR data were collected from 60cm*60cm*7.5cm (2ft*2ft*3in) asphalt mixture slabs prepared in the lab using the 2 GHz air-coupled antennas. The limestone aggregate and PG64-22 asphalt binder were used to prepare the mixture, and the measured air void contents of these slabs varied from 9.9% to 16.4%. As Figure 3.8 indicates, the preliminary laboratory testing results revealed a clear trend between the asphalt mixture's bulk specific gravity or air void content and its dielectric constant. However, the laboratory testing also found the following limitations:

1. The density levels of the slabs achieved in the lab, using the available compaction equipment, were much lower than the field values, which are usually within the range of 7% to 8% in term of air void content at the time of compaction and reduced to nearly 4% with traffic application.
2. Preparing the large laboratory testing slabs is very time and labor consuming.
3. Some edge effects existed in the lab-collected GPR data due to the GPR signal reflecting from the surrounding material of the testing slab.
4. Only one type of mixture was evaluated.

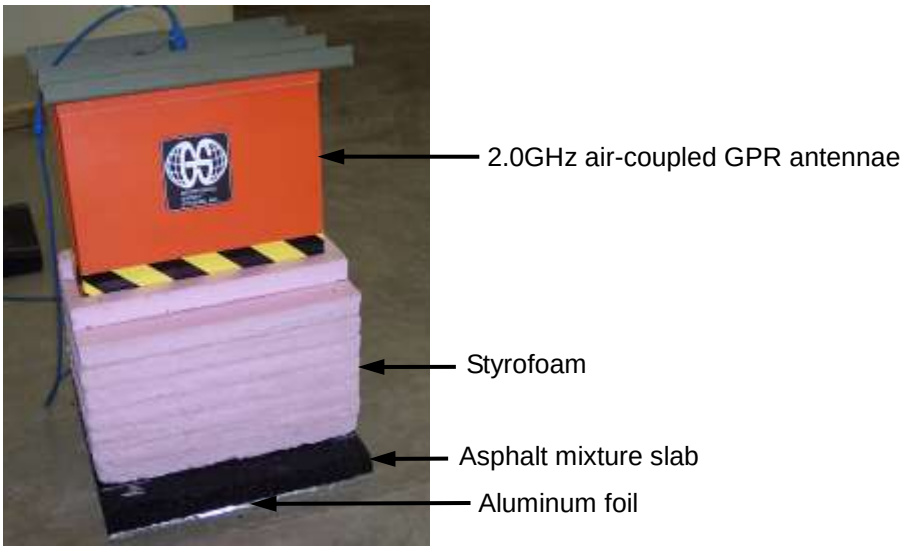

Figure 3.7 GPR test on asphalt mixture slab (Styrofoam is used under the antenna because it has the same dielectric constant as air, 1).

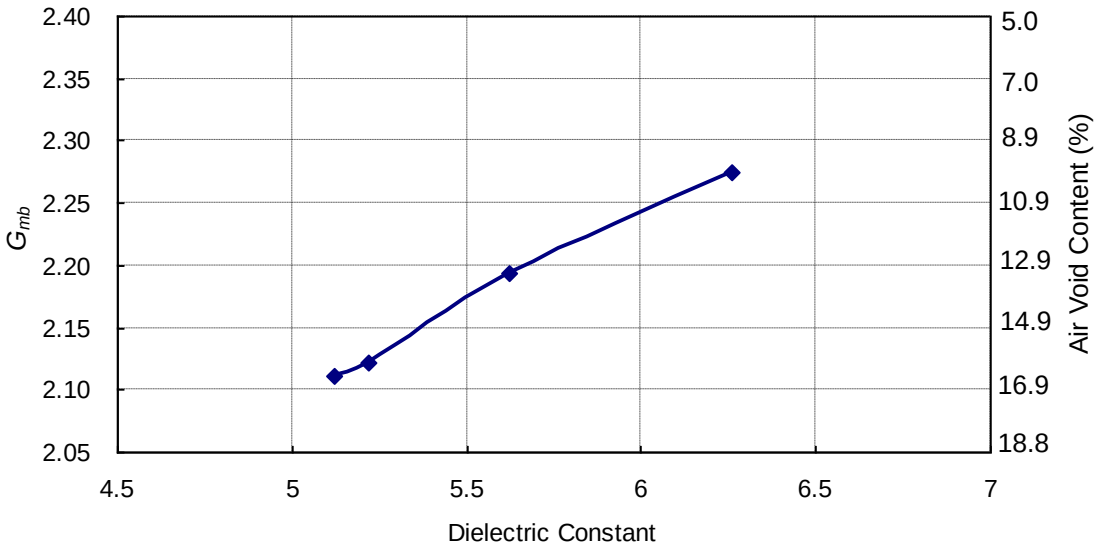

Figure 3.8 Relation between asphalt mixture's density and its dielectric constant in lab testing.

Due to the aforementioned limitations of the laboratory testing, it was then decided to design and build a full-scale test site for the model validation. Compare to the laboratory-prepared slabs, the full-scale test sections could provide a more realistic data input for the model evaluation, and at the same time have controllable test variables.

3.2.1 Test Site Design

To cover a wide range of asphalt mixtures, the test site design considered the following variables: mix type, aggregate type, asphalt type, asphalt content, air void content, and asphalt layer thickness. The levels of each variable to be evaluated are shown in Table 3.2. Based on these considered variables, three basic mix designs commonly used in construction practice were selected: one limestone surface mix, one granite surface mix, and one limestone binder mix. The designs of these three mixes are shown in Appendix A. To evaluate the effect of asphalt type, a fourth mix was added by changing the binder of the granite surface mix from PG 64-22 to PG 70-22. To evaluate the effect of the asphalt content on GPR data, a fifth mix was added that increased the asphalt content of the granite surface mix by 1%. Therefore, a total of five mixes were eventually chosen for use in the test site. Each of these mixes would be compacted in different

sections at four density levels: 4%, 6%, 9%, and 12% in terms of target air void content. Table 3.3 describes each mix that would be constructed in the test sections.

Table 3.2 Variables and Their Levels Considered in the Field Testing

Variable	Levels (Number of Levels)
Mix Type	Surface Mix and Binder Mix (2)
Aggregate Type	Limestone and Granite (2)
Asphalt Type	PG 64-22 and PG 70-22 (2)
Asphalt Content	Optimum and Optimum + 1% (2)
Air Voids	4%, 6%, 9%, and 12% (4)
Asphalt Layer Thickness	5, 10, 15, and 20 cm (2, 4, 6, and 8 in) (4)

Table 3.3 Mixes Used in Testing Site

Mix #	Mix Type	Nominal Maximum Aggregate Size (mm)	Asphalt Type	Asphalt Content
Mix I	Limestone Surface Mix	9.5	PG64-22	Optimum
Mix II	Granite Surface Mix	9.5	PG70-22	Optimum
Mix III	Granite Surface Mix	9.5	PG64-22	Optimum
Mix IV	Granite Surface Mix	9.5	PG64-22	Optimum+1%
Mix V	Limestone Binder Mix	19.0	PG64-22	Optimum

The selected test site location is at a large asphalt-surfaced parking lot at the Advanced Transportation Research and Engineering Laboratory (ATREL) of the University of Illinois. As shown in Figure 3.9, six lanes with four sections each would be constructed. Each test section was 3.6 m (12 ft) wide and 3.3 m (11 ft) long. A 3.9 m (13 ft) long transition section would be placed between the adjacent test sections in each lane. These transition sections were built to accommodate the compactor stopping and starting compaction to achieve the desired section density while maintaining section air void

content uniformity. Lane I(A) was designed to evaluate the effect of asphalt layer thickness. In this lane, the same mix (Mix I) would be compacted to the same density level (target air void content of 6%) but different thicknesses: 5, 10, 15, and 20 cm (2, 4, 6, and 8 in). Lanes I(B) to V were mainly designed to evaluate the effect of density on the GPR measurement when different mixes were used. Mixes I to V would be placed in Lanes I(B) to V, respectively. Each mix would be compacted to the same thickness (5 cm or 2.5 in) but different density levels (4%, 6%, 9%, and 12% in terms of target air void content). As illustrated in Figure 3.10, Lane I(A) would be constructed in four 5-cm-thick (2-in-thick) lifts, and Lanes I(B) to V would be constructed in one single 6.3-cm-thick (2.5-in-thick) lift.

In order to receive a clear GPR signal reflection at the bottom of each AC lift, 3.2-mm-thick (1/8-in-thick) steel plates were buried in each test section. Since the steel plates are perfect reflectors of the GPR signals, signifying that the GPR wave energy will be completely reflected by the steel plate, the locations of the asphalt layer bottom could be easily and accurately detected by identifying the strong steel plate reflections in the GPR signals. Note that these steel plates are not required for the GPR measurements in practice but were only used to validate the results in research. Figure 3.11(a) shows the steel plate layout in Lane I(A): one steel plate would be placed in each section before the construction of each new lift. After construction, there would be one steel plate in Section 1, two in Section 2, three in Section 3, and four in Section 4 in Lane I(A). Figure 3.11(b) illustrates the steel plate layout in Lane I(B) to V: one steel plate would be placed in each section. Field cores would be extracted over these plates to calibrate and evaluate the specific gravity prediction models after several GPR measurements were taken.

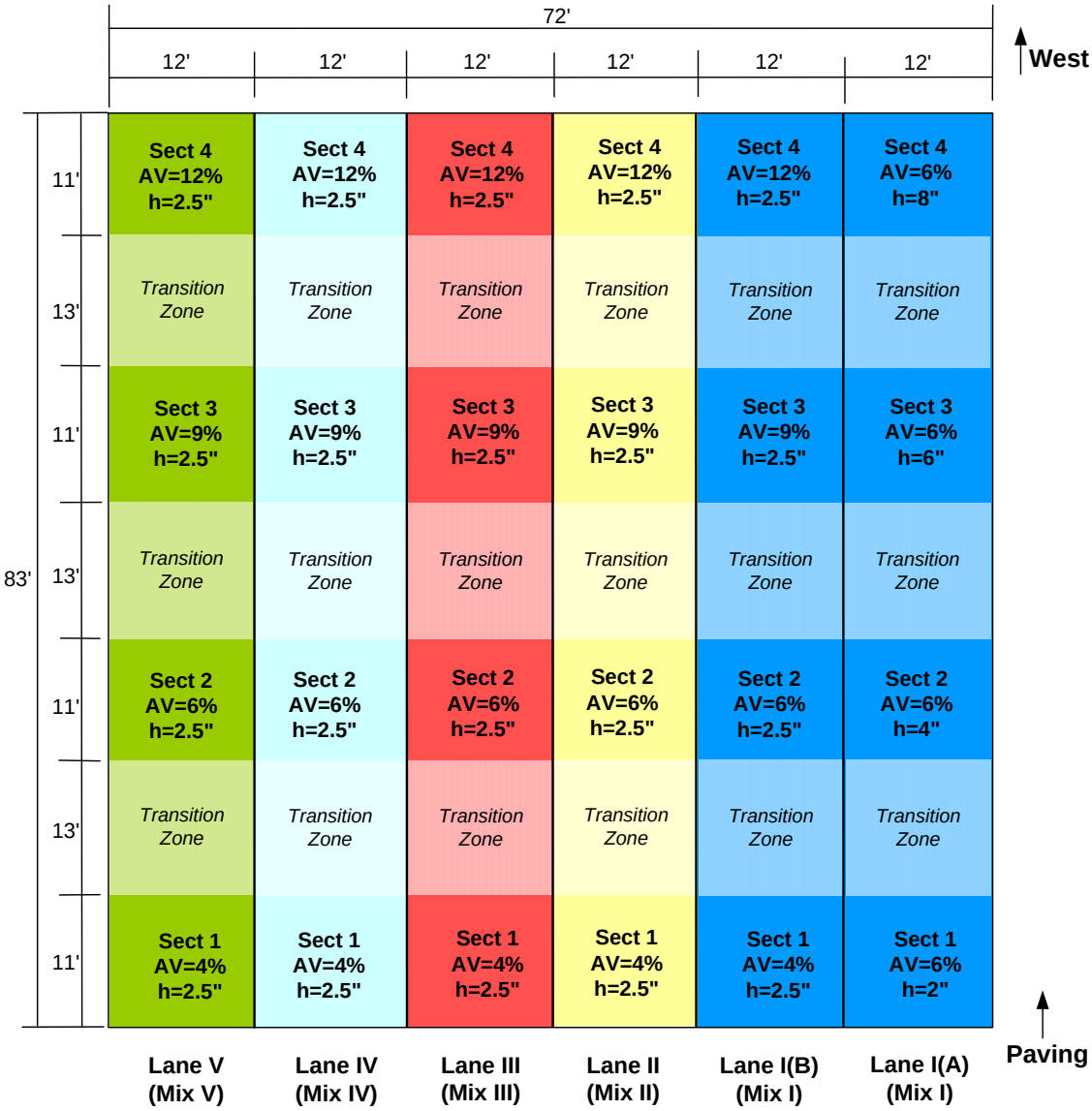

**AV: Air Void; h: Thickness of Asphalt Overlay*

Figure 3.9 Asphalt overlay construction layout.

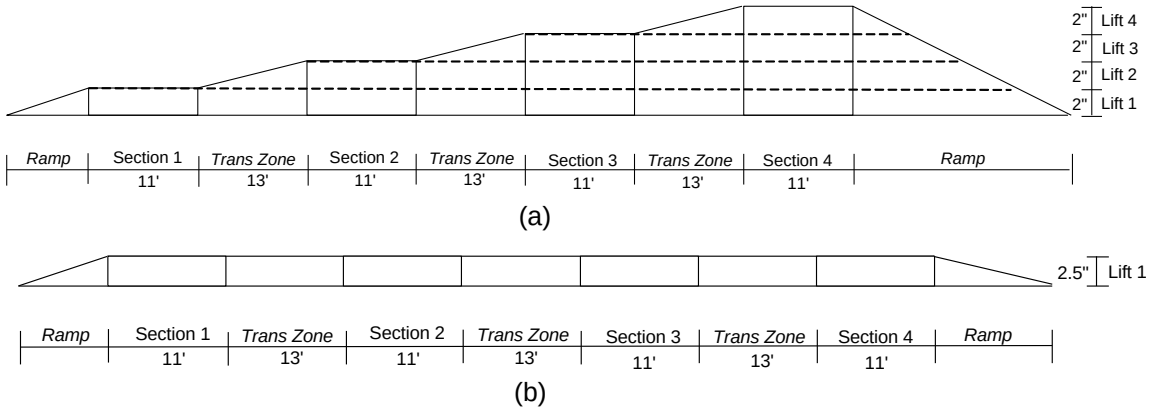

Figure 3.10 Surface layer longitudinal cross section of: (a) Lane I(A); (b) Lanes I(B) to V.

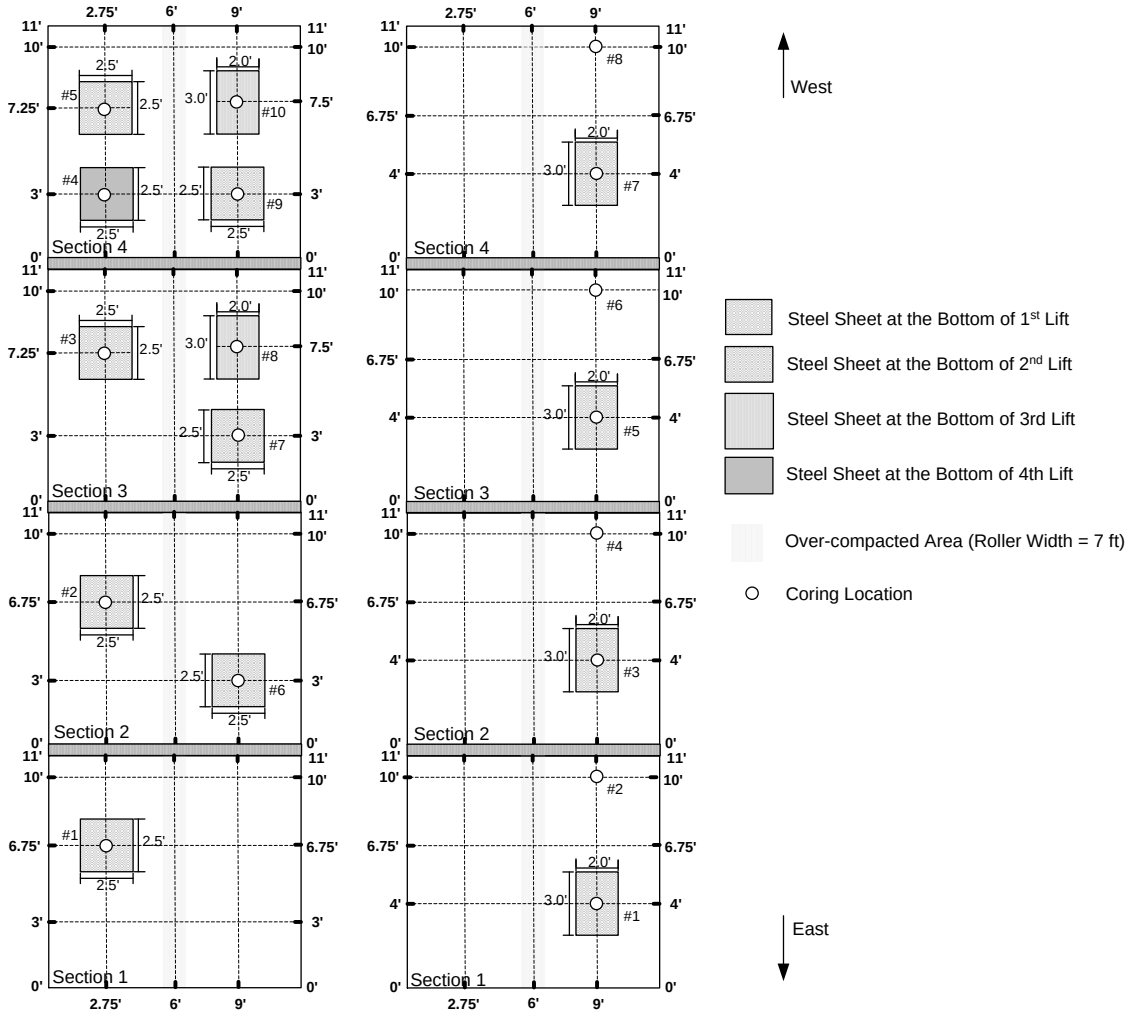

Figure 3.11 Steel plate locations in: (a) Lane I(A); (b) Lanes I(B) to V.

3.2.2 Test Site Construction

3.2.2.1 Construction process

Due to the time constraint of construction, it was planned in advance that the asphalt overlay construction of the test site would be completed on two separate days. On the first day, Lanes I(B) to V and the first lift of Lane I(A) would be constructed. On the second day, the remaining lifts of Lane I(A) would be constructed.

As Figure 3.12 exhibits, the following surface preparations were completed before the overlay construction: surface cleaning with an air blow, surface marking using paint, steel-plate fixing using nails, and tack coat application. For the tack coat application, the asphalt emulsion SS-1hp, with a specific gravity of 1.012 and an asphalt residue rate of 66%, was used. The tack coat application rate was 0.32 L/m^2 (0.07 gal/yd^2), which corresponds to a residual asphalt rate of 0.10 L/m^2 (0.023 gal/yd^2). A picture of the pavement surface after tack coat application is shown in Figure 3.13.

(a) Surface cleaning with an air blower.

(b) Surface marking using paint.

(c) Fixing the steel plate using nails.

(d) Tack coat application on the existing surface.

Figure 3.12 Surface preparation before overlay construction.

Figure 3.13 Existing pavement surface after tack coat application.

According to the mix designs and lane dimensions, the quantity of the mix needed for each test lane was estimated in advance. Based on the calculation shown in Appendix B and taking into account some safety factors, 21 tons of asphalt mixture were produced for each lane.

The asphalt overlay construction started with the first lift of Lane I(A) (Figure 3.14). The material transfer vehicle (MTV) as shown in Figure 3.15 was used to ensure the uniformity and avoid any segregation of the asphalt mixture. For each lane, samples were collected from the MTV at the beginning and end of the paving, as well as from the paver in the middle of the paving process (Figure 3.16). Mix temperature during the paving was continuously monitored using a temperature measuring gun and a temperature probe (Figure 3.17).

Figure 3.14 Paving the first lane.

Figure 3.15 Material transfer vehicle (MTV).

Figure 3.16 Sample collection from the paver.

Figure 3.17 Mix temperature check using a temperature probe.

The Caterpillar CB534D steel-drum compactor, as shown in Figure 3.18, was used for compaction. The width of the steel drums is 2.00 m (79 in), and the distance between the front and rear drums is 3.71 m (146 in). The compaction was performed along the longitudinal direction of the lane (east-west direction). Since each lane is 3.63 m (12 ft) wide, the compactor needed two passes to cover the whole lane width, and a 0.33-m-wide (1-ft-wide) area in the middle of each section was over-compacted. The compaction energy was controlled by compacting in either static or vibrating mode. The compaction speed was 42 m/min (140 ft/min) in static mode and 54 m/min (180 ft/min) in vibrating mode. The vibration frequency of the drum was 3300 vibrations/min. The in-situ density of the asphalt surface was monitored continuously using a nuclear gauge (Figure 3.19) until the target air void content was achieved in each section.

Figure 3.18 Pavement compaction.

Figure 3.19 Density measurement using a nuclear gauge.

After the paving of the first lift of Lane I(A) was completed, the construction continued in the following order: Lane I(B), Lane II, Lane III, Lane IV, and Lave V. The construction procedure of Lanes I(B) to V was a little different than that of Lane I(A), because each of these lanes contained sections with different target densities, in turn requiring different compaction efforts. To achieve different densities in different sections, each section was subjected to different numbers of compaction passes, and the density of each section was monitored continuously using nuclear gauges until the measured air void content was close to the target value. In addition, the vibration of the compactor was

turned on or off depending on the energy required to reach the target density. The compaction always started or ended at the transition zone to ensure uniform density in the test sections.

The construction of Lanes I(B) to V and Lane I(A) was completed within the same day. After construction, access to the site was denied to all but research personnel. Figure 3.20 depicts the test site after the first-day construction.

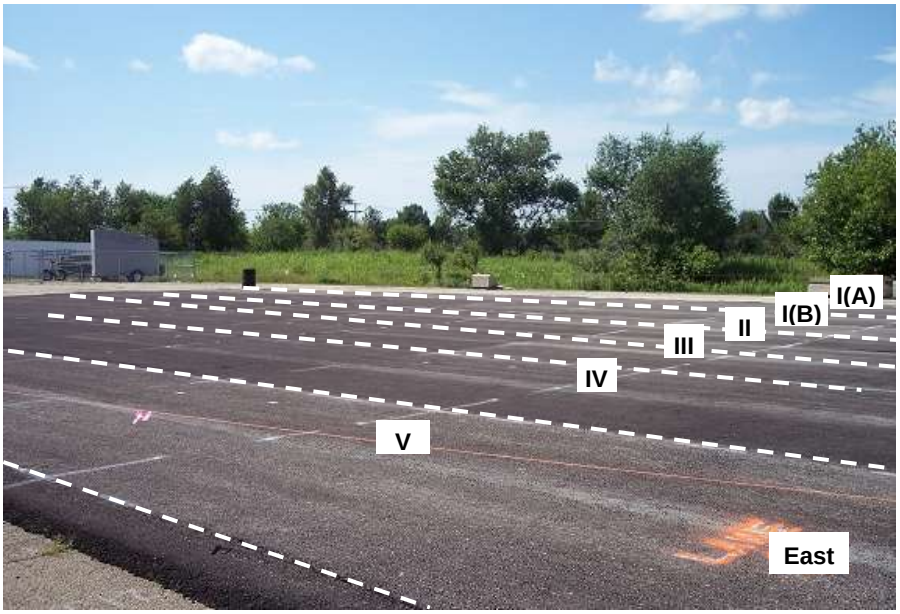

Figure 3.20 Overview of test site after the first-day construction.

In the second construction day, the remaining three lifts of Lane I(A) were paved. The second lift was placed over Sections 2, 3, and 4; the third lift covered Sections 3 and 4; and the final lift was for Section 4 only. As a result, the final thicknesses of Sections 1, 2, 3, and 4 of Lane I(A) were approximately 5 cm, 10 cm, 15 cm and 20 cm (2 in, 4 in, 6 in and 8 in), respectively. For each lift, nuclear gauge tests were conducted to control the air void content. Figure 3.21 depicts Lane I(A) containing four sections with different thicknesses after the second-day construction.

Figure 3.21 Lane I(A) after the second-day construction.

3.2.2.2 Construction quality control measurements

To ensure that the desired pavement conditions could be achieved after construction, variables such as mixture temperature, mixture density, and layer thickness were continuously monitored throughout the construction process.

Mixture temperature measurements were collected both at the mat surface (with a temperature gun) and within the mat (with a temperature probe). The first measurement was collected when the material was transferred into the paver from the MTV using a temperature probe. Subsequent measurements were collected with a temperature gun on the surface of the pavement and with a temperature probe measurements within the asphalt overlay. An 8-17 °C (15-30 °F) temperature increase was observed with the probe measurements collected within the asphalt mixture. The mixture temperatures during the paving and compaction for each lane are presented in Appendix C.

Air void content was obviously the most important mixture property to monitor for the test site construction. The different air void contents of each section were achieved through applying different numbers of compaction passes and choosing different compaction modes (static and vibration). Two nuclear gauges were used to measure the

air void content, one at the north side of the lane and the other at the south side. Data were not collected at the center of each lane because a 0.3-m (1-ft) wide over-compacted area existed in the center, and no data from this area would be used for density model evaluation. The average air void contents of each section measured by the nuclear gauge after construction are presented in Tables 3.4 and 3.5. It is evident that for most sections, the final air void contents measured by the nuclear gauge are reasonably close to the target values. It is worth noting, though, that the air void contents shown in Tables 3.4 and 3.5 are from the nuclear gauge measurements and not necessary equal to the real values.

Table 3.4 Final Air Void Content Measured by Nuclear Gauge: Lanes I(B) to V

Section #			1	2	3	4
Lane I(B)	Compaction Level (%)	South	95.0	94.4	90.5	89.7
		North	97.5	95.1	91.6	88.5
		Average	96.3	94.8	91.1	89.1
	Air void (%)		3.8	5.3	9.0	10.9
Lane II	Compaction Level (%)	South	93.4	93.2	90.2	89.3
		North	95.1	94.8	93.2	89.7
		Average	94.3	94.0	91.7	89.5
	Air void Content (%)		5.8	6.0	8.3	10.5
Lane III	Compaction Level (%)	South	94.9	93.4	91.0	87.9
		North	95.1	93.1	91.0	87.2
		Average	95.0	93.3	91.0	87.6
	Air void Content (%)		5.0	6.8	9.0	12.5
Lane IV	Compaction Level (%)	South	96.5	94.4	92.4	90.2
		North	96.4	94.0	93.8	89.2
		Average	96.5	94.2	93.1	89.7
	Air void Content (%)		3.6	5.8	6.9	10.3
Lane V	Compaction Level (%)	South	96.7	95.2	93.2	88.9
		North	95.5	94.0	91.3	88.0
		Average	96.1	94.6	92.3	88.5
	Air void Content (%)		3.9	5.4	7.8	11.6

Table 3.5 Final Air Void Content Measured by Nuclear Gauge: Lane I(A)

Lift #			1	2	3	4
Section 1	Compaction Level (%)	South	-	-	-	-
		North	-	-	-	-
		Average	-	-	-	-
	Air Void Content (%)		-	-	-	-
Section 2	Compaction Level (%)	South	93.9	94.6	-	-
		North	93.8	94.5	-	-
		Average	93.9	94.6	-	-
	Air Void Content (%)		6.1	5.4	-	-
Section 3	Compaction Level (%)	South	93.5	94.3	94.0	-
		North	94.5	94.4	95.4	-
		Average	94.0	94.4	94.7	-
	Air Void Content (%)		6.0	5.6	5.3	-
Section 4	Compaction Level (%)	South	94.5	93.7	94.5	94.3
		North	92.9	94.8	94.3	95.0
		Average	93.7	94.0	94.4	94.7
	Air Void Content (%)		6.3	6.0	5.6	5.3
Average Air Void Content (%)			6.1	5.7	5.5	5.3

In Lanes I(B) to V, sections with different air voids required different amounts of mix to achieve the same layer thickness. Therefore, the amount of material needed for a final depth of 6.3 cm (2.5 in) was estimated and used for each section. The final thickness of each section was checked at the edge of each lane (Figure 3.22). The measured thickness of each section after construction is shown in Table 3.6. For Lane I(B) to Lane V, the final thicknesses of the 9% and 12% sections are close to the target thickness of 6.3 cm (2.5 in), while the final thicknesses of the 4% and 6% sections are lower. This could be related to the existing surface and/or the adjusted clearance of the screed during the paving process

to achieve the needed air void content. Considering that the main purpose of building different sections in Lanes I(B) to V is to evaluate the effect of air void content, these thickness differences are considered acceptable.

Figure 3.22 Final thickness check of asphalt layer after compaction.

Table 3.6 Final Layer Thicknesses Measured at the South Edge after Compaction (in)

Lane / Section	Lane I(A)	Lane I(B)	Lane II	Lane III	Lane IV	Lane V
1	2.0	2.2	1.8	1.9	2.0	2.0
2	4.1	2.2	1.8	2.0	2.1	2.1
3	6.3	2.4	2.3	2.5	2.5	2.3
4	8.5	2.2	2.3	2.5	2.5	2.4

3.2.3 Data Analysis and Model Evaluation

After the test site was constructed, a 2 GHz air-coupled van-mounted GPR system, as shown in Figure 3.23, was used for GPR data collection. Both stationary data and survey data were collected. Stationary data were collected over the steel plate locations in each section. Survey data were collected for each lane along the central line of the steel plates. During the GPR surveys, a distance-measuring instrument (DMI) was attached to the van wheel to synchronize the GPR data with the survey distance. The survey speed

was approximately 32 km/h (20 mph), and the data were collected at a rate of 1 scan per 25.4 mm (1 scan per in).

Figure 3.23 2-GHz air-coupled GPR system.

Figure 3.24 shows a typical A-scan (single scan) image of the GPR data over the steel plate and a typical B-scan (multiple stacked scans shown against survey distance) image of the GPR survey data of Lanes I(B) to V. The locations of the asphalt overlay surface and bottom are labeled in the figure. Note that in Figure 3.24(b), the GPR signal reflection amplitudes were represented by different grey scales: the larger the reflection amplitude, the brighter the color. The plateau shapes derive from the strong reflections of the GPR signals from the steel plates underneath the asphalt overlay, which indicate the accurate locations of the bottom of the asphalt overlay.

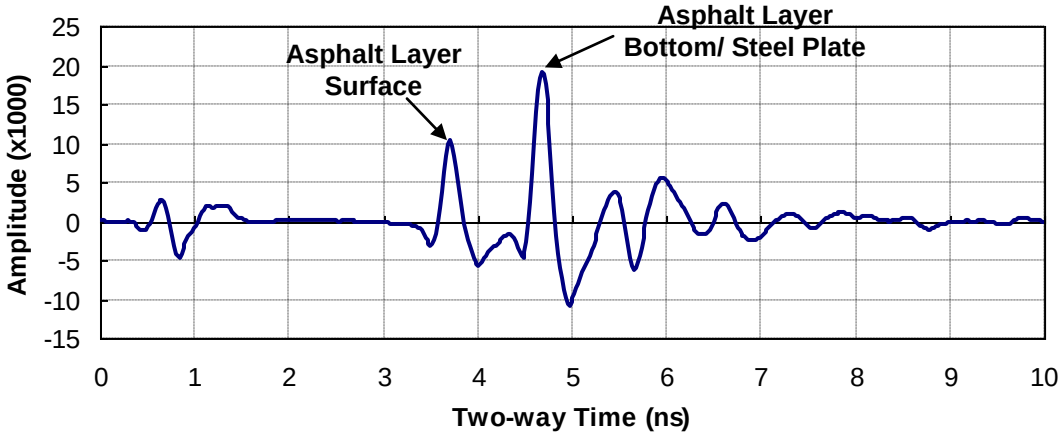

(a) A-scan image of GPR data over steel plate.

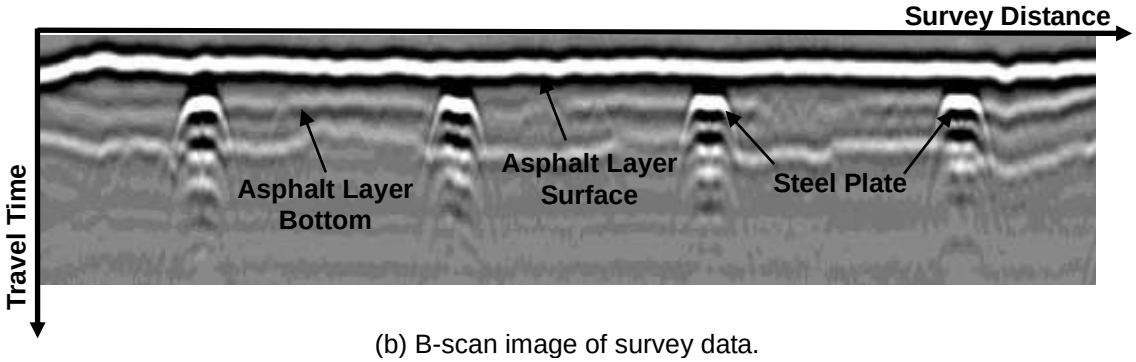

(b) B-scan image of survey data.

Figure 3.24 Typical GPR images.

Based on the amplitudes of the GPR wave surface reflections, the dielectric constant profile of each test lane was obtained using Equation 2.27. As Figure 3.25 shows, the dielectric constant profile of each lane exhibited a decreasing trend along the survey direction, from the high-density section to the low-density section. Such a trend verifies the positive relationship between the dielectric constant and density, i.e., the dielectric constant of a mixture increases when its density increases. In addition, the lanes composed of limestone mixes (Lane I(B) and Lane V) exhibited a larger dielectric constant than the lanes with granite mixes, an expected result because the limestone aggregate has a greater dielectric constant than the granite aggregate.

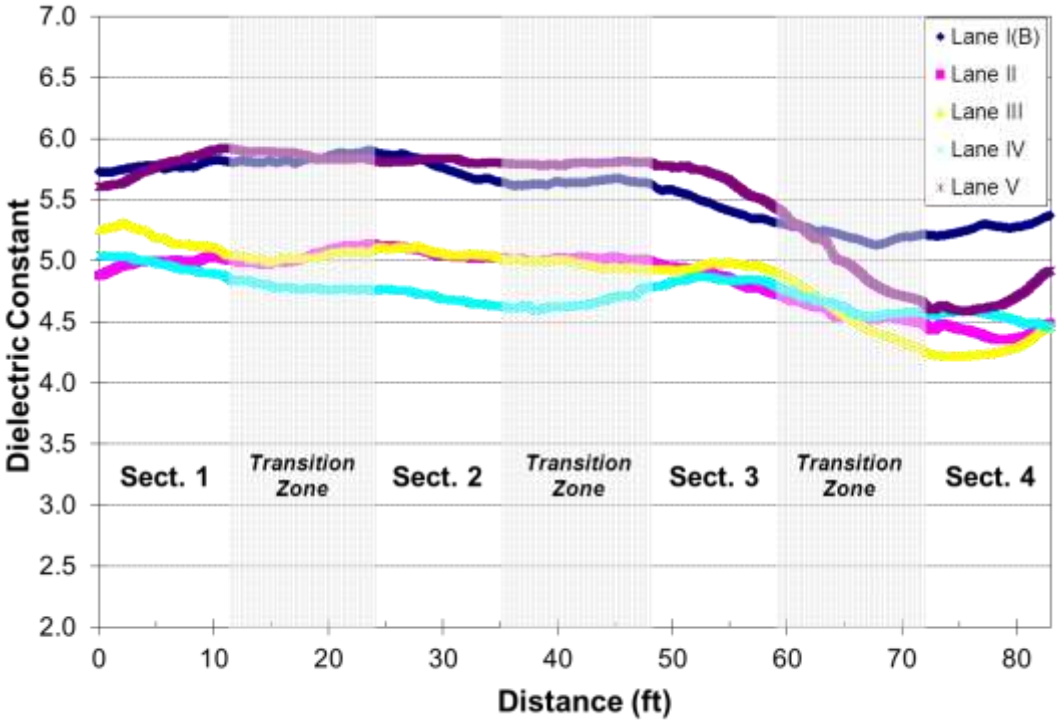

Figure 3.25 Asphaltic mixture dielectric constant profile of each test lane.

The obtained dielectric constant profiles as shown in Figure 3.25 can then be plugged into the two developed specific gravity models (Equations 3.6 and 3.9) to predict the pavement density profiles. Recall that there are six parameters in these specific gravity models: P_b, G_{se}, G_{mm}, G_b, ε_b, and ε_s. As Table 3.7 shows, the values of parameters P_b, G_{se} and G_{mm}, were obtained from the mixture designs, and the values of parameters G_b, and ε_b are usually constant around 1.015 and 3, respectively. The values of ε_s depend on the aggregate type and source. Without any laboratory testing or historic data, it is relatively difficult to determine the exact value of ε_s for a specific mixture.

To obtain the accurate dielectric constants of the aggregates for the model evaluation purpose, one core was extracted from Section 1 of each lane of Lane I(B) to Lane V (core #1 in Figure 3.11b), and its lab-measured bulk specific gravity and GPR-measured dielectric constant were utilized to back-calculate the value of ε_s. Table 3.7 shows the back-calculated values of ε_s for each mix when two different models were used. It can be noticed that the ε_s values of cores II-1, III-1 and IV-1 (granite mixes) are relatively

close to each other, but are smaller than those of cores I(B)-1 and V-1 (limestone mixes).

Table 3.7 Back-calculated Aggregate Dielectric Constants of Each Mix

Core #	ε_{AC}	Parameters with Known Values						Back-calculated ε_s	
		G_{mb}	P_b (%)	G_b	G_{se}	G_{mm}	ε_b	Modified CRIM	Modified Bottcher
I(B)-1*	5.77	2.288	6.0	1.015	2.661	2.481	3	6.69	6.94
II-1	4.99	2.362	5.4	1.015	2.682	2.528	3	5.48	5.73
III-1	5.25	2.364	5.4	1.015	2.682	2.501	3	5.86	6.01
IV-1	5.00	2.371	6.4	1.015	2.679	2.468	3	5.47	5.65
V-1	5.73	2.359	5.1	1.015	2.668	2.505	3	6.44	6.62

* *I(B)-1 represents the #1 core in Lane I(B), and the same rule applies to the other core #'s.*

After the values of ε_s were determined, the two models were applied to predict the G_{mb} profiles of each test lane. To evaluate the prediction accuracies of the two models, additional seven cores were extracted from each lane (cores #2 to #8 in Figure 3.11b). The G_{mb} values of these cores were measured in the lab and compared with the predicted values from the GPR measurements. To optimize the accuracy of laboratory G_{mb} testing, both the saturated surface dry (SSD) method (Figure 3.26a) and Corelok automatic vacuum sealing method (Figure 3.26b) were used (AASHTO T166-07 and AASHTO T331-07). The SSD method is the most commonly used method for measuring the G_{mb} of specimens with air void content less than 10%. Thus, it was used to test the cores from Sections 1, 2 and 3, which have target air void contents of less than 10%. The Corelok method is more accurate in measuring the G_{mb} of large-void specimens. Hence, it was employed to measure the G_{mb} of the cores from Section 4, which have a target air void content of 12%. Note that an air void content of 12% is not likely to appear for the dense-graded asphalt mixture in the field. This large air-void content was considered in the test site design because it could provide a wider data range for the model evaluation.

(a) (b)

Figure 3.26 Laboratory measurement of Gmb: (a) SSD method; (b) Corelok method.

Table 3.8 to Table 3.12 present the prediction errors of the two models for the cores extracted from Lane I(A) to Lane V, respectively. As these tables indicate, the average prediction errors of the modified CRIM for the five mixes are within the range of 1.7% to 4.0%, and those of the modified Bottcher model for the five mixes are within the range of 1.6% to 3.9%. The average prediction errors for all the 35 cores are 2.7% and 2.5% for the modified CRIM and modified Bottcher model, respectively. This indicates that both methods provided reasonably accurate density prediction, although the modified Bottcher model performed a little better than the modified CRIM in terms of the average prediction error.

Table 3.8 Gmb Prediction Errors of Each Model for Mix I (Lane I(B))

Core #	Section #	Core G_{mb}	Core Air Void (%)	ε_{AC}	Modified CRIM		Modified Bottcher	
					G_{mb}	Error* (%)	G_{mb}	Error (%)
I(B)-2	1	2.314	6.7	5.78	2.291	1.0	2.291	1.0
I(B)-3	2	2.309	6.9	5.77	2.288	0.9	2.288	0.9
I(B)-4		2.286	7.9	5.66	2.250	1.5	2.251	1.5
I(B)-5	3	2.216	11.0	5.49	2.192	1.1	2.194	1.0
I(B)-6		2.211	12.4	5.35	2.143	3.1	2.146	2.9
I(B)-7	4	2.188	15.2	5.28	2.118	3.2	2.123	3.0
I(B)-8		2.177	13.6	5.37	2.150	1.3	2.153	1.1
Average Prediction Error (%)					1.7		1.6	

* *Error is calculated by dividing the absolute difference between the predicted G_{mb} and core G_{mb} by the core G_{mb}.*

Table 3.9 Gmb Prediction Errors of Each Model for Mix II (Lane II)

Core #	Section #	Core G_{mb}	Core Air Void (%)	ε_{AC}	Modified CRIM		Modified Bottcher	
					G_{mb}	Error* (%)	G_{mb}	Error (%)
II-2	1	2.358	6.7	5.01	2.371	0.5	2.370	0.5
II-3	2	2.358	6.7	5.08	2.400	1.8	2.400	1.8
II-4		2.349	7.1	5.02	2.375	1.1	2.375	1.1
II-5	3	2.300	9.0	4.91	2.328	1.2	2.328	1.2
II-6		2.294	9.2	4.77	2.267	1.2	2.268	1.1
II-7	4	2.211	13.7	4.40	2.101	5.0	2.109	4.6
II-8		2.200	13.0	4.41	2.106	4.3	2.113	4.0
Average Prediction Error (%)					2.2		2.0	

* *Error is calculated by dividing the absolute difference between the predicted G_{mb} and core G_{mb} by the core G_{mb}.*

Table 3.10 Gmb Prediction Errors of Each Model for Mix III (Lane III)

Core #	Section #	Core G_{mb}	Core Air Void (%)	ε_{AC}	Modified CRIM		Modified Bottcher	
					G_{mb}	Error* (%)	G_{mb}	Error (%)
III-2	1	2.353	5.9	5.12	2.312	1.8	2.316	1.6
III-3	2	2.318	7.3	5.11	2.308	0.4	2.312	0.3
III-4		2.297	8.2	5.05	2.283	0.6	2.288	0.4
III-5	3	2.269	9.3	4.95	2.242	1.2	2.248	0.9
III-6		2.259	9.7	4.96	2.246	0.6	2.252	0.3
III-7	4	2.199	13.1	4.23	1.935	12.0	1.954	11.1
III-8		2.168	13.3	4.37	1.996	7.9	2.012	7.2
Average Prediction Error (%)					3.5		3.1	

* *Error is calculated by dividing the absolute difference between the predicted G_{mb} and core G_{mb} by the core G_{mb}.*

Table 3.11 Gmb Prediction Errors of Each Model for Mix IV (Lane IV)

Core #	Section #	Core G_{mb}	Core Air Void (%)	ε_{AC}	Modified CRIM		Modified Bottcher	
					G_{mb}	Error* (%)	G_{mb}	Error (%)
IV-2	1	2.327	5.7	4.91	2.332	0.2	2.333	0.2
IV-3	2	2.320	5.8	4.72	2.249	3.1	2.251	3.0
IV-4		2.251	8.8	4.64	2.214	1.7	2.216	1.6
IV-5	3	2.269	8.1	4.87	2.315	2.0	2.315	2.0
IV-6		2.247	9.0	4.84	2.302	2.5	2.303	2.4
IV-7	4	2.218	10.6	4.59	2.191	1.2	2.195	1.1
IV-8		2.204	12.1	4.49	2.146	2.6	2.151	2.4
Average Prediction Error (%)					1.9		1.8	

* *Error is calculated by dividing the absolute difference between the predicted G_{mb} and core G_{mb} by the core G_{mb}.*

Table 3.12 Gmb Prediction Errors of Each Model for Mix V (Lane V)

Core #	Section #	Core G_{mb}	Core Air Void (%)	ε_{AC}	Modified CRIM		Modified Bottcher	
					G_{mb}	Error* (%)	G_{mb}	Error (%)
V-2	1	2.333	6.9	5.87	2.408	3.2	2.408	3.3
V-3	2	2.328	7.1	5.83	2.394	2.8	2.394	2.9
V-4		2.308	7.9	5.79	2.380	3.1	2.380	3.2
V-5	3	2.302	8.1	5.74	2.363	2.6	2.363	2.7
V-6		2.270	9.4	5.51	2.280	0.5	2.281	0.5
V-7	4	2.151	13.5	4.60	1.938	9.9	1.953	9.2
V-8		2.153	11.4	4.82	2.023	6.0	2.034	5.5
Average Prediction Error (%)					4.0		3.9	

* *Error is calculated by dividing the absolute difference between the predicted G_{mb} and core G_{mb} by the core G_{mb}.*

3.2.4 Model Fine-tuning

The test site data has shown that both specific gravity models predicted asphalt mixture's density with reasonable accuracy in terms of average prediction error. However, the results in Tables 3.8 to 3.12 also indicated that when the cores in Section 1 were used for back-calculating ε_s, the prediction errors in Section 4 are generally larger than those in Sections 1 to 3. For example, the prediction errors of core III-7 are 12.0% and 11.1% for the modified CRIM and modified Bottcher model, respectively, although the average prediction errors of Lane III cores are 3.5% and 3.1% for the two models, respectively. However, it should be noted that the relative large errors in Section 4 are not caused by changing the laboratory G_{mb} testing method from SSD to Corelok. In fact, if the SSD method is used to test Section 4 cores, the prediction errors in Section 4 will be even larger, because the SSD method predicts higher G_{mb} than the Corelok method for large-void specimens (Leng et al. 2011). This implies that the models themselves might be the main reason for the large prediction errors in Section 4. Therefore, model fine-tuning was conducted to further improve the performance of the specific gravity models.

Among the two candidate models, the modified Bottcher model has exhibited better performance for the test site data. However, it has to be noted that the Bottcher model is based on the assumption that all inclusions in the mixture are spherical. Although the aggregates and air voids in asphalt mixture can be considered to have shapes close to sphere, they are not exactly spherical. As a result, errors may be caused by this assumption.

According to Behari (2005), if the mixture inclusions are not spherical, but of any arbitrary shape, the Bottcher model (Equation 2.42) can be modified to the following equation by introducing a shape factor, *u*:

$$\frac{\varepsilon_{eff} - \varepsilon_0}{\varepsilon_{eff} + u\varepsilon_0 + 2(\varepsilon_{eff} - \varepsilon_0)} = \sum_{i=1}^{N} V_i \frac{\varepsilon_i - \varepsilon_0}{\varepsilon_i + u\varepsilon_0 + 2(\varepsilon_{eff} - \varepsilon_0)}. \tag{3.14}$$

The value of *u* will vary depending on the shape of the scatterers and is equal to 2 for spherical inclusions. It can be noticed that when the shape factor is equal to 2, Equation 3.14 becomes the Bottcher model.

By following the same procedure as presented in Section 3.1.2, the following specific gravity model can be derived from Equation 3.14:

$$G_{mb} = \frac{\dfrac{\varepsilon_{AC} - \varepsilon_b}{3\varepsilon_{AC} + (u-2)\varepsilon_b} - \dfrac{1-\varepsilon_b}{1 + (u-2)\varepsilon_b + 2\varepsilon_{AC}}}{\left(\dfrac{\varepsilon_s - \varepsilon_b}{\varepsilon_s + (u-2)\varepsilon_b + 2\varepsilon_{AC}}\right)\left(\dfrac{1-P_b}{G_{se}}\right) - \left(\dfrac{1-\varepsilon_b}{1 + (u-2)\varepsilon_b + 2\varepsilon_{AC}}\right)\left(\dfrac{1}{G_{mm}}\right)}, \tag{3.15}$$

where *u* is the shape factor, and all the other parameters are as defined in Figure 3.3. Obviously, the modified Bottcher model (Equation 3.9) is a special case of Equation 3.15 when *u* is equal to 2.

Since the asphalt mixture contains non-spherical aggregate and air inclusions, a shape factor other than 2 should be used. To find the correct shape factor value for each asphalt mixture evaluated in the test site, nonlinear least square curve fitting using Equation 3.15 was performed on the G_{mb}-ε_{AC} data of the eight cores extracted from each test lane. The shape factor, *u*, and the dielectric constant of aggregate, ε_s, were determined from the curve fitting. The values of all other parameters in Equation 3.15 for

each mixture are presented in Table 3.7. Table 3.13 shows the optimum values of *u* and ε_s for each mix which provide the least sum of square error (SSE) for the curve fitting. It can be seen that the optimum *u* values for the five mixes are within a relatively small range, which is between -0.5 and 0.0.

Table 3.13 Optimum Shape Factor Values for Each Mix

Mix #	Mix I	Mix II	Mix III	Mix IV	Mix V
Shape Factor	0.0	-0.1	-0.3	-0.1	-0.5
Aggregate Dielectric Constant	7.2	6.0	6.4	5.9	7.3

Since the optimum *u* values for each mix are relatively close to each other, it is reasonable to seek for an optimum *u* value which generally applies to different mixes. As Table 3.14 shows, the individual curve fitting SSE's for each mixt at different *u* values were first calculated, and then the sum of SSE for the five mixes at each *u* value was computed. The u value which provided the minimum sum of SSE would be selected as the optimum *u* value. Figure 3.27 illustrates the relationship between the sum of SSE and the shape factor for the five mixes. It can be seen that a *u* value of -0.3 provides the minimum sum of SSE, i.e., the best curve fitting, for the five mixes.

When *u* equals to -0.3, Equation 3.15 becomes:

$$G_{mb} = \frac{\dfrac{\varepsilon_{AC} - \varepsilon_b}{3\varepsilon_{AC} - 2.3\varepsilon_b} - \dfrac{1-\varepsilon_b}{1-2.3\varepsilon_b + 2\varepsilon_{AC}}}{\left(\dfrac{\varepsilon_s - \varepsilon_b}{\varepsilon_s - 2.3\varepsilon_b + 2\varepsilon_{AC}}\right)\left(\dfrac{1-P_b}{G_{sb}}\right) - \left(\dfrac{1-\varepsilon_b}{1-2.3\varepsilon_b + 2\varepsilon_{AC}}\right)\left(\dfrac{1}{G_{mm}}\right)}. \qquad (3.16)$$

In this study, the above equation is referred to as the Al-Qadi Lahouar Leng (ALL) model.

Figures 3.28 to 3.32 illustrate the comparisons of the fitting curves by using three different models (the modified CRIM, the modified Bottcher model, and the ALL model) for Mixes I to V, respectively. These figures clearly show that the ALL model provided the best fitting to the core data for all mixes. Table 3.15 presents the SSE of the three models for the five mixtures. It is evident that the ALL model produces significant smaller SSE values compared to the other two models for each mixture. Therefore, the ALL model is selected

as the best-performance model based on the test site data, and its performance would be further verified using in-service pavement data.

Table 3.14 Nonlinear Fitting SSE of Each Model

Shape Factor	SSE for Each Mix					Sum of SSE
	Mix I	Mix II	Mix III	Mix IV	Mix V	
-1.0	0.0100	0.0646	0.0845	0.0295	0.0308	0.2194
-0.9	0.0077	0.0414	0.0495	0.0216	0.0178	0.138
-0.8	0.0059	0.0267	0.0282	0.0167	0.0099	0.0874
-0.7	0.0046	0.0172	0.0155	0.0135	0.0054	0.0562
-0.6	0.0037	0.0110	0.0081	0.0114	0.0033	0.0375
-0.5	0.0030	0.0069	0.0042	0.0100	**0.0029**	0.027
-0.4	0.0024	0.0043	0.0026	0.0091	0.0037	0.0221
-0.3	0.0021	0.0026	**0.0025**	0.0086	0.0053	**0.0211**
-0.2	0.0018	0.0017	0.0034	0.0083	0.0076	0.0228
-0.1	0.0017	**0.0013**	0.0050	**0.0081**	0.0103	0.0264
0	**0.0016**	0.0013	0.0071	0.0081	0.0132	0.0313
0.1	0.0016	0.0015	0.0094	0.0082	0.0163	0.037
0.2	0.0016	0.0019	0.0120	0.0084	0.0196	0.0435
0.3	0.0017	0.0025	0.0146	0.0086	0.0229	0.0503
0.4	0.0018	0.0032	0.0173	0.0088	0.0263	0.0574
0.5	0.0019	0.0040	0.0201	0.0091	0.0296	0.0647

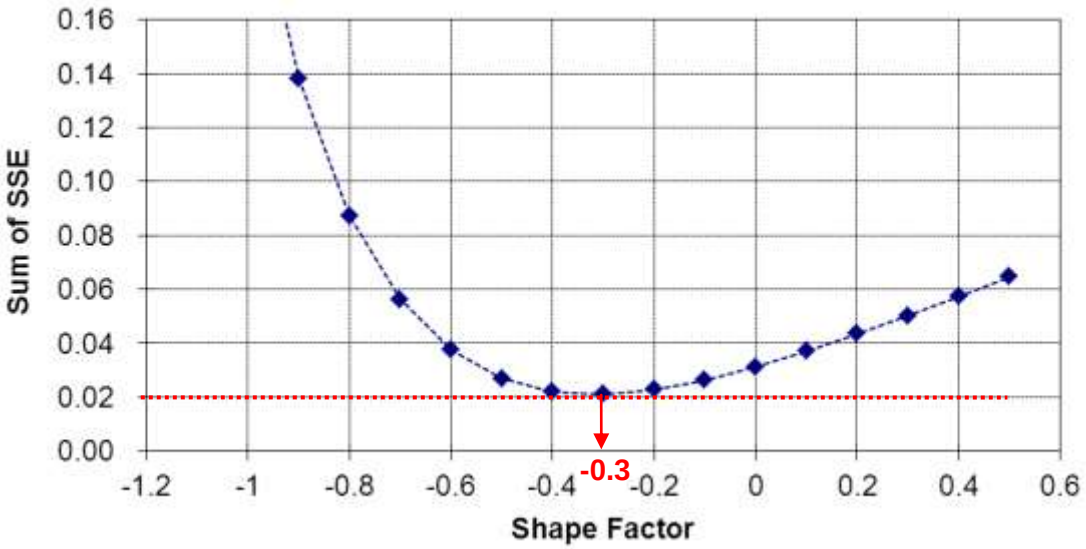

Figure 3.27 Relationship between the shape factor and sum of SSE.

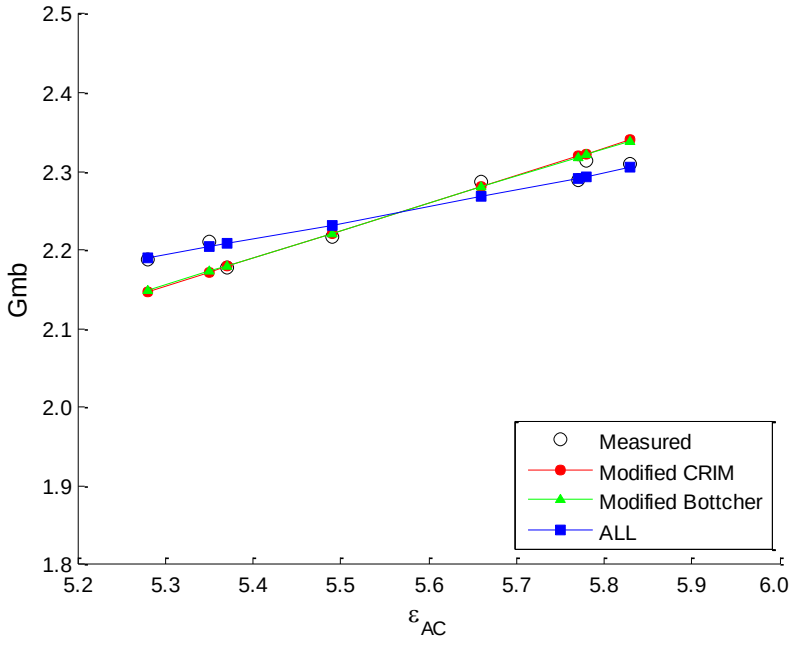

Figure 3.28 Non-linear least square curve fitting for Mix I.

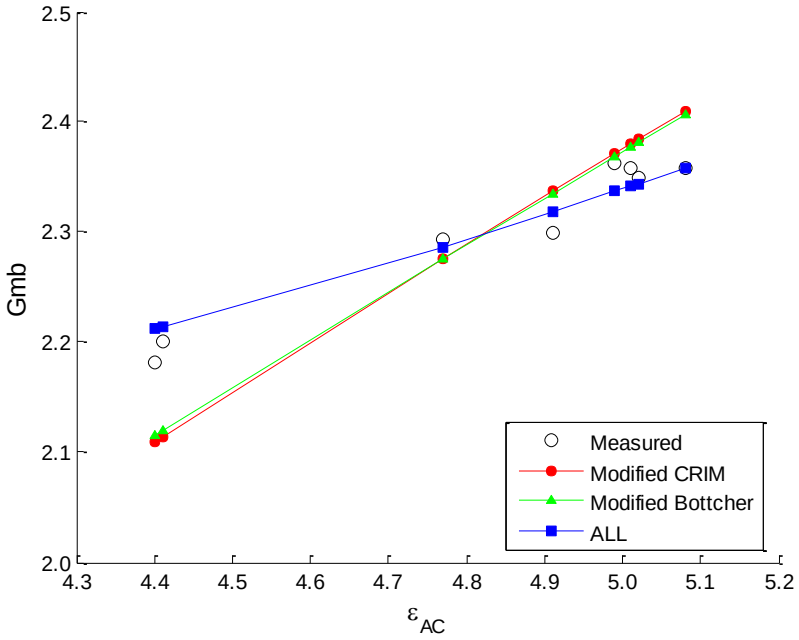

Figure 3.29 Non-linear least square curve fitting for Mix II.

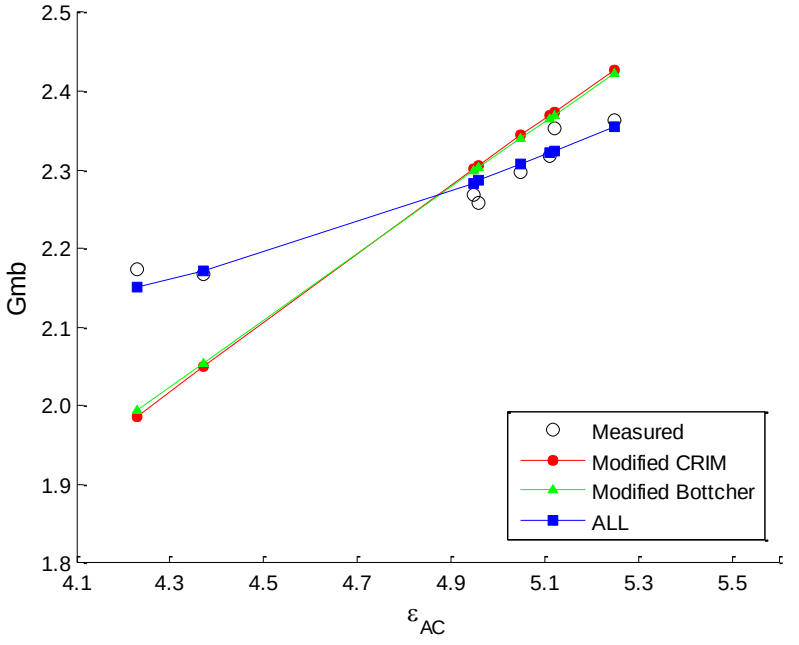

Figure 3.30 Non-linear least square curve fitting for Mix III.

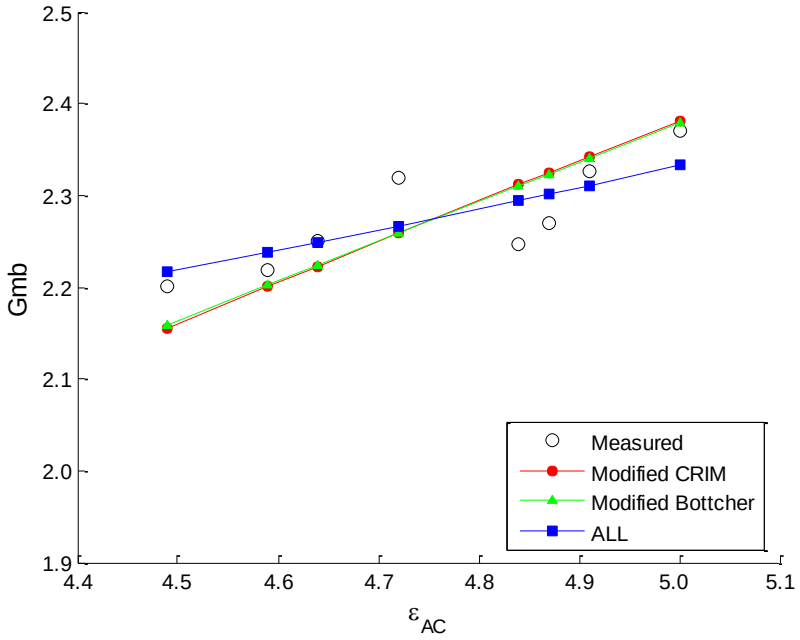

Figure 3.31 Non-linear least square curve fitting for Mix IV.

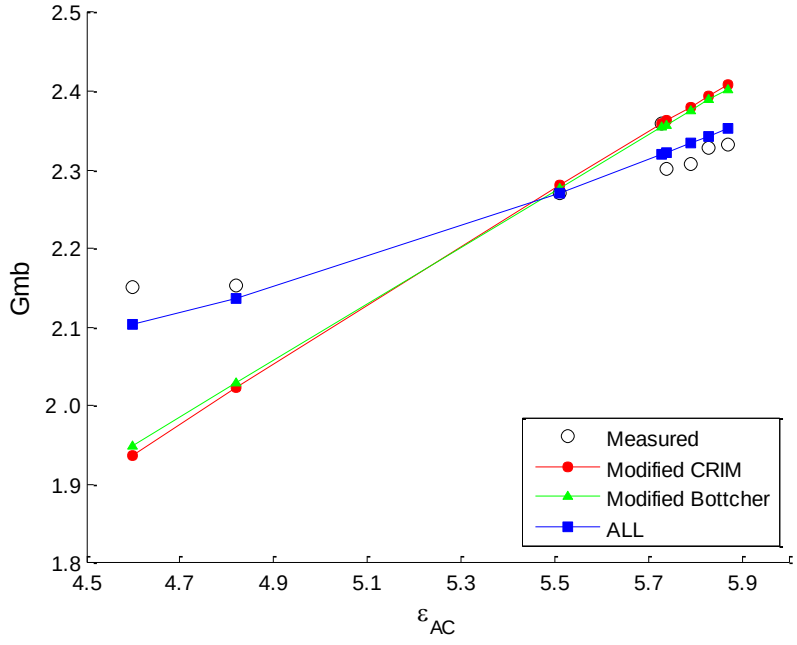

Figure 3.32 Non-linear least square curve fitting for Mix V.

Table 3.15 Comparison of SSE of Three Specific Gravity Models

Specific Gravity Model	SSE				
	Mix I	Mix II	Mix III	Mix IV	Mix V
Modified CRIM	0.0053	0.0196	0.0619	0.0633	0.1125
Modified Bottcher	0.0048	0.0173	0.0551	0.0585	0.1026
ALL Model	0.0020	0.0025	0.0025	0.0085	0.0057

3.3 Model Validation Using In-service Pavement Data

Based on the test site data, the ALL model has been identified as the best model for predicting in-situ asphalt mixture density. To further verify the performance of this model, GPR data was collected from in-service pavement sections.

3.3.1 Description of In-service Pavement Construction Site

As Figure 3.33 shows, the in-service pavement construction site, where GPR data were collected for the model validation purpose, is located on IL-72 and between the Bartlett Rd. and Glen Lake Rd. in Hoffman Estates and Barrington, IL. The total length of the construction site in each direction is 5.26 km (3.27 miles). The old pavement structure included an asphalt overlay over concrete pavements, and a 5-cm (2-in) thick new asphalt overlay was placed using six different mixtures: four newly developed mixes and two control mixes, as shown in Table 3.16. The purpose of building this construction site was to evaluate the field performance of four new mixes, which were potential next-generation overlay mix in Illinois. However, it should be noted that among the six mixtures, three of them contained steel slags, which could be a variation source to the GPR measurement. The friction mix contained 36% steel slags, the 12.5mm SMA contained 57% steel slags, and the fiber/slag mix contained 20% steel slags. The details of the aggregate types used in each mixture are presented in Appendix D.

Figure 3.33 Location of the construction site, Hoffman Estates and Barrington, IL.

Table 3.16 Summary of Construction Site Mixtures

Mixture Name		Nominal Maximum Aggregate Size (mm)	Gradation	Binder	Asphalt Content (%)
New Mixes	Quartzite Mix	9.5	Fine Dense-Graded	PG 70-22	5.8
	4.75mm SMA*	4.75	SMA	PG 70-22	7.3
	Sprinkle Mix	9.5	Fine Dense-Graded	PG 70-22	6.1
	Fiber/Slag Mix	9.5	Fine Dense-Graded	PG 70-22	5.7
Control Mixes	Friction Mix	9.5	Coarse Dense-Graded	PG 70-22	5.1
	12.5mm SMA	12.5	SMA	PG 76-22	6.0

**SMA represents Stone Mastic Asphalt*

3.3.2 In-service Pavement Data Collection

The same GPR system as used in the test site data collection (Figure 3.23) was used to collect data from the construction site. The data collection at the construction site was conducted for the following three purposes:

- to investigate the relationship between the compaction effort and the GPR measurement
- to evaluate the effect of temperature on the GPR measurement
- to validate the performance of the ALL model

During the asphalt pavement construction process, the fractional volume of air within the asphalt mixture will become smaller during the compaction process, which will result in change in the collected GPR data. To explore the relationship between the GPR measurements and the compaction effort, stationary GPR data were collected at the same spot in the construction site after each compaction pass during the asphalt overlay construction (Figure 3.34).

Figure 3.34 GPR data collection during compaction.

Because the compaction temperature of an asphalt mixture is much higher than its in-service temperature, it is necessary and important to know the effect of temperature on the GPR measurement. To quantify such effect, GPR data were collected from a selected spot in the construction site at different mixture temperatures during its cooling process after construction. The pavement surface temperature was measured using an infrared thermo-gun before each GPR test.

The data collection for the model verification purpose was conducted in the following steps, as shown in Figure 3.35:

1. Collect nuclear density measurements at pre-selected locations.
2. Collect GPR data at the same locations where the nuclear density data were collected.
3. Extract cores from the same locations where the nuclear gauge and GPR data were collected.

Figure 3.35 In-service pavement data collection: (a) nuclear gauge testing; (b) GPR data collection; (c) core extraction.

Among the six paved mixtures, GPR data were collected from five of them: namely the quartzite mix, 4.75mm SMA, sprinkle mix, fiber/slag mix, and friction mix. As Figure 3.36 illustrates, six cores were extracted for each type of mixture. These cores covered the locations of left wheel path, right wheel path, and central lane. The bulk specific gravities of the field cores were measured in the laboratory, and then compared to the nuclear-gauge-measured and the GPR-predicted densities.

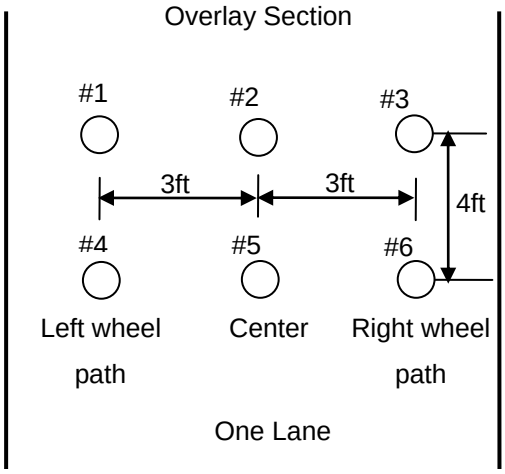

Figure 3.36 Coring locations at each test location.

3.3.3 Relationship between GPR Measurements and Number of Compactor Passes

Figure 3.37 shows the compaction curve relating the reflection amplitude of GPR signal and pass number of the compactor for two mixtures: 12.5mm SMA and 4.75mm SMA. In this figure, the reflection amplitudes of both mixtures increase during the first couple of compaction passes due to the mixture densification. When the compaction pass number reaches six, both reflection amplitudes become relatively constant, which indicates that the maximum densities have been achieved. Such compaction curves can be used to determine the compaction pass number required to achieve the maximum mixture density. The reflection amplitude corresponding to the maximum density can also be used as a reference to examine the density levels of the asphalt pavement at other locations. Note that the reflection amplitude of 12.5mm SMA in Figure 3.37 is much larger than that of 4.75mm SMA, because a large amount of steel slags were used in 12.5mm SMA, while there is no steel slag in 4.75mm SMA.

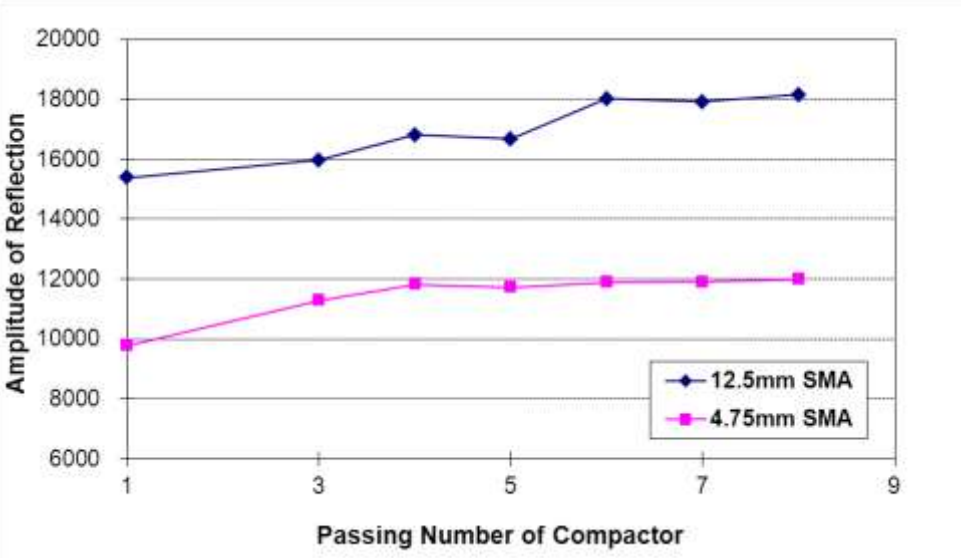

Figure 3.37 Relationship between GPR signal reflection amplitude and number of compactor passes.

3.3.4 Effect of Asphalt Mixture Temperature on GPR Measurements

Figure 3.38 plots the surface reflection amplitudes of the 12.5mm SMA at different temperatures. It is clear in this figure that, except for some random fluctuation, the reflection amplitude stays constant within the temperature range of 32 to 88 ^{o}C (90 to 190 ^{o}F), which indicates that within the testing temperature range, the temperature effect can be ignored when using the specific gravity model to predict the asphalt mixture density.

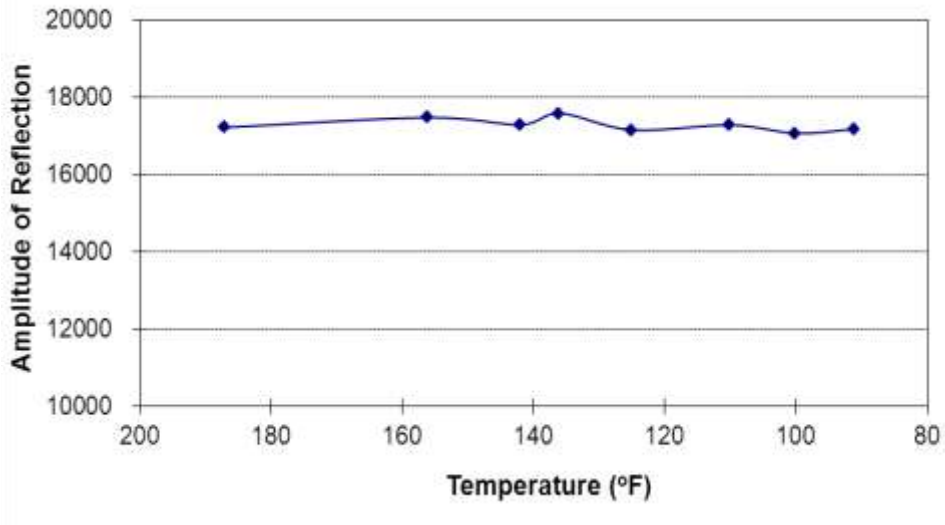

.

Figure 3.38 Relationship between the amplitude of GPR signal reflection and temperature.

3.3.5 Model Validation Using In-service Pavement Data

To verify the accuracy of the GPR density prediction using the ALL model, three different methods were used to measure the bulk specific gravities of the field cores in the lab: the SSD method, the Corelok vacuum method, and the physical method. The SSD method has been the most commonly used method for laboratory G_{mb} measurement, but it may produce large error for specimens with large air void contents. The Corelok method has recently gained increasing attention, because it is believed to provide more accurate measurement for specimens with large air void contents. The physical method is based on directly measuring the dimensions of the specimens (height and diameter) to calculate their volumes. Since none of these methods provides true G_{mb}, all of them were used in this study for comparison purpose.

Figures 3.39 to 3.43 present the laboratory measured G_{mb} of the five mixtures by using three different methods. It can be observed that the SSD and Corelok methods in general provided very close G_{mb} results, and the G_{mb} results from the physical method are a little different from the other two. In general, the physical method provided the lowest G_{mb} measurement. This is probably due to the over-estimated specimen volume by including the specimen surface irregularities. Table 3.17 shows the difference between the three methods by using the SSD method as a reference. Since the SSD method and Corelok method provided very close G_{mb}, the G_{mb} values from the SSD method were used as a reference in this study to evaluate the performance of the nuclear gauge and GPR.

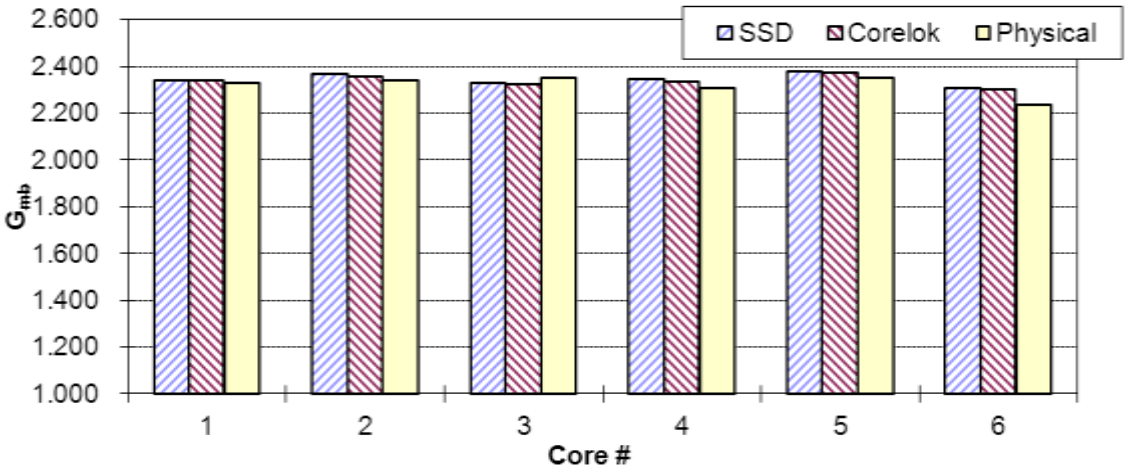

Figure 3.39 Laboratory-measured Gmb of quartzite mix cores.

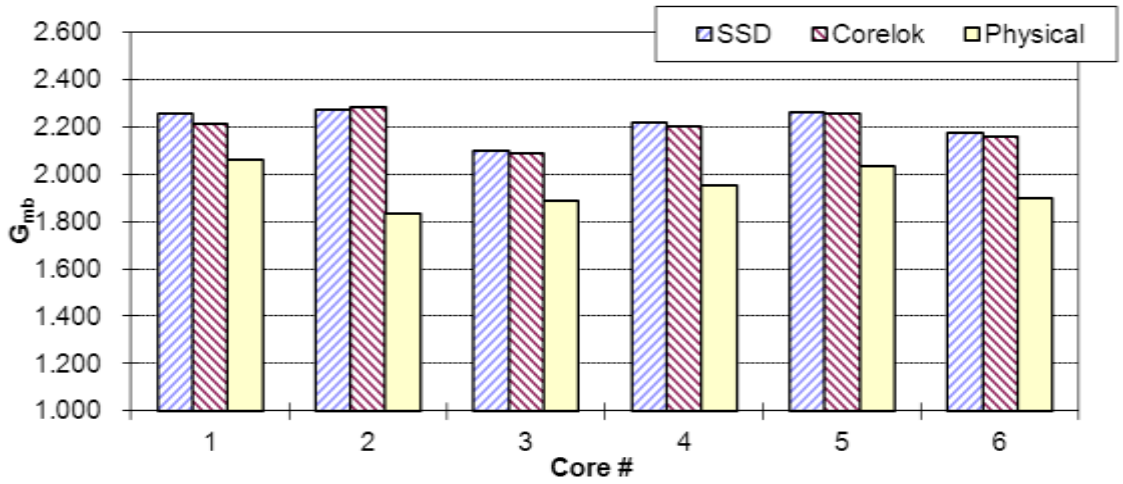

Figure 3.40 Laboratory-measured Gmb of 4.75mm SMA cores.

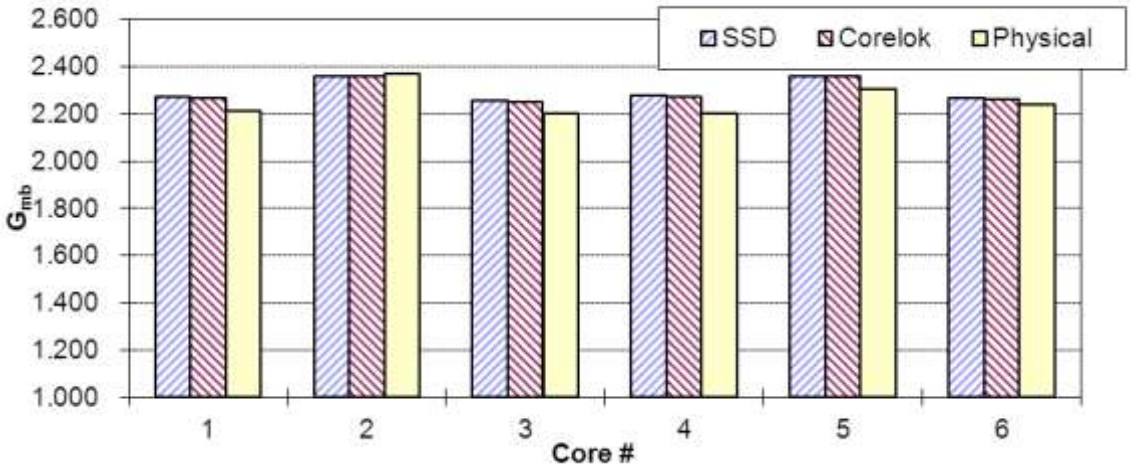

Figure 3.41 Laboratory-measured Gmb of sprinkle mix cores.

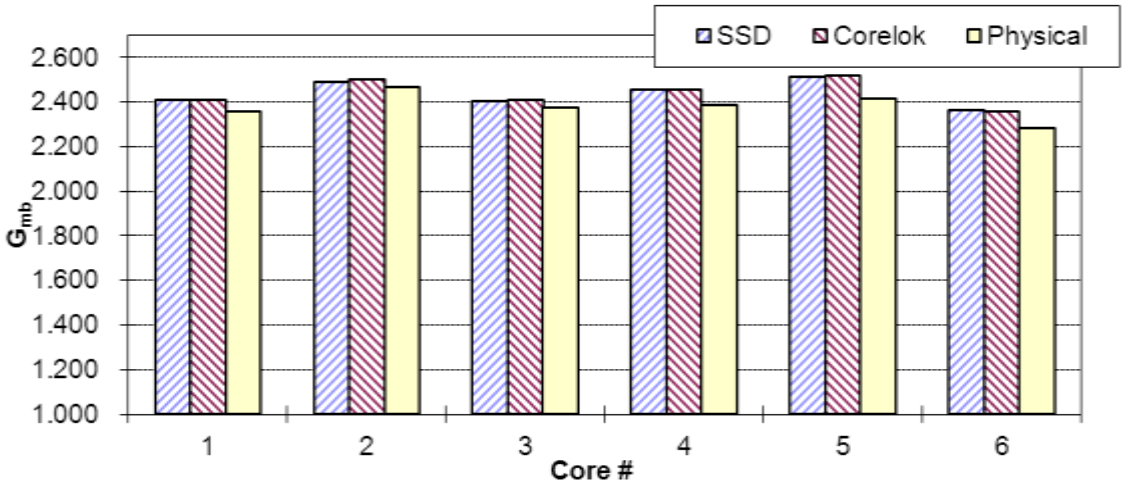

Figure 3.42 Laboratory-measured Gmb of slag/fiber mix cores.

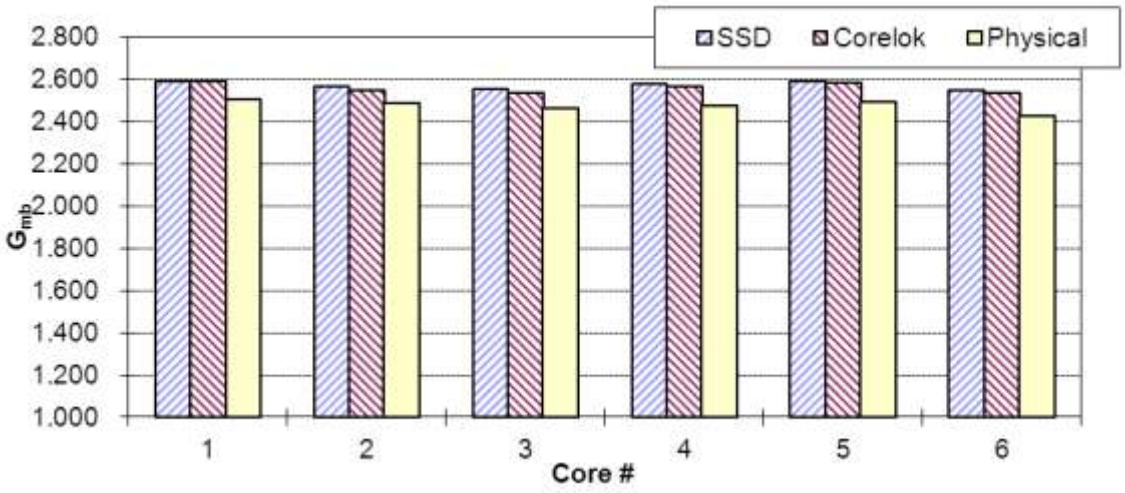

Figure 3.43 Laboratory-measured Gmb of friction mix cores.

Table 3.17 Relative Difference in Gmb between Various Laboratory Testing Methods

Relative Difference* between	Quartzite Mix	4.75mm SMA	Sprinkle Mix	Fiber/Slag Mix	Friction Mix
SSD and Corelok	0.3%	0.7%	0.2%	0.2%	0.4%
SSD and Physical	1.3%	11.7%	1.9%	2.4%	3.2%

** Relative difference is calculate by dividing the difference in G_{mb} between two methods by the G_{mb} measured using the SSD method.*

To employ the GPR measurements and the ALL model to predict the G_{mb} of the field cores, the data of the two cores in the central lane, cores #2 and #5 (Figure 3.36), were used to obtain the average values of ε_s of each mixture. The values of the parameters in the ALL model for each mixture are listed in Table 3.18. The ε_{AC} and G_{mb} values of cores #2 and #5 as shown in Table 3.19 were used to back-calculate the values of ε_s.

Table 3.18 Mixture Dielectric and Volumetric Properties

Mixture	P_b (%)	G_{mm}	G_{se}	G_b	ε_b	ε_s		
						Core #2	Core #5	Average
Quartzite Mix	5.8	2.504	2.744	1.015	3	7.47	7.72	7.60
4.75mm SMA	7.3	2.454	2.753	1.015	3	7.55	7.64	7.60
Sprinkle Mix	6.1	2.500	2.750	1.015	3	8.16	7.93	8.05
Fiber/Slag Mix	5.7	2.606	2.870	1.015	3	10.30	10.53	10.42
Friction Mix	5.1	2.700	2.958	1.015	3	12.28	11.63	11.96

Table 3.19 Measured and Gmb and εAC of Cores #2 and #5 of Each Mix

Mixture	Core #2		Core #5	
	G_{mb}	ε_{AC}	G_{mb}	ε_{AC}
Quartzite Mix	2.371	6.0	2.381	6.3
4.75mm SMA	2.272	5.7	2.263	5.7
Sprinkle Mix	2.353	6.4	2.357	6.3
Fiber/Slag Mix	2.481	8.1	2.462	8.2
Friction Mix	2.563	9.6	2.589	9.3

Using the parameters in Table 3.18 and the GPR-measured ε_{AC}, the G_{mb} of cores #1, 3, 4, and 6 for each mixture were predicted using the ALL model. Table 3.20 shows the predicted G_{mb} of these cores from GPR measurement as well as their prediction errors relative to the lab-measured G_{mb}. As a comparison, the G_{mb} of these cores measured by the nuclear density gauge are also listed.

Figure 3.44 shows a comparison of the average prediction error between the GPR method and nuclear gauge method for each mixture. It can be seen that for the three mixtures without slags: quartzite mix, 4.75mm SMA, and sprinkle mix, the performance of GPR is better than nuclear gauge. However, for the two mixtures with slags: slag/fiber mix, and friction mix, the prediction error of GPR increased and the nuclear gauge exhibited better performance. The average prediction errors of GPR are between 0.5% and 1.1% for mixtures without slags, which indicated that the prediction is very accurate. The relative larger error for the mixtures with slags is mainly due to the metal material inside the mixture. The metal material can be considered to have extremely high dielectric constant, and since its distribution is not uniform within the mixture, larger variation in GPR measurement from slag mixtures is expected.

In summary, the in-service pavement data successfully verified the accuracy of ALL model in predicting in-situ asphalt mixture density. In general, the performance of GPR was comparable to, or better than, the traditional nuclear gauge, when the ALL model was employed with two calibration cores.

Table 3.20 Core Gmb Predicted by GPR and Nuclear Gauge

Mixture/Core #		SSD G_{mb}	Air Void Content (%)	GPR		Nuclear Gauge	
				G_{mb}	Error* (%)	G_{mb}	Error* (%)
Quartzite Mix	1	2.342	6.5	2.322	0.8	2.384	1.8
	3	2.331	5.8	2.320	0.5	2.346	0.6
	4	2.346	7.2	2.369	1.0	2.384	1.6
	6	2.307	6.6	2.259	2.1	2.324	0.7
4.75mm SMA	1	2.261	5.1	2.225	1.6	2.287	1.1
	3	2.102	8.1	2.106	0.2	2.250	7.0
	4	2.219	9.7	2.206	0.6	2.245	1.2
	6	2.176	6.9	2.168	0.4	2.241	3.0
Sprinkle Mix	1	2.268	14.8	2.289	0.9	2.273	0.2
	3	2.255	10.2	2.261	0.3	2.340	3.8
	4	2.276	7.9	2.272	0.2	2.313	1.6
	6	2.262	11.9	2.250	0.6	2.310	2.1
Slag/Fiber Mix	1	2.402	9.5	2.424	0.9	2.413	0.5
	3	2.372	5.8	2.479	4.5	2.408	1.5
	4	2.478	10.1	2.456	0.9	2.450	1.1
	6	2.356	9.3	2.390	1.5	2.421	2.8
Friction Mix	1	2.589	5.7	2.684	3.7	2.630	1.6
	3	2.549	9.7	2.705	6.1	2.530	0.7
	4	2.577	7.9	2.618	1.6	2.541	1.4
	6	2.547	4.6	2.554	0.3	2.584	1.5

* *Error is calculated by dividing the absolute difference between the predicted G_{mb} and SSD G_{mb} by the SSD G_{mb}.*

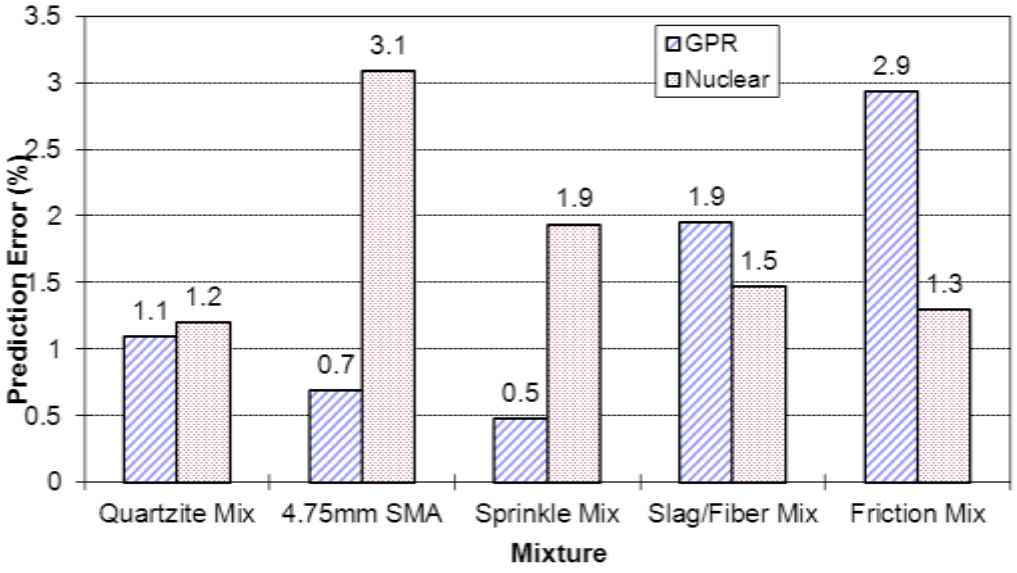

Figure 3.44 Prediction error comparison between GPR and nuclear density gauge.

3.4 Extended CMP Method with Two Air-coupled Bistatic Systems

The prediction of asphalt mixture density using GPR is based on the relation between asphalt mixture's density and dielectric constant. Therefore, the accuracy of the predicted density is largely dependent on the accuracy of the dielectric constant measurement.

Currently, the most commonly used method for pavement material dielectric constant estimation is based on the reflection amplitudes measured by an air-coupled GPR system, as described in Section 2.2.3. In this study, this method was also used to estimate asphalt mixture's dielectric constant in the test site and construction site. The advantage of this method is that it is easy to implement and provides reasonably accurate results. However, this method assumes that the pavement material is lossless (i.e., its conductivity is zero) and that the pavement material has uniform dielectric property through depth. This assumption is more suitable for newly built flexible pavements. However, it cannot provide reliable information for the whole layer, and the estimate error may increase when the asphalt mixture ages or when the asphalt layer is made of multiple lifts.

To improve the accuracy of the reflection amplitude method, another type of

methods based on the time delays of two GPR systems can be employed. The time-delay methods calculate the average dielectric constant of a material layer based on the average travel speed of the GPR wave within the layer. Thus, the results are more representative for the whole layer than that found by Equation 2.27, which is based on the surface reflection only and, therefore, does not consider any dielectric constant changes through the layer depth.

The most commonly used time-delay method is the common midpoint (CMP) technique, which is often employed in seismic tests to estimate the velocity of seismic waves (Schneider 1984). Similarly, this technique is also useful in estimating the velocity of EM waves in a material, and therefore in finding its dielectric constant according to Equation 2.19. The following section describes the principle of the CMP method for GPR testing as well as some existing applications.

3.4.1 Available CMP Methods for GPR Testing

Figure 3.45 illustrates the simplest CMP configuration that can be used to estimate the average EM velocity, v, within a single asphalt layer or within multiple layers with comparable dielectric constants, using one ground-coupled monostatic system (T1/R1) and one ground-coupled bistatic system (T2 and R2). By tracing the EM wave paths of the two GPR systems, the following two equations can be derived:

$$vt_1 = 2d_1 = \frac{ct_1}{\sqrt{\varepsilon_{r,1}}}, \tag{3.17}$$

$$vt_2 = 2\sqrt{d_1^2 + \left(\frac{x}{2}\right)^2}, \tag{3.18}$$

where d_1 is the unknown layer thickness, t_1 and t_2 are the two-way travel times of the monostatic and bistatic systems, respectively, x is the separation distance between the transmitter and receiver of the bistatic system, and c is the speed of light in free space.

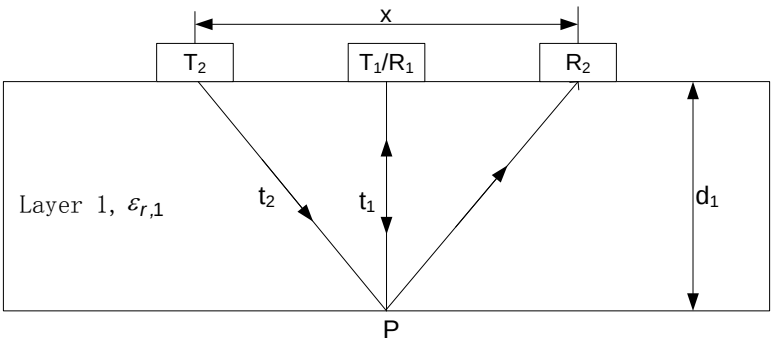

Figure 3.45 CMP geometry using ground-coupled monostatic and bistatic antennas.

Solving Equations 3.17 and 3.18 for $\varepsilon_{r,1}$ by eliminating the unknown d_1 leads to the following relation:

$$\varepsilon_{r,1} = \frac{c^2}{x^2}(t_2^2 - t_1^2). \tag{3.19}$$

Using the above equation, the dielectric constant of a material layer can be estimated based on the two-way travel times measured by the two GPR systems.

The aforementioned CMP configuration requires that one antenna system be ground-coupled monostatic and the other be ground-coupled bistatic. To expand the suitability of this method to more GPR systems, Lahouar et al. (2003) developed the modified CMP method using one ground-coupled monotonic system and one air-coupled bistatic system.

As depicted in Figure 3.46, the air-coupled bistatic antennae (T2 and R2) are set at a height of d_0 above the ground. The separation distance between the transmitter and receiver of the air-coupled system is x_0, and the distance between the incidence point and the reflection point of the air-coupled system on the air-layer interface is x_1, which is unknown because the dielectric constant of Layer 1, $\varepsilon_{r,1}$, the incidence angle θ_i, and the transmission angle θ_t, are unknown. From Figure 3.46, it is clear that Equation 3.19 holds when x is replaced by x_1, resulting in

$$\varepsilon_{r,1} = \frac{c^2}{x_1^2}(t_2^2 - t_1^2)\,. \tag{3.20}$$

Angles θ_i and θ_t are related according to the Snell's law of refraction (Balanis 1989),

$$\sqrt{\varepsilon_{r,0}}\,\sin\theta_i = \sqrt{\varepsilon_{r,1}}\,\sin\theta_t\,, \tag{3.21}$$

where $\varepsilon_{r,0}$ is the dielectric constant of air ($\varepsilon_{r,0}$=1).

Using the geometry of Figure 3.46, the following relations can be found:

$$2d_0 \tan\theta_i + x_1 = x_0\,, \tag{3.22}$$

$$\tan\theta_t = \frac{x_1}{2d_1} = \frac{x_1}{vt_1}\,, \tag{3.23}$$

where d_1 is the asphalt layer thickness.

Combining Equations 3.20 and 3.23 and solving for θ_t as a function of the two-way travel times t_1 and t_2 yields the following:

$$\tan\theta_t = \frac{\sqrt{t_2^2 - t_1^2}}{t_1}\,. \tag{3.24}$$

Finally, combining Equations 3.20, 3.22 and 3.23 gives the following relation, where only θ_i is unknown:

$$2d_0 \tan\theta_i + c\frac{\sin\theta_t}{\sin\theta_i}\sqrt{t_2^2 - t_1^2} = x_0\,. \tag{3.25}$$

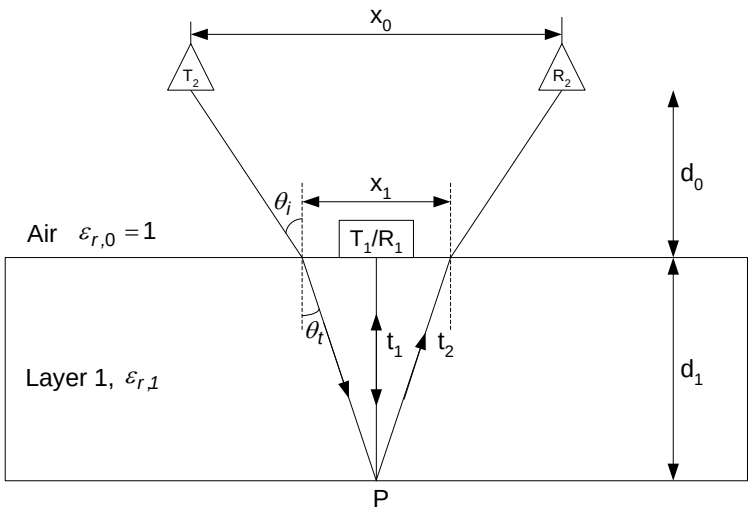

Figure 3.46 Modified CMP geometry using a ground-coupled monostatic system and an air-coupled bistatic system.

To estimate $\varepsilon_{r,1}$ and d_1 using the modified CMP technique utilizing one ground-coupled monostatic system and one air-coupled bistatic system, Lahouar et al. (2002) proposed the following algorithm:

1. Estimate the reflection times t_1 and t_2 corresponding to the two-way travel times in Layer 1 obtained by the ground-coupled and air-coupled system, respectively.
2. Calculate the transmission angle θ_t using Equation 3.24.
3. Solve Equation 3.25 numerically to find the angle of incidence θ_i.
4. Use Equation 3.21 to find $\varepsilon_{r,1}$.
5. Calculate the thickness of Layer 1 using $d_1 = \frac{c}{2\sqrt{\varepsilon_{r,1}}} t_1$.

As Figure 3.47 shows, the above algorithm was implemented in a study by Lahouar et al. (2002) to predict the asphalt layer thickness of a section of I-81 built between 1963 and 1965. The survey was conducted using a combination of a 900MHz ground-coupled antenna and a 1GHz air-coupled antenna system. It was reported that the thickness prediction errors ranged from 1% to 15% with a mean error of 6.8%. These errors were attributed mainly to the inaccurate localization of the surface reflection from the ground-

coupled antenna, which is usually overlapped with the coupling pulse (Figure 2.13). In addition, the use of ground-coupled antenna entailed a relatively low survey speed, imposing yet another limitation on this technique.

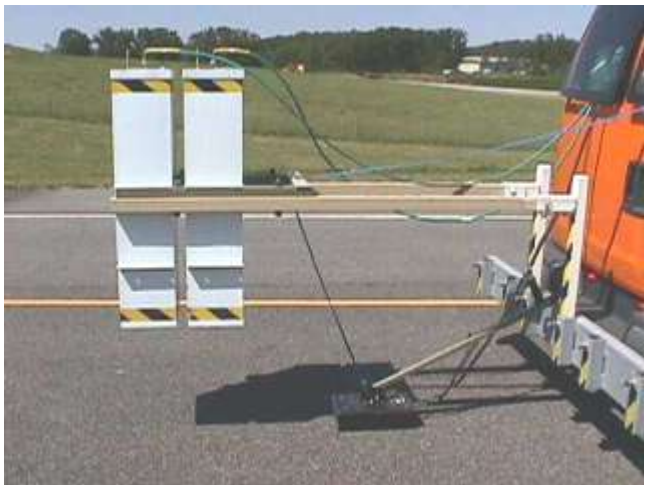

Figure 3.47 CMP configuration using a ground-coupled monostatic system and an air-coupled bistatic system (Lahouar et al. 2002).

3.4.2 Extended CMP Method with Two Air-Coupled Bistatic Systems

In this research, the feasibility of an extended CMP (XCMP) method by using two air-coupled bistatic systems was investigated. The motivation for this investigation was to develop a CMP method capable of being performed at a high survey speed. Moreover, by avoiding using the ground-coupled antenna system, the EM-wave travel times within the asphalt layer can be more accurately determined, thereby producing a more accurate estimate of the mixture's dielectric constant.

As illustrated in Figure 3.48, the XCMP method has both air-coupled bistatic systems (T1/R1 and T2/R2) set at height d_0 above the ground. The separation distance between the transmitter and receiver of the inner system (T1/R1) is x_{01} and that of the outer system (T2/R2) is x_{02}. The distance between the incidence point and the reflection point of T1/R1 is x_1, and that of T2/R2 is x_2. x_1 and x_2 are unknown, because the dielectric constant of Layer 1 $\varepsilon_{r,1}$, the incidence angles θ_{i1}, θ_{i2}, and the transmission angles θ_{t1}, θ_{t2}, are unknown.

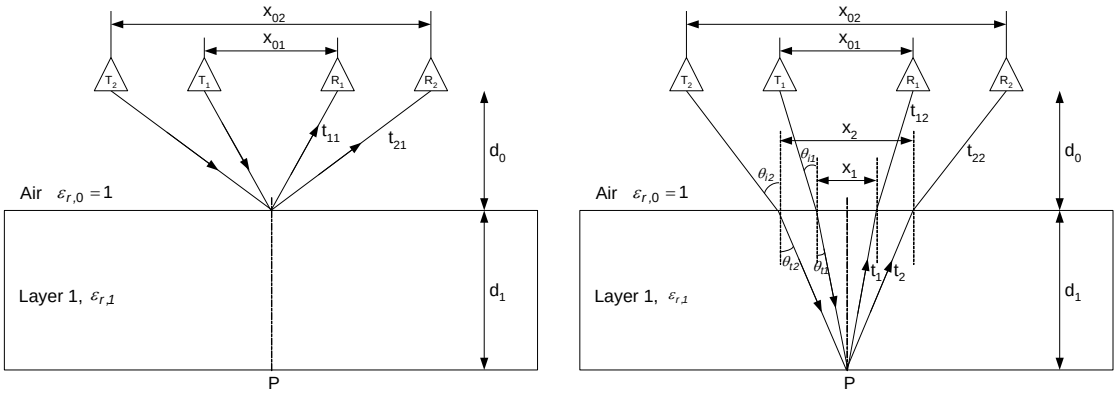

Figure 3.48 XCMP geometry using two air-coupled bistatic systems: (a) reflection at Layer 1 surface; (b) reflection at the Layer 1 bottom.

According to Snell's law, the following relations exit:

$$sin\theta_{i1}\sqrt{\varepsilon_{r,0}} = sin\theta_{t1}\sqrt{\varepsilon_{r,1}} \text{ , i.e. } sin\theta_{i1} = sin\theta_{t1}\sqrt{\varepsilon_{r,1}} \text{ ,} \tag{3.26}$$

$$sin\theta_{i2}\sqrt{\varepsilon_{r,0}} = sin\theta_{t2}\sqrt{\varepsilon_{r,1}} \text{ , i.e. } sin\theta_{i2} = sin\theta_{t2}\sqrt{\varepsilon_{r,1}} \text{ .} \tag{3.27}$$

Combining Equations 3.26 and 3.27 and eliminating $\varepsilon_{r,1}$ yields:

$$\frac{sin\theta_{i1}}{sin\theta_{i2}} = \frac{sin\theta_{t1}}{sin\theta_{t2}} \text{ .} \tag{3.28}$$

From the geometry in Figure 3.48(b), the following relations can be obtained:

$$vt_1 = \frac{ct_1}{\sqrt{\varepsilon_{r,1}}} = 2\sqrt{d_1^2 + (\frac{x_1}{2})^2} \text{ ,} \tag{3.29}$$

$$vt_2 = \frac{ct_2}{\sqrt{\varepsilon_{r,1}}} = 2\sqrt{d_1^2 + (\frac{x_2}{2})^2}\ , \tag{3.30}$$

$$sin\theta_{t1} = \frac{x_1 / 2}{vt_1 / 2} = \frac{x_1\sqrt{\varepsilon_{r,1}}}{ct_1}, \tag{3.31}$$

$$sin\theta_{t2} = \frac{x_2 / 2}{vt_2 / 2} = \frac{x_2\sqrt{\varepsilon_{r,1}}}{ct_2}, \tag{3.32}$$

$$tan\,\theta_{i1} = \frac{x_{01} - x_1}{2d_0}, \tag{3.33}$$

$$tan\,\theta_{i2} = \frac{x_{02} - x_2}{2d_0}, \tag{3.34}$$

where t_1 and t_2 are the two-way travel times within Layer 1 of T1/R1 and T2/R2, respectively (Figure 3.48(b)).

Combining Equations 3.29 and 3.30 by eliminating d_1 results in

$$\varepsilon_{r,1} = \frac{c^2(t_2^2 - t_1^2)}{x_2^2 - x_1^2}. \tag{3.35}$$

Plugging Equations 3.31 and 3.32 into Equations 3.26 and 3.27, respectively, and then applying Equation 3.35 result in the following:

$$sin\theta_{i1} = \frac{x_1}{ct_1}\varepsilon_{r,1} = \frac{x_1}{t_1}c\frac{t_2^2 - t_1^2}{x_2^2 - x_1^2}, \tag{3.36}$$

$$sin\theta_{i2} = \frac{x_2}{ct_2}\varepsilon_{r,1} = \frac{x_2}{t_2}c\frac{t_2^2 - t_1^2}{x_2^2 - x_1^2}. \tag{3.37}$$

Combining Equations 3.36 and 3.37, and Equations 3.33 and 3.34 by applying the triangular relation, $tan^2\theta + 1 = \frac{1}{1 - sin^2\theta}$, yields the following two equations:

$$(\frac{x_{01} - x_1}{2d_0})^2 + 1 = \frac{t_1^2(x_2^2 - x_1^2)^2}{t_1^2(x_2^2 - x_1^2)^2 - x_1^2c^2(t_2^2 - t_1^2)^2}, \tag{3.38}$$

$$(\frac{x_{02} - x_2}{2d_0})^2 + 1 = \frac{t_2^2(x_2^2 - x_1^2)^2}{t_2^2(x_2^2 - x_1^2)^2 - x_2^2c^2(t_2^2 - t_1^2)^2}. \tag{3.39}$$

In the above two equations, there are four unknowns: x_1, x_2, t_1, and t_2. It should be noted here that t_1 and t_2 are not the same as the Δt_1 and Δt_2 shown in Figure 3.49, which are the differences in the two-way travel times between the surface reflections and bottom reflections of the two GPR systems, respectively. Instead, the following relations exist:

$$\Delta t_1 = t_{12} + t_1 - t_{11}, \tag{3.40}$$

$$\Delta t_2 = t_{22} + t_2 - t_{21}, \tag{3.41}$$

where t_{11} and t_{22} are the two-way travel times of the surface reflections of T1/R1 and T2/R2, respectively (Figure 3.48(a)); t_{12} and t_{22} are the above-surface two-way travel times of the bottom reflections of T1/R1 and T2/R2, respectively (Figure 3.48(b)).

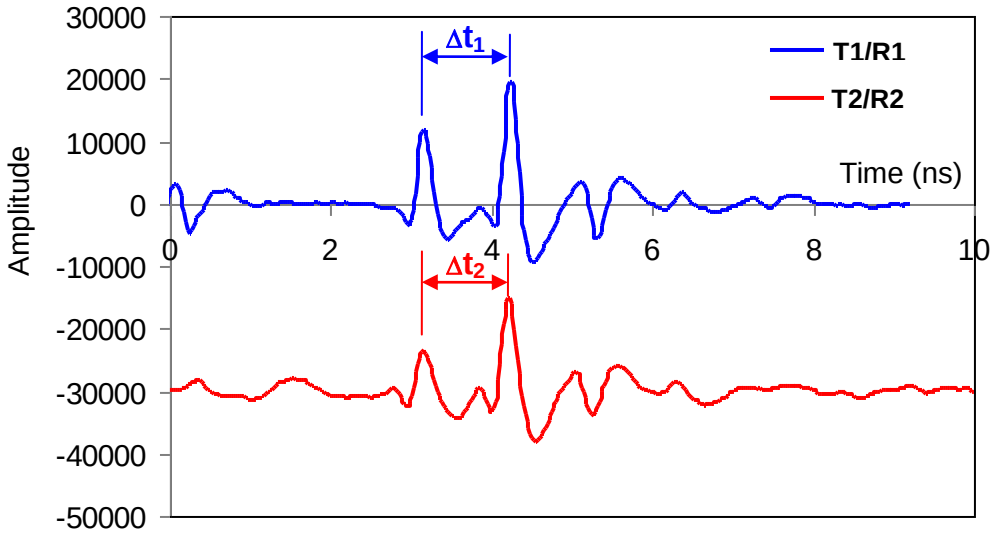

Figure 3.49 Example GPR data using the CMP technique with two air-coupled bistatic systems.

Equations 3.40 and 3.41 can be rewritten as

$$t_1 = \Delta t_1 + t_{11} - t_{12}, \tag{3.42}$$

$$t_2 = \Delta t_2 + t_{21} - t_{22}. \tag{3.43}$$

From the geometry in Figure 3.48, the following relations can be found:

$$t_{11} = \frac{2\sqrt{{d_1}^2 + {x_{01}}^2 / 4}}{c}, \tag{3.44}$$

$$t_{12} = \frac{2\sqrt{{d_1}^2 + (x_{01} - x_1)^2 / 4}}{c}, \tag{3.45}$$

$$t_{21} = \frac{2\sqrt{{d_1}^2 + {x_{02}}^2 / 4}}{c}, \tag{3.46}$$

$$t_{22} = \frac{2\sqrt{d_1^{\,2} + (x_{02} - x_2)^2 / 4}}{c}. \tag{3.47}$$

Plugging the above four equations into Equations 3.42 and 3.43 yields:

$$t_1 = \Delta t_1 + \frac{\sqrt{4d_1^{\,2} + x_{01}^{\,2}}}{c} - \frac{\sqrt{4d_1^{\,2} + (x_{01} - x_1)^2}}{c}, \tag{3.48}$$

$$t_2 = \Delta t_2 + \frac{\sqrt{4d_1^{\,2} + x_{02}^{\,2}}}{c} - \frac{\sqrt{4d_1^{\,2} + (x_{02} - x_2)^2}}{c}. \tag{3.49}$$

Since Δt_1 and Δt_2 can be measured from the GPR data, the following algorithm can be implemented to measure the Layer 1 dielectric constant and thickness using the XCMP method:

1. Obtain the two-way travel time differences between the surface and bottom reflections of the two GPR systems, Δt_1 and Δt_2, from the GPR data;
2. Plug Δt_1 and Δt_2 into Equations 3.48 and 3.49 to find the two-way travel times within Layer 1 of the two GPR systems, t_1 and t_2;
3. Numerically solve Equations 3.38 and 3.39 to determine the distances between the incidence point and reflection point of the two systems, x_1 and x_2;
4. Calculate the dielectric constant of Layer 1 using Equation 3.35; and
5. Calculate the dielectric constant of Layer 1 using $d_1 = \sqrt{(\frac{ct_1}{2\sqrt{\varepsilon_{r,1}}})^2 - (\frac{x_1}{2})^2}$.

3.4.3 Implementation of the XCMP Method

The previous section described the theoretical equations and implementation algorithm for the XCMP method. In this section, the practical implementation of this method to predict the asphalt pavement dielectric constant and layer thickness will be introduced.

To achieve the XCMP antenna configuration, two 2 GHz air-coupled bistatic GPR

systems manufactured by the Geophysical Survey Systems, Inc. (GSSI), as shown in Figure 3.50, were used in this study. As Figure 3.51 illustrates, each antenna case actually contains two antennas inside: one as a transmitter (T) and the other as a receiver (R). However, it should be noted that since these commercial GPR systems seal and fix the antenna pairs inside the cases, the separation distance of each antenna pair cannot be changed.

As described in the previous section, the two-way travel time differences between the surface and bottom reflections of the two antenna pairs, Δt_1 and Δt_2, are needed to calculate the dielectric constant and layer thickness of the asphalt pavement surface. However, due to the relative small thickness of the asphalt pavement layer and the extremely high speed of GPR waves, the difference between Δt_1 and Δt_2 is usually very small (approximately 0.02 ns to 0.1 ns). Therefore, to ensure the successful application of the XCMP method, GPR systems with high time-resolution must be used.

Figure 3.50 GPR antenna systems used for the XCMP method.

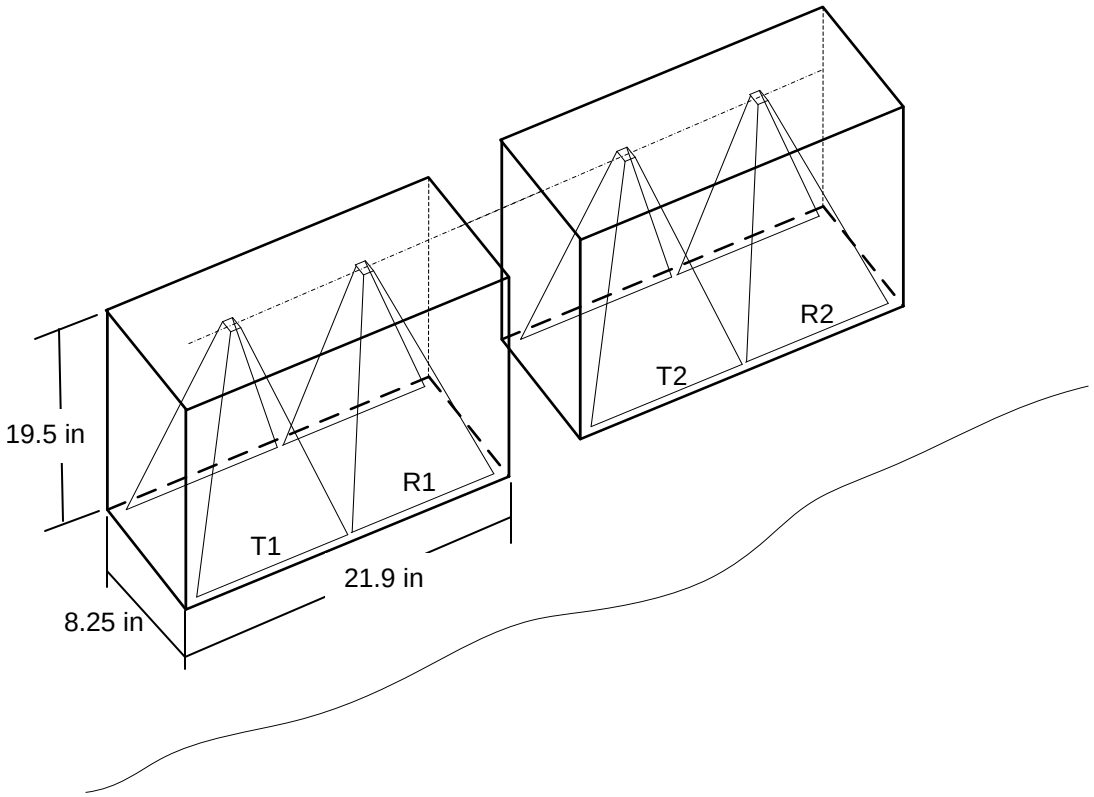

Figure 3.51 Schematic of antennas inside the antenna case.

To make the difference between Δt_1 and Δt_2 as large as possible, two different antenna setups were attempted in this study (Figure 3.52): using T2/R1 as the inner antenna pair and T1/R2 as the outer antenna pair, and using T2/R2 as the inner antenna pair and T1/R2 as the outer antenna pair. For both setups, the two antenna cases were placed at the same height above the ground. The two antennas were aligned with their long edges in the driving direction. Some trial tests were conducted in this study to compare these two setups. It was found that the second setup could provide larger difference between Δt_1 and Δt_2 by increasing the separation distance between the two antenna cases. Therefore, this setup was selected in this study. To avoid the effect of the metal frames in the GPR van on the GPR signal, an optimum separation distance between the centers of the two antenna cases was found at 91.4 cm (36.0 in).

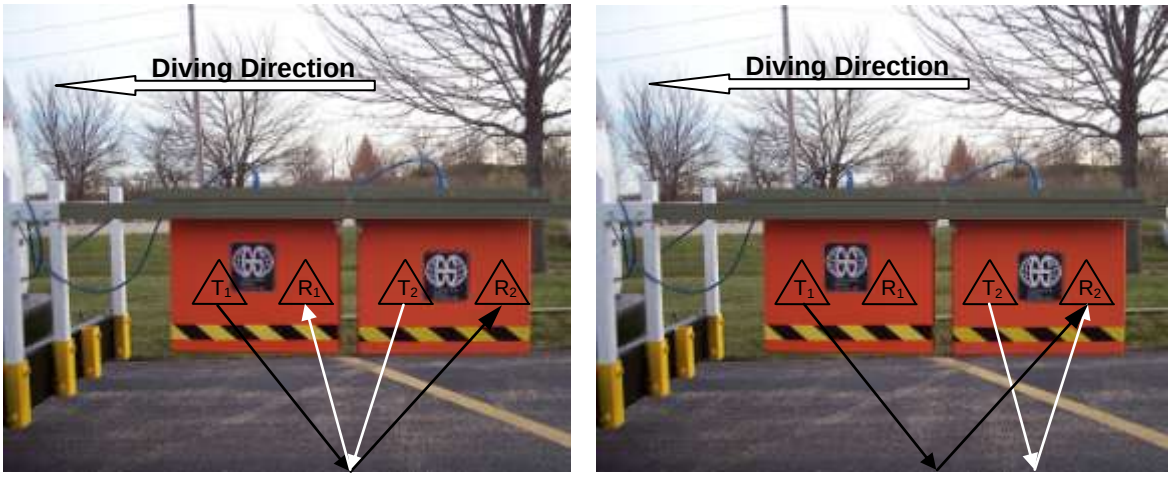

(a) (b)

Figure 3.52 XCMP antenna setup: (a) T2/R1 and T1/R2; (b) T2/R2 and T1/R2 (selected setup).

The maximization of the time resolution of the available GPR systems was achieved by maximizing the sampling rate, i.e. number of sampling points in each GPR scan, while at the same time minimizing the range of the GPR signal. For the GPR systems used in this study, the maximum workable sampling rate is 1024 samples/scan and it was used in this study. The minimum signal range is dependent on the pavement layer thickness. Approximately, a minimum range of 2 ns is required for a 5-cm (2-in) thick asphalt layer, and a minimum range of 6 ns is required for a 20-cm (8-in) thick asphalt layer.

Once the GPR system setup was selected, the locations of the antennas needed to be determined to use the XCMP equations. Remember that all the antennas were treated as points when deriving the theoretical equations for the XCMP method. These artificial points are known as the antenna phase centers, where the EM waves are assumed to be sent or received. According to GSSI, the separation distance between the feed points of the transmitter and receiver within each antenna case is 38.0 cm (15.0 in). Due to the symmetry of the antenna structure, the separation distance between the phase centers is same as that between the feed points. Therefore, only the height of the phase centers needs to be determined. In this study, the height of the phase centers was obtained by using calibration cores, and it was found that the phase centers are 35.8 cm (14.1 in)

above the antenna case bottom. Since the antenna case bottoms were set at 55.9 cm (22 in) above the ground during survey, the height of the phase centers above the pavement surface was 91.7 mm (36.1 in). Table 3.21 summarizes antenna phase center location parameters for the selected XCMP antenna setup. In this table, x_{01} is the separation distance between antennas T2 and R2; x_{02} is the separation distance between antennas T1 and R2, which is equal to the sum of distance between T2 and R2 and the distance between the center of the two antenna cases, which is 91.4 cm (36 in); and d_0 is the height of the two antenna pairs above the pavement surface.

Table 3.21 Antenna Phase Center Location Parameters

x_{01} (cm)	x_{02} (cm)	d_0 (cm)
35.8	126.2	91.7

After the GPR system setup was selected (Figure 3.35b) and the phase center locations were determined, this study implemented the XCMP method to predict the dielectric constant and layer thickness of Lane I(A) in the test site, which contains four sections with different thicknesses. Two GPR surveys with the XCMP setup were conducted: one along the centers of the steel plates on the south side, and the other along the centers of the steel plates on the north side (Figure 3.11).

Figure 3.53 shows the raw GPR images from these two surveys. As the figure shows, with the XCMP setup, two sets of GPR data were collected simultaneously in each survey: one from the antenna pair T1/R2, and the other from the antenna pair T2/R2. The plateau shapes in these GPR images indicate the locations of the steel plates buried at different depth underneath the pavement surface. It should be noted that in order to match the data of the two antenna pairs, i.e. making them share the common midpoint, the data from T2/R2 should be shifted forward 45.7 cm (18.0 in), because the separation distance between the centers of the two antenna cases was 91.4 cm (36.0 in).

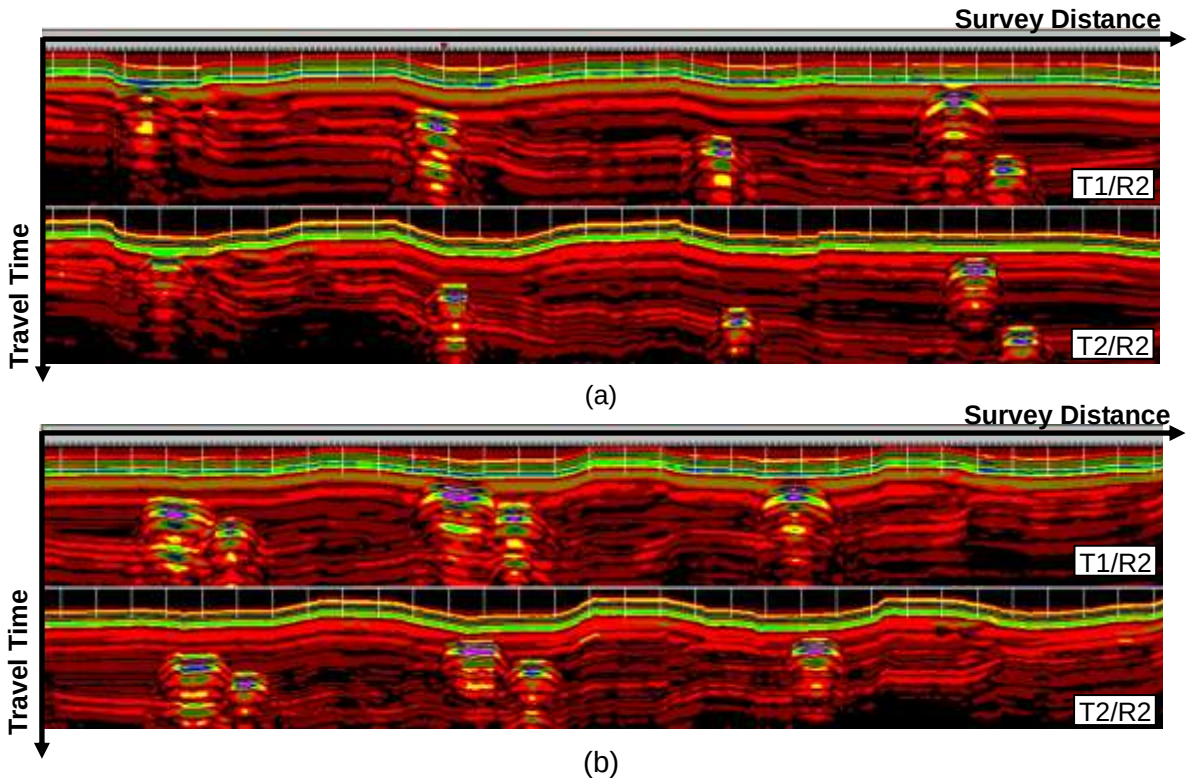

Figure 3.53 GPR B-scan image of Lane I(A) using the XCMP setup (a) south side (from east to west); (b) north side (from west to east).

After the GPR data was collected, the implementation algorithm presented in Section 3.4.2 was applied to predict the dielectric constant and layer thickness of Lane I(A). To assess the accuracy of the XCMP method, the layer thickness predicted by the XCMP method was compared to the real pavement thickness, which was obtained by extracting cores from Lane I(A). In total, ten cores were extracted at the centers of the steel plates (Figure 3.11). Among these ten cores, four cores have one single lift, three cores have two lifts, two cores have three lifts, and one core has four lifts, as shown in Figure 3.54. Each lift is approximately 5 cm (2 in) thick.

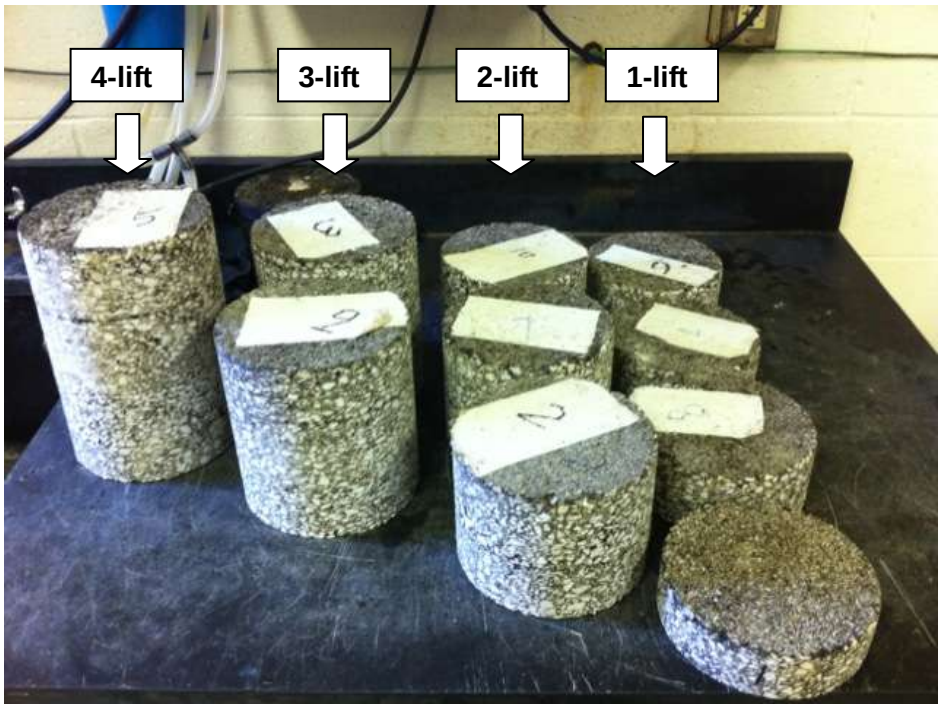

Figure 3.54 Cores extracted from Lane I(A).

Table 3.22 presents the GPR-measured Δt_1 and Δt_2 at each core location. From Δt_1 and Δt_2, the dielectric constants and thicknesses of the field cores were calculated by numerically solving Equations 3.38 and 3.39 using the MATLAB codes shown in Appendix E. The lab-measured core thicknesses were used as a reference to calculate the thickness prediction errors of the XCMP method. For comparison purpose, the dielectric constants and thicknesses of the field cores were also predicted by using the traditional surface-reflection method, as shown in Table 3.23.

Table 3.22 Predicted Core Dielectric Constant and Thickness Using the XCMP Method

Core #		Δt_1 (ns)	Δt_2 (ns)	Dielectric Constant	XCMP Thickness (in)	Core Thickness (in)		Thickness Prediction Error (%)
						Average	COV* (%)	
South Side	1	0.675781	0.660156	6.4	1.59	1.78	0.7	10.7
	2	1.833984	1.789063	6.0	4.44	4.48	0.1	0.9
	3	2.871094	2.798828	5.7	7.10	7.02	0.1	1.1
	4	0.896484	0.880859	8.4	1.83	2.38	1.2	22.9
	5	3.597656	3.507813	5.7	8.91	8.69	0.8	2.5
North Side	6	1.859375	1.812500	5.7	4.60	4.49	0.3	2.4
	7	2.701172	2.634766	5.8	6.64	6.51	0.1	2.0
	8	0.966797	0.943359	6.0	2.33	2.49	0.8	6.4
	9	1.978516	1.927734	5.6	4.95	4.75	0.3	4.2
	10	0.998047	0.970703	5.3	2.56	2.50	0.6	2.4

**COV represents coefficient of variance*

Table 3.23 Predicted Core Dielectric Constant and Thickness Using the Surface-Reflection Method

Core #		Dielectric Constant	Surface-reflection Thickness (in)	Core Thickness (in)		Thickness Prediction Error (%)
				Average	COV* (%)	
South Side	1	5.3	1.72	1.78	0.7	3.4
	2	5.2	4.72	4.48	0.1	5.4
	3	6.4	6.67	7.02	0.1	5.0
	4	5.9	2.28	2.38	1.2	4.0
	5	5.4	9.28	8.69	0.8	6.8
North Side	6	5.3	4.75	4.49	0.3	5.8
	7	6.2	6.31	6.51	0.1	3.1
	8	5.2	2.57	2.49	0.8	3.2
	9	5.5	4.84	4.75	0.3	1.9
	10	5.4	2.57	2.50	0.6	2.8

**COV represents coefficient of variance*

Figure 3.55 shows a comparison of the thickness prediction error between the XCMP method and the surface-reflection method. In this figure, the prediction errors of the two methods were plotted against the core thickness. Obviously, the XCMP outperformed the surface-reflection method for thick multi-lift pavement cores (thickness > 10 cm or 4 in), with only one exception which is the 4.75-in core. However, for thin single-lift pavement cores (thickness < 10 cm or 4 in), the XCMP method provided much larger errors than the surface-reflection method.

The different performances of the XCMP method in thin and thick pavements were mainly caused by the sampling rate limitation of the GPR systems. For thin pavements, the difference between Δt_1 and Δt_2 is so small (around 0.02 ns) that the current GPR systems (resolution around 0.003 ns) may not be able to accurately catch such small difference. However, for thick pavements, the difference between Δt_1 and Δt_2 is relatively large (0.05 ns to 0.1 ns). Thus, the effect of the GPR sampling rate is diminished. Another fact that may have contributed to the large errors of the XCMP method in thin pavements is the possible signal overlap between the signal surface and bottom reflections. For example, Figure 3.56 shows the GPR signal collected at one of the thin single-lift core locations. It can be seen that the surface reflection and bottom reflection are very close to each other. Although the peak locations of the two reflection pulses are clearly separated, the tail part of the bottom reflection may have affected the peak location of the surface reflection. Because the XCMP method is highly sensitive to the accurate measurement of Δt_1 and Δt_2, any slight overlap between the surface and bottom reflections may cause relatively large errors to the estimated dielectric constant and layer thickness.

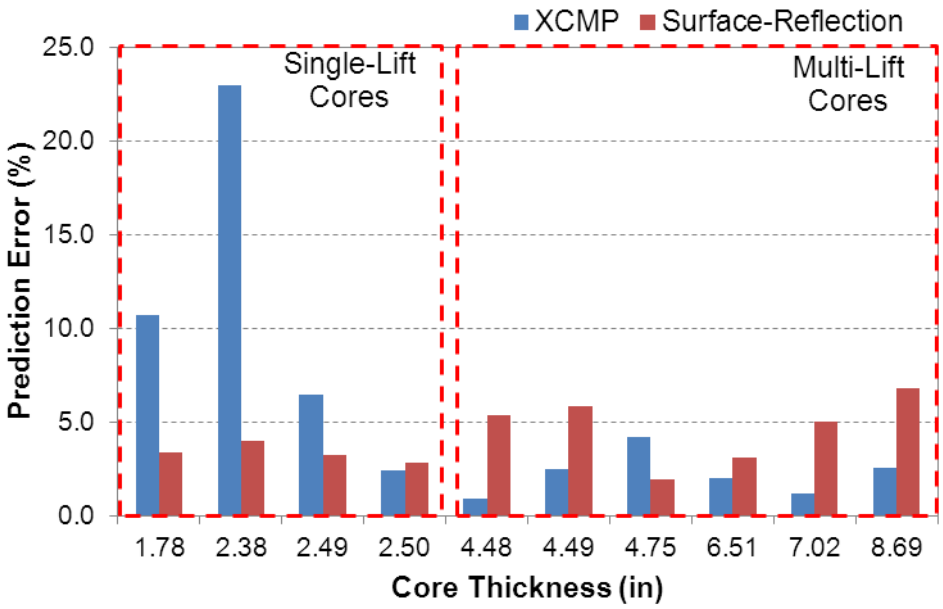

Figure 3.55 Prediction error comparison between the XCMP method and the surface-reflection method.

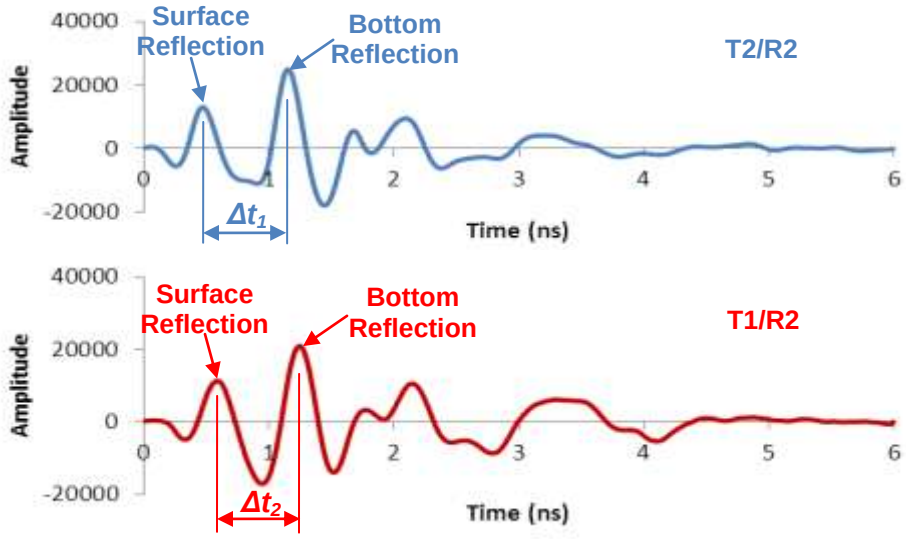

Figure 3.56 GPR data collected at one of the single-lift core locations.

3.4.4 Summary

In this section, the XCMP method, using two air-coupled bistatic GPR systems, was developed for pavement surface dielectric constant estimation. Based on the data collected from two air-coupled GPR systems, which share the common midpoint, the average (or bulk) dielectric constant and the thickness of the asphalt pavement surface can be determined. As a result, this technique works better for pavements containing multi-lifts or pavements with non-uniform properties through depth, compared to the classic method based on surface reflection. In addition, since this method eliminates the usage of ground-coupled antenna, the time delays of the two GPR systems can be more accurately estimated, and a higher GPR survey speed can be achieved.

The equipment setup for the XCMP method was accomplished using two commercial 2 GHz air-coupled GPR systems in this study. The reliability and accuracy of the XCMP method were evaluated using the data collected from Lane I(A) of the test site, which contained sections with different thicknesses. It was found that the XCMP method produced smaller thickness errors than the surface-reflection method for thick multi-lift pavement sections, while for thin single-lift pavement sections with a thickness around 4.3 to 6.3 cm (1.7 in to 2.5 in), the performance of the XCMP method was not as good as the surface-reflection method. Factors accounting for this include the sampling rate limitation of the GPR systems, as well as the possible overlap of the GPR signal reflections at the surface and bottom of the asphalt layers.

The GPR systems used in this study had a maximum workable sampling rate of 1024 samples/scan. When GPR systems with higher sampling rates are used, the accuracy of this method is expected to be further increased. In addition, both GPR systems used in this study are bistatic, and they fix and seal the antennas within the antenna case. The configuration of using a monostatic air-coupled system and a bi-static system with adjustable separation distance between transmitter and receiver may also enhance this technique by increasing the difference between Δt_1 and Δt_2.

3.5 In-situ Asphalt Mixture Density Prediction Using GPR: An Implementation Plan

To facilitate the task for pavement engineers to employ GPR as a nondestructive tool for in-situ asphalt mixture density prediction in practice, an implementation plan was proposed based on the outcome of this study and is presented in this section. This implementation plan covers the GPR equipment selection, asphalt mixture information collection, aggregate dielectric constant determination, GPR data collection, and density prediction using GPR data and specific gravity model.

3.5.1 GPR Equipment Selection

For the purpose of asphalt pavement density estimation, an air-coupled GPR system is preferred over a ground-coupled GPR system because of the following facts:

a. The ground-coupled antenna signal has overlap between the coupling and surface reflection pulses (Figure 2.13), which makes it difficult to determine the accurate surface reflection amplitude and the exact time when the signal is reflected at the pavement surface, resulting in errors in the dielectric constant estimation of the asphalt pavement surface.

b. The air-coupled antenna system allows data collection at a high survey speed (up to 96 km/h or 60 mph) while the ground-coupled system is usually conducted at a much lower speed.

c. Ringing noise may be a problem for the ground-coupled antenna system, especially when the pavement surface layer is thin. For GPR practitioners, the term signal ringing describes an artifact in GPR data where a response to a shallow feature “echoes” and repeatedly overlaps onto responses to deeper features. The ringing noise may mask responses to real features.

Currently, the most common central frequencies of the air-coupled GPR systems available in market are 1 GHz and 2 GHz. Although 2 GHz air-coupled antennas were used in this study, antennas with both frequencies can be used for asphalt pavement density prediction. However, if the GPR survey is conducted for thin asphalt pavement surfaces (less than or equal to 51cm or 2 in thick), 2 GHz antennas are recommended, because 1 GHz antenna signals may have significant overlaps between asphalt layer

surface and bottom reflections, which may affect the accuracy of dielectric constant estimation.

To synchronize the GPR measurement with the test location, a distance measuring instrument (DMI) or GPS should be used. When a DMI is used, the starting location of the GPR survey should be recorded as a reference point.

3.5.2 Asphalt Mixture Information Collection

To predict asphalt mixture bulk specific gravity using GPR measurement, some basic mixture properties are needed in the specific gravity model. These properties include the maximum specific gravity of asphalt mixture (G_{mm}), effective specific gravity of aggregate (G_{se}), asphalt binder content (P_b), and aggregate type. All this information can be obtained from the design of the paved mixture. However, if there is significant difference between the actually produced mixture and the designed mixture, the properties of the actually produced mixture should be measured and used.

3.5.3 Aggregate Dielectric Constant Determination

After the basic mixture information is collected, the dielectric constant of aggregate (ε_s) needs to be determined to ensure the accurate prediction of the asphalt mixture density. The recommended method to acquire this value is to use calibration cores. GPR data should be collected at the core locations before coring to obtain the dielectric constant of asphalt mixture (ε_{AC}), and the bulk specific gravity (G_{mb}) of the extracted cores should be measured in the lab. Then by plugging ε_{AC} and G_{mb} of the cores into the specific gravity model, the values of ε_s can be back-calculated. Once the value of ε_s for a certain mixture is obtained, this value can be stored in the database, and directly used in the future when the same mixture is paved.

Note that since ε_s is the only unknown parameter in the specific gravity model, theoretically the data of one core will be sufficient to solve the value of ε_s. However, to obtain a more reliable value of ε_s, at least two cores are recommended in the field and the average value of ε_s should be used.

In addition to using calibration cores, the value of ε_s can also be determined by using the GPR-predicted ε_{AC} and nuclear-gauge-measured G_{mb} at the same pavement location. The advantage of this method is that it makes the density prediction a completely

nondestructive process. However, the accuracy of this method is relying on the accuracy of nuclear gauge, because all GPR predictions will be based on the nuclear gauge measurement as a reference.

3.5.4 GPR Data Collection

The main purpose of the GPR data collection is to obtain the longitudinal dielectric constant profile of the asphalt pavement, which can be used as the input to the specific gravity model. To minimize the effect of water on the dielectric constant estimation, it is recommended that the GPR survey should be conducted when there are at least three days without raining before testing.

To estimate the dielectric constant of a thin single-lift asphalt pavement surface, which is probably the most common case in practice, the surface-reflection method (Equation 2.27) is recommended for obtaining the asphalt pavement surface dielectric constant. This method is easy to implement and has been proved to provide good performance based on the field verification results in this study. When the bulk density of a multi-lift thick asphalt pavement needs to be measured, the XCMP method presented in Section 3.4 can be used. This method requires two air-coupled systems with high sampling rates to work together. But it provides more accurate dielectric constant estimation when the pavement inhomogeneity through depth is an issue.

3.5.5 Density Prediction Using GPR Data

The final step is to input the basic mixture information, the dielectric constant of aggregate, and the dielectric constant profile of the asphalt pavement into the specific gravity model to predict the bulk specific gravity profile of the asphalt pavement. Based on the outcome of this study, the ALL model has been proved to be the best-performance model for the density prediction. Therefore, this specific gravity model is recommended to be used in practice to predict the specific gravity or air void content profile of asphalt pavement.

3.5.6 Implementation Example

As an example to illustrate the implementation plan, the process of predicting the density profile of Lane III in the test site using GPR is presented as follows.

1. GPR equipment selection. As the surface layer of Lane III is relatively thin

(approximately 6.3 cm or 2.5 in), a 2 GHz air-coupled GPR system as shown in Figure 3.23, were used for collecting GPR data in Lane III. In addition, a DMI is attached to the survey vehicle wheel to synchronize the GPR data with survey distrance.

2. Asphalt mixture information collection. For the mixture placed in Lane III, the information as shown in Table 3.24 was collected. The asphalt binder content, P_b, effective specific gravity of aggregate, G_{se}, and maximum specific gravity of asphalt mixture, G_{mm}, were obtained from the mixture design. The specific gravity of binder, G_b, and the dielectric constant of binder, ε_b, are constants. In addition, the mixture in Lane III is mainly composed of granite aggregate, which usually has a dielectric constant value between 4 and 7.

Table 3.24 Basic Mixture Information of the Mixture Used in Lane III

P_b (%)	G_{se}	G_{mm}	G_b	ε_b
5.4	2.682	2.501	1.015	3

3. Aggregate dielectric constant determination. In order to find the accurate value of ε_s, two cores were extracted from Section 1 of Lane III. As Table 3.25 shows, the GPR-predicted ε_{AC} of these two cores are 5.25 and 5.12, respectively, and the lab-measured G_{mb} of these two cores are 2.364 and 2.353, respectively. Then by plugging the core ε_{AC} and G_{mb} into the ALL model (Equation 3.16), the values of ε_s were obtained as shown in Table 3.25. The parameter values shown in Table 3.24 were used for the back-calculation. The average dielectric constant of aggregate was found at 6.25.

Table 3.25 Aggregate Dielectric Constant of the Mixture Used in Lane III

Core #	ε_{AC}	G_{mb}	ε_s
1	5.25	2.364	6.30
2	5.12	2.353	6.19
Average			6.25

4. GPR data collection. Since Lane III in test site has a thin single-lift asphalt overlay, the surface-reflection method was employed to obtain the dielectric constant profile of the pavement surface. The GPR data was collected on a day without raining for more than three days, and the longitudinal dielectric constant profile as shown in Figure 3.57 was obtained according to Equation 2.27. As the figure shows, there is a clear decreasing trend in the measured dielectric constant from Section 1 to Section 4.

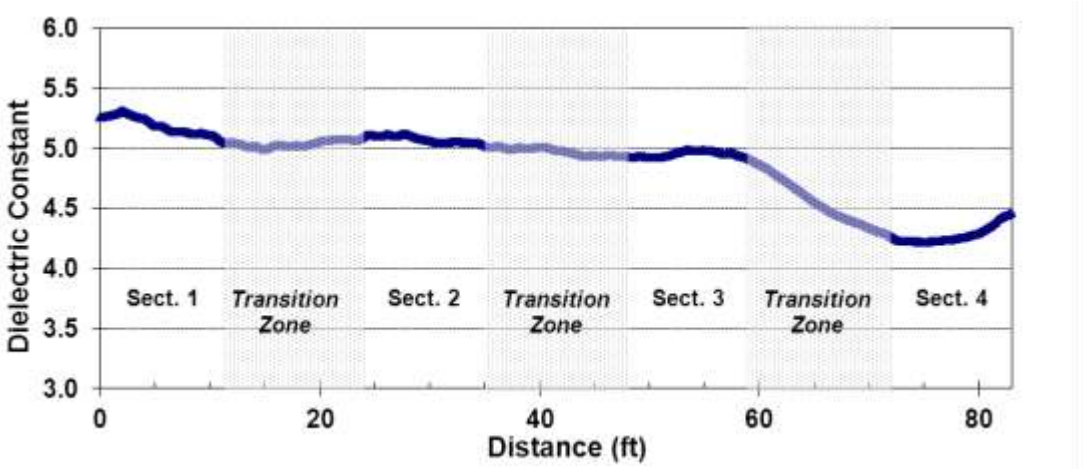

Figure 3.57 Longitudinal dielectric constant profile of Lane III in the test site.

5. Density prediction. The final step was to employ the ALL model developed in this study to predict the density profile of Lane III. By plugging the basic mixture information shown in Table 3.23, the average dielectric constant of aggregate

shown in Table 3.24, and the dielectric constant profile shown in Figure 3.57 into Equation 3.16, the bulk specific gravity profile as shown in Figure 3.58 was obtained. It is clear that the pavement density gradually decreases from Section 1 to Section 4. Once the bulk specific gravity profile of Lane III was known, its air void content profile, as shown in Figure 3.59 was easily acquired by applying Equation 3.2. As described in Section 3.2.1, the target air void contents of Sections 1, 2, 3, and 4 are 4%, 6%, 9%, and 12%, respectively. Figure 3.59 indicates that the measured air void contents in Sections 2 and 3 are close to the target values, and the densities of these two sections are relatively uniform. However, the measured air void contents in Sections 1 and 4 are higher than their target values, and their densities are not as uniformly distributed as those of Sections 2 and 3. This could be expected because Section 1 was over-compacted, while Section 4 was under-compacted, compared to normal compaction practice. In construction practice, an air void content profile as shown in Figure 3.59 can be used to easily locate those areas which have density problems.

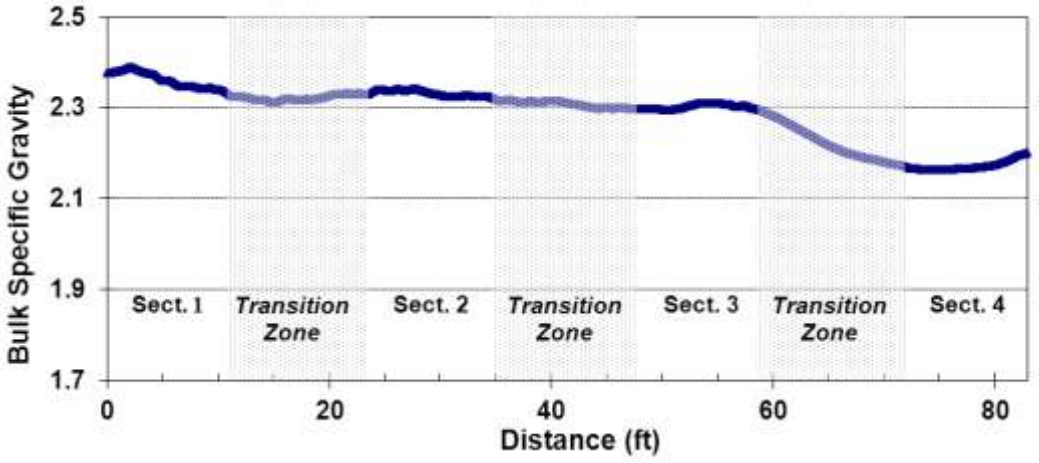

Figure 3.58 Longitudinal bulk specific gravity profile of Lane III in the test site.

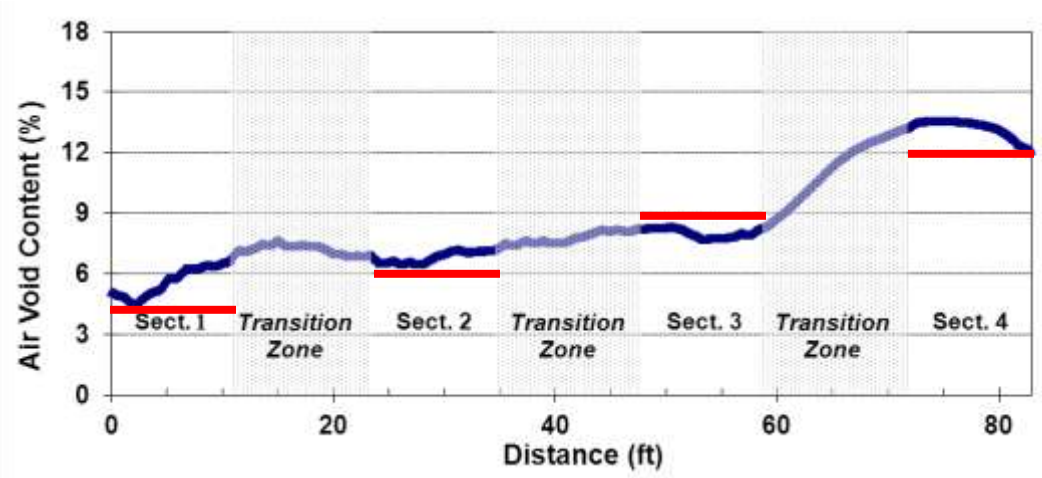

Figure 3.59 Longitudinal air void content profile of Lane III in the test site.

CHAPTER 4 FINDINGS, CONCLUSIONS, AND RECOMMENDATIONS

4.1 Summary

In-situ asphalt mixture density is critically important to the performance of flexible airport pavements, because density that is too high or too low may cause early pavement distresses. Traditionally, two methods have been commonly used for in-situ asphalt mixture density measurement: laboratory testing on field-extracted cores and on-site nuclear gauge testing. However, both these methods have limitations. The coring method damages pavement, causes traffic interruption, and only provides limited data at discrete locations. The nuclear gauge method cannot provide continuous measurement either. Moreover, it requires a license for the equipment operators because it uses radioactive material. To overcome the limitations of these traditional methods, this study develops a nondestructive method of using GPR to measure in-situ asphalt mixture density accurately, continuously, and rapidly.

To achieve the research objective, a comprehensive literature review on NDE tools for pavement quality assessment, EM theories pertinent to the GPR systems, and GPR applications to pavements was completed. Then, according to the EM mixing theory, two specific gravity models, based on the CRIM and the Bottcher model, were developed to predict the asphalt mixture's bulk specific gravity from its dielectric contestant.

To obtain realistic data input for the specific gravity model evaluation, a full-scale six-lane test site with four sections per lane was designed and constructed. Forty cores were extracted from the test site and their densities were measured in the laboratory. A comparison between the lab-measured core densities and the GPR-predicted values indicated that both models were effective in predicting asphalt mixture density, and the modified Bottcher model performed better.

To further improve the performance of the modified Bottcher model, a shape factor was introduced to account for the non-spherical shapes of the air voids and aggregate particles in asphalt mixture. Nonlinear least square fitting to the density and dielectric constant data of the field cores identified that a shape factor of -0.3 was the most suitable for asphalt mixture. The specific gravity model with a shape factor of -0.3 was referred to as the ALL model in this study, and its performance was then successfully verified by using the field data collected from in-service pavement sections in Chicago area.

To improve the accuracy of the asphalt mixture dielectric constant estimation, this study also investigated alternative methods for in-situ asphalt mixture dielectric constant estimation. The XCMP method using two air-coupled antenna systems was developed and its performance was evaluated using the test site data.

In the end, an implementation plan was proposed to help pavement engineers predict asphalt pavement density using GPR in practice.

4.2 Findings

Various findings regarding using GPR for asphalt mixture density prediction were encountered in this study. These findings are summarized as follows:

- A positive relation exists between the asphalt mixture's density and its dielectric constant, i.e., the dielectric constant of asphalt mixture increases when its density increases. This result has been supported by both the laboratory and field test results and is independent of mixture type.
- The CRIM and Bottcher models were modified in this study to allow predicting the asphalt mixture's density from its dielectric constant. The average prediction errors for 35 cores using the two modified models were 2.7% and 2.5%, respectively, when one calibration core was used.
- To account for the effect of the non-spherical inclusions in asphalt mixture, a shape factor was introduced into the modified Bottcher model. Hence, a new model, the Al-Qadi Lahouar Leng (ALL) model, was introduced.
- Based on the in-service pavement construction site data, when the ALL model was used with two calibration cores, the accuracy of GPR is comparable to, or better than, that of nuclear density gauge. For the asphalt mixtures without slags, the average density prediction errors of GPR are between 0.5% and 1.1%, while those of nuclear gauge are between 1.2% and 3.1%.
- A compaction curve between the GPR signal surface reflection amplitude and the pass number of the compactor can be built to track the asphalt mixture density change during its compaction process. In this curve, the reflection amplitude first increases due to the mixture densification and then stays constant after the

maximum density is reached. This compaction curve is helpful in determining the required compaction pass number to achieve the maximum asphalt mixture density, and the GPR measurement corresponding to the maximum density can be used as a reference to examine the density levels at other locations.

- The temperature effect on the GPR-measured dielectric constant of asphalt mixture is insignificant from 32 ^{o}C to 88 ^{o}C (90 ^{o}F to 190 ^{o}F), as supported by the field data. As a result, GPR measurement can be used to predict asphalt mixture density even when the mixture is at relatively high temperature.
- Using slag in asphalt mixture may decrease the density prediction accuracy of GPR.
- It is feasible to measure the dielectric constant of pavement using the XCMP technique with two air-coupled antenna systems. Compared to the traditional method based on the GPR signal surface-reflection amplitude, this technique predicts the average (or bulk) dielectric constant instead of the surface dielectric constant of the asphalt mixture. Therefore, its measurement is more representative for the whole asphalt mixture layer. However, the sampling rate of the GPR system must be high enough to ensure the accuracy of this method.

4.3 Conclusions

Based on this research, the following conclusions can be drawn:

- The estimated asphalt mixture's dielectric constant from GPR data can be used to predict its density and air void content when an appropriate model is used.
- An asphalt mixture density prediction model, Al-Qadi Lahouar Leng (ALL), was introduced, and its accuracy of in-situ asphalt mixture density prediction was successfully validated using in-service pavement data.
- When GPR is used for in-place asphalt airport pavement density prediction, the density profile along the length of the entire pavement could be predicted. Hence, the GPR method provides more efficient pavement density prediction compared to the current discrete methods: using the coring approach or estimation by the nuclear gauge method.

4.4 Recommendations for Further Study

This study has shown that GPR is an effective NDE tool for asphalt airport pavement density prediction. As a continuation of this research, the following recommendations are proposed:

- In this study, the specific gravity models were developed based on the assumption that the asphalt mixture is under dry condition. Further study should look into the accuracy and reliability of more advanced models which consider the contribution of moisture. The feasibility of using GPR to predict the asphalt mixture density and moisture content simultaneously should be investigated.
- The asphalt binder aging may also affect the GPR measurement. The significance of the aging effect on the asphalt mixture density prediction using GPR should also be studied.
- To obtain the real-time monitoring of the in-situ asphalt mixture density during construction, it is recommended to examine the feasibility of integrating the GPR system to the roller compactor. Effort may be focused on the appropriate way to install the GPR system to avoid antenna vibration during compaction and on the development of software to visually illustrate the real-time pavement density in a screen graphic.
- The performance of the XCMP technique should be further investigated by using GPR systems with higher sampling rates. Besides, the configuration of a mono-static air-coupled system and a bi-static system with adjustable separation distance between transmitter and receiver may be employed to further improve the accuracy of the XCMP method.

REFERENCES

AASHTO T166 (2007). *Standard Method of Test for Bulk Specific Gravity of Compacted Hot Mix Asphalt (HMA) Using Saturated Surface-Dry Specimens,* American Association of State Highway and Transportation Officials (AASHTO), Washington, D. C.

AASHTO T269 (2007). *Standard Method of Test for Percent Air Voids in Compacted Dense and Open Asphalt Mixtures,* American Association of State Highway and Transportation Officials (AASHTO), Washington, D. C.

AASHTO T331 (2007). *Standard Method of Test for Bulk Specific Gravity and Density of Compacted Asphalt Mixtures Using Automatic Vacuum Sealing Method,* American Association of State Highway and Transportation Officials (AASHTO), Washington, D. C.

Abo-Qudais, S., and Suleiman, A. (2005). "Monitoring fatigue damage and crack healing by ultrasound wave velocity." *Nondestructive Testing and Evaluation*, 20(2), 125-145.

Achenbach, J. D. (1984). *Wave Propagation in Elastic Solids*. New York: Elsevier.

Al-Qadi, I. L. (1992). “Using microwave measurements to detect moisture in asphaltic concrete.” Journal of Testing and Evaluation. 20(1), 43-50.

Al-Qadi, I. L., and Lahouar, S. (2005a). "Measuring layer thicknesses with GPR-Theory to practice." *Construction and Building Materials*, 19(10), 763-772.

Al-Qadi, I. L., and Lahouar, S. (2005b). "Measuring rebar cover depth in rigid pavements with ground-penetrating radar." *Transportation Research Record* (1907), 81-85.

Al-Qadi, I. L., Lahouar, S., and Loulizi, A. (2001). "In-situ measurements of hot-mix asphalt dielectric properties." *NDT & E international*, 34(6), 427-434.

Al-Qadi, I. L., Lahouar, S., and Loulizi, A. (2003). "Successful application of ground-penetrating radar for quality assurance-quality control of new pavements." *Transportation Research Record: Journal of the Transportation Research Board*, 1861, 86-97.

Ai-Qadi, I. L., Lahouar, S., Jiang, K., McGhee, K. K., and Mokarem, D. (2005). "Accuracy of ground-penetrating radar for estimating rigid and flexible pavement layer thicknesses." *Transportation Research Record: Journal of the Transportation Research Board,* 1940, 69-78.

Al-Qadi, I. L., and Riad, S. M. (1996). *Characterization of Portland Cement Concrete: Electromagnetic and Ultrasonic Measurement Techniques*. Report submitted to the National Science Foundation.

Al-Qadi, I. L., Riad, S. M., Su, W. U., and Haddad, R. H. (1996). “Detecting flaws in Portland cement concrete using TEM horn antennae.” *SPIE*, 2946, 28-39.

ASTM E274 (2003). *Standard Test Method for Skid Resistance of Paved Surfaces Using a Full-Scale Tire*, ASTM International, West Conshohocken, PA.

ASTM E445 (2003). *Standard Test Method for Stopping Distance on Paved Surfaces Using a Passenger Vehicle Equipped with Full-Scale Tires*, ASTM International, West Conshohocken, PA.

ASTM E670 (2003). *Standard Test Method for Side Force Friction on Paved Surfaces Using the Mu-Meter*, ASTM International, West Conshohocken, PA.

Austroads Test Method AG: AM/T009 (2007). *Pavement Rutting Measurement with A Multi-laser Profilometer*

Balanis, C. A. (1989). *Advanced Engineering Electromagnetics*, Wiley, New York.

Behari, J. (2005). *Microwave Dielectric Behavior of Wet Soils*, Springer, New York.

Black, K., and Kopac, P. (1992). "The application of ground-penetrating radar in highway engineering." *Public Roads,* 56(3), 96-103.

Cardimona, S., Willeford, B., Webb, D., Hickman, S., Wenzlick, J., and Anderson, N. (2003). "Automated pavement analysis in Missouri using ground penetrating radar." *University of Missouri-Rolla, Department of Geology and Geophysics*.

Chang, G. K., Xu, Q., Rasmussen, R., Merritt, D., Michael, L., White, D., and Horan, B. (2010), *Accelerated Implementation of Intelligent Compaction Technology For Embankment Subgrade Soils, Aggregate Base, and Asphalt Pavement Materials.* Report submitted to the Federal Highway Administration.

Chen, D., and Scullion, T. (2008). "Detecting subsurface voids using ground-coupled penetrating radar." *ASTM Geotechnical Testing Journal*, 31(3), 217-224.

Commuri, S. and Lemon, B. (2007). *Intelligent Asphalt Compaction Analyzer.* Report submitted to the Federal Highway Administration.

Guzina, B. B., and Osburn, R. H. (2002). "Effective tool for enhancing elastostatic pavement diagnosis." *Transportation Research Record: Journal of the Transportation Research Board*, 1806, 30-37.

Gucunski, N., and Krstic V. (1996). “Backcalculation of pavement profiles from spectral-analysis-of-surface-waves test by neural networks using individual receiver spacing approach.”

Transportation Research Record: Journal of the Transportation Research Board, 1526, 6-13.

Hill, M., McHugh, J. and Turner, J.D. (2000). “Cross-sectional modes in impact-echo testing of concrete structures.” *Journal of Structural Engineering*, 126, 228–234.

http://en.wikipedia.org/wiki/File:EM_spectrum.svg, accessed on Oct. 30, 2010

http://www.mit-dresden.de/, accessed on Oct. 30, 2010

http://training.ce.washington.edu/WSDOT/ , accessed on Nov. 22, 2010

Huston, D. R., Pelczarski, N. V., Esser, B., and Maser, K. R. (2000) "Damage detection in roadways with ground penetrating radar." *Proceedings of the Eighth International Conference on Ground Penetrating Radar,* Gold Coast, Australia*,* 91-94.

Jiang, Z. Y., Ponniah, J., Cascante, G., and Charlottetown, P. E. I (2006). "Improved ultrasonic pulse velocity technique for bituminous material characterization." *Annual Conference & Exhibition of the Transportation Association of Canada,* Charlottetown, Prince Edward Island, Canada.

Joyce R. P. (1985). *Rapid Nondestructive Delamination Detection*. Final Report No. FHWA/RD-85/051. Federal Highway Administration, Washington, D. C.

Khazanovich, L., Velasquez, R., and Nesvijski, E. G. (2005). "Evaluation of top-down cracks in asphalt pavements by using a self-calibrating ultrasonic technique." *Transportation Research Record: Journal of the Transportation Research Board*, 1940, 63-68.

Killingsworth, B. M (2004). *Quality Characteristics for Use with Performance Related Specifications for Hot Mix Asphalt*. NCHRP Project 9-15 Research Results Digest 291, Washington, D.C.: Transportation Research Board, National Research Council.

Lahouar, S. (2003). *Development of Data Analysis Algorithms for Interpretation of Ground Penetrating Radar Data.* Ph.D. Dissertation, Virginia Polytechnic Institute and State University, Blacksburg, VA.

Lahouar, S., and Al-Qadi, I. L. (2008). "Automatic detection of multiple pavement layers from GPR data." *NDT and E International*, 41(2), 69-81.

Lahouar, S., Al-Qadi, I. L., Loulizi, A., Clark, T. M., and Lee, D. T. (2002). "Approach to determining in-situ dielectric constant of pavements: Development and implementation at interstate 81 in Virginia." *Transportation Research Record: Journal of the Transportation Research Board*, 1806, 81-87.

Leng, Z., Al-Qadi, I. L., Baek, J., and Lahouar, S. (2009). “Selection of antenna type and frequency for pavement surveys using GPR.” *88th Annual Meeting of the Transportation Research Board,* CD-ROM, Transportation Research Board of the National Academies, Washington, D.C.

Leng, Z., Al-Qadi, I. L., and Lahouar, S. (2011). “Development and validation for in-situ asphalt mixture density prediction model.” *NDT&E International*, Elsevier, 44(4), 2011, 369-375.

Loulizi, A. (2001). *Development of Ground Penetrating Radar Signal Modeling and Implementation for Transportation Infrastructure Assessment,* Ph.D. Dissertation, Virginia Polytechnic Institute and State University, Blacksburg, VA.

Loizos, A., and Plati, C. (2007). "Accuracy of pavement thicknesses estimation using different ground penetrating radar analysis approaches." *NDT and E International*, 40(2), 147-157.

Luo, Q., and Bungey, J. H. (1996). "Using compression wave ultrasonic transducers to measure the velocity of surface waves and hence determine dynamic modulus of elasticity for concrete." *Construction and building materials*, 10(4), 237-242.

Lytton, R. L (1995). *System Identification and Analysis of Subsurface Radar Signals,* U.S. Patent No. 5384715, Texas A&M University, Licensed to Lyric Technologies, Inc., Houston, TX.

Lytton, R. L. (2000). "Characterizing asphalt pavements for performance." *Transportation Research Record: Journal of the Transportation Research Board*, 1723(-1), 5-16.

Malhotra, V. M., and Carino, N. J. (2004). *Handbook on nondestructive testing of concrete*, CRC press.

Maser, K. R. (1996). "Condition assessment of transportation infrastructure using ground-penetrating radar." *Journal of infrastructure systems*, 2(2), 94-101.

Morey, R. M. (1998). “*Ground penetrating radar for evaluating subsurface conditions for transportation facilities*,” NCHRP Synthesis 255, Transportation Research Board, Washington D.C.

Nazarian, S., Yuan, D. and Tandon, V. (1999). “Structural field testing of flexible layers with seismic methods for quality control.” *Transportation Research Record: Journal of the Transportation Research Board*,1654, 1–27.

Newnham, L. and Goodier, A. (2000). “Using neural networks to interpret sub-surface radar imagery of reinforced concrete," *Proceedings of GPR 2000*, University of Queensland, Australia, CD-ROM.

Olhoeft, G. R., and Smith III, S. S. "Automatic processing and modeling of GPR data for pavement

thickness and properties." *Proc. of the 8th International Conference on Ground Penetrating Radar,* Gold Coast, Australia,188-193.

Pellinen, T. K., and Witczak, M. W. (2002). "Use of stiffness of hot-mix asphalt as a simple performance test." *Transportation Research Record: Journal of the Transportation Research Board*, 1789, 80-90.

Romero, P., and Kuhnow, F. (2002). “Evaluation of new non-nuclear pavement density gauges with data from field projects.’ *Transportation Research Record: Journal of the Transportation Research Board*, 1813, 47-54.

Rhazi, J., Dous, O., Ballivy, G., Laurens, S., and Balayssac, J. P. (2003). "Non destructive health evaluation of concrete bridge decks by GPR and half cell potential techniques." *International Symposium on Non-Destructive Testing in Civil Engineering,* CD-ROM, Berlin, Germany.

Roberts, F.L., Kandhal, P.S., Brown, E.R., Lee, D.Y., and Kennedy, T.W. (1996). *Hot Mix Asphalt Materials, Mixture Design, and Construction*. National Asphalt Paving Association Education Foundation. Lanham, MD.

Saarenketo, T. (1997). "Using ground-penetrating radar and dielectric probe measurements in pavement density quality control." *Transportation Research Record: Journal of the Transportation Research Board*, 1575, 34-41.

Saarenketo, T., and Scullion, T. (1994). *Ground Penetrating Radar Applications on Roads and Highways,* Research Report, Texas Transportation Institute, College Station, TX.

Saarenketo, T., and Scullion, T. (2000). "Road evaluation with ground penetrating radar." *Journal of applied geophysics*, 43(2-4), 119-138.

Schneider, W. A. (1984). "The common depth point stack." *Proceedings of the IEEE*, 72(10), 1238-1254.

Sebesta, S., and Scullion, T. (2002). “Application of infrared imaging and ground-penetrating radar for detecting segregation in hot-mix asphalt overlays,” *Transportation Research Record: Journal of the Transportation Research Board*,1861, 37-43.

Shaw, M. R., Molyneaux, T. C. K., Millard, S. G., Bungey, J. H., and Taylor, M. J. (1998). “Automatic analysis of GPR scans on concrete structures," *Proceedings of GPR 98*, University of Kansas, USA, 449-454.

Sihvola, A. and Lindell, I. V. (1989). “Polarizability and effective permittivity of layered and continuously inhomogeneous dielectric spheres,” *Journal of Electromagnetic Waves*

Application, 3(1), 37-60.

Sihvola, A. (1989). “Self-consistency aspects of dielectric mixing theories,” IEEE Transactions on Geoscience and Remote Sensing, 27(4), 403-415.

Silvast, M. (2001). *Air Void Content Measurement Using GPR Technology at Helsinki-Vantaa Airport, Runway No. 3*, Survey Report, Roadscanners, Finland.

Steinway, W. J., Echard, J. D., and Luke, C. M. (1981). *Locating Voids beneath Pavement Using Pulsed Electromagnetic Waves,* NCHRP Report 237, National Cooperative Highway Research Program, Transportation Research Board, Washington DC, USA.

Tayabji, S. D., and Lukanen, E. O. (2000). *Nondestructive Testing of Pavements and Backcalculation of Moduli: Third Volume*, ASTM, West Conshohocken, PA.

UK Department of Transport (2001). *Design Manual for Roads and Bridges - Volume 7, Section 3, Part 2: HD29/94 Structural Assessment Methods, Chapter 6 Ground Radar,* The Stationary Office, London, UK.

Van, Thomas. (2008). “Rolling wheel deflectometer: a high-speed deflection device to improve asset management,” *Focus,* Federal Highway Administration.

Von Quintus, H. L. (2009). *NDT technology for quality assurance of HMA pavement construction*, Transportation Research Board.

Wells, A. K., and Lytton, R. L. (2001) “Ground penetrating radar for measuring pavement layer composition and void detection,” *Second International Symposium on Maintenance and Rehabilitation of Pavements and Technological Control*, Auburn, Alabama, USA.

APPENDIX A MIX DESIGNS FOR TEST SITE CONSTRUCTION

A.1 Limestone Binder Mix

DATE: 15-Oct-2008

SEQ NO:

Bituminous Mixture Design

Design Number:----->	85BIT0000
Lab preparing the design?(PP,PL,IL ect.)	PP
Producer Name & Number>	6437-01 Open Road Asphalt Fairmount, IL
Material Code Number--->	18612 BIT BASE TYB AERO TONS

Required! FA20/21 RAP in #6

Agg No.	#1	#2	#3	#4	#5	#6	ASPHALT
Size (e.g. 032CAM16)	042CMM11	032CMM16	039FAM20	037FAM02	004MFM01		10127
Source (PROD#)	MATL SERV	MATL SERV	52100-32	52100-32	51352-04		2250-03
(NAME)	51832-01	51832-01	INTER S&G	INTER S&G	MaterialService		EMLSCT
(LOC)	FAIRMOUNT	FAIRMOUNT	WEST LEB, IN	WEST LEB, IN	Nokomis, IL		URBANA
					RAP in Mix:		
Aggregate Blend	38.0	22.0	14.6	22.0	3.4		100.0

Agg No. / Sieve Size	#1	#2	#3	#4	#5	#6	Blend	Sieve Size
1	100.0	100.0	100.0	100.0	100.0	100.0	100.0	1
3/4	95.9	100.0	100.0	100.0	100.0	100.0	98.4	3/4
1/2	40.0	100.0	100.0	100.0	100.0	100.0	77.2	1/2
3/8	13.3	98.1	100.0	100.0	100.0	100.0	66.6	3/8
#4	3.3	29.3	99.9	99.5	100.0	100.0	47.6	#4
#8	2.5	4.3	79.0	92.3	100.0	100.0	37.1	#8
#16	2.2	3.2	51.3	66.7	100.0	100.0	27.1	#16
#30	2.0	2.8	30.9	34.2	100.0	100.0	16.8	#30
#50	1.9	2.5	18.5	9.7	100.0	100.0	9.5	#50
#100	1.7	2.3	9.0	2.8	95.0	100.0	6.3	#100
#200	1.5	2.1	4.4	2.0	85.0	100.0	5.0	#200

Mixture Composition Specification	Formula	Formula Range Min	Formula Range Max
	100	100	100
	98	98	98
	77	77	77
	67	67	67
	48	41	55
	37	32	42
	27	22	32
	17	13	21
	10	10	10
	6	4	8
	5.0	3.0	7.0

							Blended SpGr	
Bulk Sp Gr	2.617	2.603	2.588	2.579	2.800	1.000	2.607	
Apparent Sp Gr	1.000	1.000	1.000	1.000	1.000	1.000		Dust AC Ratio
Absorption, %	1.20	1.60	2.20	1.70	1.00	1.00	1.000	0.98
					SP GR AC		1.03	

BITUMINOUS MIXTURE AGED HOW LONG? 1.0 HOURS @ 295.0 F

SUMMARY OF SUPERPAVE GYRATORY TEST DATA

	N-initial 10				N-design 40			
PB:	4.5	5	5.5	6	4.5	5	5.5	6
Gmb (corr):	2.283	2.303	2.316	2.317	2.392	2.415	2.427	2.428
Gmm:	2.492	2.472	2.452	2.431	2.492	2.472	2.452	2.431
Pa:	8.4	6.8	5.6	4.7	4.0	2.3	1.0	0.1
VMA:	16.4	16.1	16.0	16.5	12.4	12.0	12.0	12.5
FIELD VMA:	18.4	18.0	17.9	18.2	14.5	14.0	14.0	14.3
VFA:	48.8	57.4	65.4	71.5	67.6	80.7	91.4	98.9
Vbe:	8.0	9.2	10.5	11.8	8.4	9.7	11.0	12.3
Pbe:	3.6	4.1	4.7	5.2	3.6	4.1	4.7	5.2
Gse:	2.671	2.669	2.667	2.662	2.671	2.669	2.667	2.662
Pba:	0.9	0.9	0.9	0.8	0.9	0.9	0.9	0.8

Slope: 7.5

NUMBER OF REVOLUTIONS: 40

	% AC	Gmm	Gmb	% Voids Pa	VMA	Design Field VMA	VFA	Gse	Gsb
OPTIMUM DESIGN DATA:	5.1	2.467	2.418	2.0	12.0	14.0	83.3	2.668	2.607

REMARKS:

A.2 Limestone Surface Mix

DATE: 15-Oct-2008

SEQ NO:

Bituminous Mixture Design

Design Number:-----> 85BIT0001

Lab preparing the design?(PP,PL,IL ect.) PP

Producer Name & Number> 6437-01 Open Road Asphalt Fairmount, IL

Material Code Number---> 18712 BIT SUR TYB AERO TONS

Required FA20/21 RAP in #6

Agg No.	#1	#2	#3	#4	#5	#6	ASPHALT
Size (e.g. 032CAM16)	032CMM16		039FAM20	037FAM02	004MFM01		10127
Source (PROD#)	MATL SERV		52100-32	52100-32	51352-04		2260-03
(NAME)	51832-01		INTER S&G	INTER S&G	MaterialService		EMLSCT
(LOC)	FAIRMOUNT		WEST LEB, IN	WEST LEB, IN	Nokomis, IL		URBANA
					RAP in Mix:		
Aggregate Blend	58.0		12.0	25.6	4.4		100.0

Agg No. / Sieve Size	#1	#2	#3	#4	#5	#6	Blend	Sieve Size
1	100.0	100.0	100.0	100.0	100.0	100.0	100.0	1
3/4	100.0	100.0	100.0	100.0	100.0	100.0	100.0	3/4
1/2	100.0	100.0	100.0	100.0	100.0	100.0	100.0	1/2
3/8	98.1	100.0	100.0	100.0	100.0	100.0	98.9	3/8
#4	29.3	100.0	99.9	99.5	100.0	100.0	58.9	#4
#8	4.3	100.0	79.0	92.3	100.0	100.0	40.0	#8
#16	3.2	100.0	51.3	66.7	100.0	100.0	29.5	#16
#30	2.8	100.0	30.9	34.2	100.0	100.0	18.5	#30
#50	2.5	100.0	18.5	9.7	100.0	100.0	10.6	#50
#100	2.3	100.0	9.0	2.8	95.0	100.0	7.3	#100
#200	2.1	100.0	4.4	2.0	85.0	100.0	6.0	#200

Mixture Composition Specification	Formula	Formula Range Min	Formula Range Max
	100	100	100
	100	100	100
	100	100	100
	99	99	99
	59	52	66
	40	35	45
	29	24	34
	18	14	22
	11	11	11
	7	5	9
	6.0	4.0	8.0

							Blended SpGr	
Bulk Sp Gr	2.603	1.000	2.588	2.579	2.800	1.000	2.603	
Apparent Sp Gr	1.000	1.000	1.000	1.000	1.000	1.000		Dust AC Ratio
Absorption, %	1.60	1.00	2.20	1.70	1.00	1.00	1.000	1.00
					SP GR AC		1.03	

BITUMINOUS MIXTURE AGED HOW LONG? 1.0 HOURS @ 295.0 F

SUMMARY OF SUPERPAVE GYRATORY TEST DATA

	N-initial 10				N-design 40			
PB:	5.5	6	6.5	7	5.5	6	6.5	7
Gmb (corr):	2.222	2.248	2.243	2.249	2.356	2.381	2.382	2.386
Gmm:	2.445	2.431	2.405	2.397	2.445	2.431	2.405	2.397
Pa:	9.1	7.5	6.7	6.2	3.6	2.0	1.0	0.4
VMA:	19.3	18.8	19.4	19.6	14.5	14.0	14.4	14.8
FIELD VMA:	21.0	20.6	20.9	21.5	16.2	15.9	16.0	16.7
VFA:	52.9	60.1	65.3	68.6	74.9	85.4	93.3	97.0
Vbe:	10.2	11.3	12.7	13.5	10.8	12.0	13.5	14.3
Pbe:	4.7	5.2	5.8	6.2	4.7	5.2	5.8	6.2
Gse:	2.657	2.662	2.651	2.663	2.657	2.662	2.651	2.663
Pba:	0.8	0.9	0.7	0.9	0.8	0.9	0.7	0.9

Slope: 9.1

NUMBER OF REVOLUTIONS: 40

	% AC	Gmm	Gmb	% Voids Pa	VMA	Design Field VMA	VFA	Gse	Gsb
OPTIMUM DESIGN DATA:	6.0	2.430	2.381	2.0	14.0	15.9	85.7	2.661	2.603

REMARKS:

A.3 Gravel Surface Mix

DATE: 15-Oct-2008

SEQ NO:

Bituminous Mixture Design

Design Number:-----> 85BIT9998

Lab preparing the design?(PP,PL,IL ect.) PP

Producer Name & Number> 6437-01 Open Road Asphalt

Material Code Number---> 18712 BIT SUR TYB AERO TONS

Required FA20/21 RAP in #6

Agg No.	#1	#2	#3	#4	#5	#6	ASPHALT
Size (e.g. 032CAM16)	031CMM16		039FAM20	037FAM02	004MFM01		10127
Source (PROD#)	52100-32		52100-32	52100-32	51352-04		2660-03
(NAME)	Interstate S&G		Interstate S&G	Interstate S&G	Material Service		Emulsicoat
(LOC)	W Leb, IN		W Leb, IN	W Leb, IN	Nokomis, IL		Fairmount, IL
					RAP in Mix:		
Aggregate Blend	55.0		12.0	28.0	5.0		100.0

Agg No. / Sieve Size	#1	#2	#3	#4	#5	#6	Blend	Sieve Size	Mixture Composition Specification	Formula	Formula Range Min	Formula Range Max
1	100.0	100.0	100.0	100.0	100.0	100.0	100.0	1		100	100	100
3/4	100.0	100.0	100.0	100.0	100.0	99.4	100.0	3/4		100	100	100
1/2	100.0	100.0	100.0	100.0	100.0	93.6	100.0	1/2		100	100	100
3/8	94.8	100.0	100.0	100.0	100.0	89.3	97.1	3/8		97	97	97
#4	24.0	100.0	99.9	99.5	100.0	61.6	58.0	#4		58	51	65
#8	2.6	100.0	79.0	92.3	100.0	41.8	41.8	#8		42	37	47
#16	1.7	100.0	51.3	66.7	100.0	30.9	30.8	#16		31	26	36
#30	1.3	100.0	30.9	34.2	100.0	22.6	19.0	#30		19	15	23
#50	1.2	100.0	18.5	9.7	100.0	16.2	10.6	#50		11	11	11
#100	1.1	100.0	9.0	2.8	95.0	12.0	7.2	#100		7	5	9
#200	0.9	100.0	4.4	2.0	85.0	9.5	5.8	#200		5.8	3.8	7.8

							Blended SpGr	
Bulk Sp Gr	2.671	1.000	2.588	2.579	2.800	2.630	2.641	
Apparent Sp Gr	1.000	1.000	1.000	1.000	1.000	1.000		Dust AC Ratio
Absorption, %	1.50	1.00	2.20	1.70	1.00	1.00	1.000	
					SP GR AC		1.03	1.07

BITUMINOUS MIXTURE AGED HOW LONG? HOURS @ C

SUMMARY OF SUPERPAVE GYRATORY TEST DATA

	N-initial 10				N-design 40			
PB:	5	5.5	6	6.5	5	5.5	6	6.5
Gmb (corr):	2.208	2.308	2.311	2.307	2.405	2.419	2.419	2.426
Gmm:	2.482	2.464	2.446	2.426	2.482	2.464	2.446	2.426
Pa:	11.0	6.3	5.5	4.9	3.1	1.8	1.1	0.0
VMA:	20.6	17.4	17.7	18.3	13.5	13.4	13.9	14.1
FIELD VMA:	21.7	18.7	19.0	19.5	14.8	14.8	15.2	15.3
VFA:	46.4	63.5	68.9	73.2	77.1	86.3	92.1	99.9
Vbe:	9.5	11.1	12.2	13.4	10.4	11.6	12.8	14.1
Pbe:	4.4	4.9	5.4	6.0	4.4	4.9	5.4	6.0
Gse:	2.680	2.682	2.681	2.678	2.680	2.682	2.681	2.679
Pba:	0.6	0.6	0.6	0.6	0.6	0.6	0.6	0.6

Slope: 7.5

NUMBER OF REVOLUTIONS: 40

	% AC	Gmm	Gmb	% Voids Pa	VMA	Design Field VMA	VFA	Gse	Gsb
OPTIMUM DESIGN DATA:	5.4	2.466	2.417	2.0	13.4	14.8	85.1	2.682	2.641

REMARKS:

APPENDIX B ESTIMATED MIXTURE WEIGHT FOR CONSTRUCTION

Mix Type	Gmm	Air Void	Gmb	Weight (ton/lane*in*ft))
Mix I	2.475	4%	2.376	0.097
	2.475	6%	2.327	0.095
	2.475	9%	2.252	0.092
	2.475	12%	2.178	0.089
Mix II	2.492	4%	2.392	0.098
	2.492	6%	2.342	0.096
	2.492	9%	2.268	0.093
	2.492	12%	2.193	0.090
Mix III	2.475	4%	2.376	0.097
	2.475	6%	2.327	0.095
	2.475	9%	2.252	0.092
	2.475	12%	2.178	0.089
Mix IV	2.457	4%	2.359	0.096
	2.457	6%	2.310	0.094
	2.457	9%	2.236	0.091
	2.457	12%	2.162	0.088
Mix V	2.498	4%	2.398	0.098
	2.498	6%	2.348	0.096
	2.498	9%	2.273	0.093
	2.498	12%	2.198	0.090

APPENDIX C MIXTURE TEMPERATURE DURING CONSTRUCTION

C.1 Lane I(A)

Temperature (°F)		In the Paver	Before Compaction	After 1st Pass	After 2nd Pass	After 3rd Pass	Last Pass
Lift 1	Section 1	300	220	200	190	160	158
	Section 2		217	198	189	170	160
	Section 3		216	200	190	170	
	Section 4		213	198			160
Lift 2	Section 2	300	300	260	210	200	185
	Section 3		295	250	220	200	180
	Section 4		270	230	215	195	175
Lift 3	Section 3	304	270	220	205	200	
	Section 4		265	225	210	200	
Lift 4	Section 4	320	310	230	185	165	160

C.2 Lanes I(B) to V

Temperature (°F)		In the Paver	Before Compaction	After 1st Pass	After 2nd Pass	After 3rd Pass	Last Pass
Lane I(B)	Section 1	293	278	250	210	205	
	Section 2		260	245	235	180	
	Section 3		235	223	210		200
	Section 4		220	212	190		170
Lane II	Section 1	285	260	245	210	203	170
	Section 2		250	240	210	205	171
	Section 3		250	240	220		187
	Section 4		235	230	220		180
Lane III	Section 1	300	264	245	220		180
	Section 2		261	247	220		182
	Section 3		238	220	205		178
	Section 4		234	215	206		180
Lane IV	Section 1	292	260	240	222		175
	Section 2		250	240	220		180
	Section 3		235	212	201		176
	Section 4		220	200	190		180
Lane V	Section 1	288	245	220			188
	Section 2		245	218			188
	Section 3		230	215			192
	Section 4		240	220			197

APPENDIX D AGGREGATE TYPES FOR CONSTRUCTION SITE MIXES

D.1 Percentage of Aggregate Used in New Mixes

Aggregate Code		039CM13	032CM16	038FM20	037FM02	004MF01	032CM13	Scalped 032CM13	Scalped FM22
Aggregate Type		Steel Slag	Dolomite	Dolomite	Natural Sand	Mineral Filler	Quartzite	Quartzite	Dolomite
Percentage (%)	Quartzite Mix	-	17.8	45.4	17.9	1.1	17.8	-	-
	4.75 mm SMA	-	-	12.4	-	8.2	-	39.7	39.7
	Sprinkle Mix	-	35.7	43.9	19.8	0.6	-	-	-
	Fiber/Slag Mix	20.3	16.3	44.0	17.5	1.9	-	-	-

D.2 Percentage of Aggregate Used in Control Mixes

Aggregate Code		039CM13	032CM16	038FM20	037FM02	004MF01	017CM13	039CM11
Aggregate Type		Steel Slag	Dolomite	Dolomite	Natural Sand	Mineral Filler	RAP	Dolomite
Percentage (%)	Friction Mix	35.7	26.0	19.5	7.8	1.0	10.0	-
	12.5mm SMA	57.0	-	9.0	-	7.0	-	27.0

APPENDIX E MATLAB CODES FOR THE XCMP METHOD

This appendix provides the Matlab codes for numerically solving Equations 3.38 ad 3.39 to obtain the dielectric constant and layer thickness of the asphalt pavement.

Matlabe m file name: call.m

```
clc; clear;
x0=[0.02; 0.08];%Make a starting guess at the solution for x1 and
x2; for thin pavement, guess values of [0.01 0.02] should be used
options=optimset('Display','iter'); %Option to display output
[x,fval]=fsolve(@myfun,x0,options) %Call optimizer

[F,diel,d,t1,t2]=myfun(x);
d=d*100/2.54; %change unit from "m" to "in"
t1
t2
fprintf('The dielectric constant of HMA is: %4.1f \n', diel);
fprintf('The thickness of the HMA layer is %4.2fin \n', d)
```

Matlabe m file name: myfun.m

```
function [F,diel,d,t1,t2]=myfun(x,delta_t1,delta_t2)

% Distance unit is "m", and time unit is "ns";

c=0.3; %speed of light

% Input Antenna Configuration Measurements
x01=14.96*2.54/100; %the distance between T2R2
x02=(36+14.96)*2.54/100; %the distance between T1R2
h=(22+14.1)*2.54/100; %antenna height above the ground

% Input GPR time data
delta_t1=0.953125; %time difference between surface and bottom
reflections for T2R2
delta_t2=0.923828; %time difference between surface and bottom
reflections for T1R2

t1=delta_t1+sqrt(4*h^2+x01^2)/c-sqrt(4*h^2+(x01-x(1))^2)/c;
t2=delta_t2+sqrt(4*h^2+x02^2)/c-sqrt(4*h^2+(x02-x(2))^2)/c;

F=[((x01-x(1))/(2*h))^2+1-t1^2*(x(2)^2-x(1)^2)^2/(t1^2*(x(2)^2-
x(1)^2)^2-x(1)^2*c^2*(t2^2-t1^2)^2);
    ((x02-x(2))/(2*h))^2+1-t2^2*(x(2)^2-x(1)^2)^2/(t2^2*(x(2)^2-
x(1)^2)^2-x(2)^2*c^2*(t2^2-t1^2)^2)];
```

```
x;
diel=c^2*(t2^2-t1^2)/(x(2)^2-x(1)^2);
d=sqrt(c^2/diel*t1^2/4-x(1)^2/4);
```